

# UNCLASSIFIED

AD NUMBER
ADB281577
NEW LIMITATION CHANGE
TO Approved for public release, distribution unlimited
FROM Distribution authorized to U.S. Gov't. agencies only; Proprietary Information; Oct 2001. Other requests shall be referred to US Army Medical Research and Materiel Command, 504 Scott Street, Ft. Detrick, MD 21702
AUTHORITY
USAMRMC ltr, DTD 01 Jul 2003

THIS PAGE IS UNCLASSIFIED

AD\_\_\_\_\_

Award Number: DAMD17-99-1-9218

TITLE: Frequency-Domain Optical Mammography

PRINCIPAL INVESTIGATOR: Sergio Fantini, Ph.D.

CONTRACTING ORGANIZATION: Tufts University  
Medford, Massachusetts 02155

REPORT DATE: October 2001

TYPE OF REPORT: Annual

PREPARED FOR: U.S. Army Medical Research and Materiel Command  
Fort Detrick, Maryland 21702-5012

DISTRIBUTION STATEMENT: Distribution authorized to U.S. Government agencies only (proprietary information, Oct 01). Other requests for this document shall be referred to U.S. Army Medical Research and Materiel Command, 504 Scott Street, Fort Detrick, Maryland 21702-5012.

The views, opinions and/or findings contained in this report are those of the author(s) and should not be construed as an official Department of the Army position, policy or decision unless so designated by other documentation.

20020814 152

## NOTICE

USING GOVERNMENT DRAWINGS, SPECIFICATIONS, OR OTHER DATA INCLUDED IN THIS DOCUMENT FOR ANY PURPOSE OTHER THAN GOVERNMENT PROCUREMENT DOES NOT IN ANY WAY OBLIGATE THE U.S. GOVERNMENT. THE FACT THAT THE GOVERNMENT FORMULATED OR SUPPLIED THE DRAWINGS, SPECIFICATIONS, OR OTHER DATA DOES NOT LICENSE THE HOLDER OR ANY OTHER PERSON OR CORPORATION; OR CONVEY ANY RIGHTS OR PERMISSION TO MANUFACTURE, USE, OR SELL ANY PATENTED INVENTION THAT MAY RELATE TO THEM.

### LIMITED RIGHTS LEGEND

Award Number: DAMD17-99-1-9218  
Organization: Tufts University

Those portions of the technical data contained in this report marked as limited rights data shall not, without the written permission of the above contractor, be (a) released or disclosed outside the government, (b) used by the Government for manufacture or, in the case of computer software documentation, for preparing the same or similar computer software, or (c) used by a party other than the Government, except that the Government may release or disclose technical data to persons outside the Government, or permit the use of technical data by such persons, if (i) such release, disclosure, or use is necessary for emergency repair or overhaul or (ii) is a release or disclosure of technical data (other than detailed manufacturing or process data) to, or use of such data by, a foreign government that is in the interest of the Government and is required for evaluational or informational purposes, provided in either case that such release, disclosure or use is made subject to a prohibition that the person to whom the data is released or disclosed may not further use, release or disclose such data, and the contractor or subcontractor or subcontractor asserting the restriction is notified of such release, disclosure or use. This legend, together with the indications of the portions of this data which are subject to such limitations, shall be included on any reproduction hereof which includes any part of the portions subject to such limitations.

THIS TECHNICAL REPORT HAS BEEN REVIEWED AND IS APPROVED FOR PUBLICATION.

Carole B. Christian

6/7/02

**REPORT DOCUMENTATION PAGE**Form Approved  
OMB No. 074-0188

Public reporting burden for this collection of information is estimated to average 1 hour per response, including the time for reviewing instructions, searching existing data sources, gathering and maintaining the data needed, and completing and reviewing this collection of information. Send comments regarding this burden estimate or any other aspect of this collection of information, including suggestions for reducing this burden to Washington Headquarters Services, Directorate for Information Operations and Reports, 1215 Jefferson Davis Highway, Suite 1204, Arlington, VA 22202-4302, and to the Office of Management and Budget, Paperwork Reduction Project (0704-0188), Washington, DC 20503

<b>1. AGENCY USE ONLY (Leave blank)</b>		<b>2. REPORT DATE</b> October 2001	<b>3. REPORT TYPE AND DATES COVERED</b> Annual (1 Oct 00 - 30 Sep 01)	
<b>4. TITLE AND SUBTITLE</b> Frequency-Domain Optical Mammography			<b>5. FUNDING NUMBERS</b> DAMD17-99-1-9218	
<b>6. AUTHOR(S)</b> Sergio Fantini, Ph.D.				
<b>7. PERFORMING ORGANIZATION NAME(S) AND ADDRESS(ES)</b>  Tufts University Medford, Massachusetts 02155  E-mail: sergio.fantini@tufts.edu			<b>8. PERFORMING ORGANIZATION REPORT NUMBER</b>	
<b>9. SPONSORING / MONITORING AGENCY NAME(S) AND ADDRESS(ES)</b>  U.S. Army Medical Research and Materiel Command Fort Detrick, Maryland 21702-5012			<b>10. SPONSORING / MONITORING AGENCY REPORT NUMBER</b>	
<b>11. SUPPLEMENTARY NOTES</b> Report contains color				
<b>12a. DISTRIBUTION / AVAILABILITY STATEMENT</b> Distribution authorized to U.S. Government agencies only (proprietary information, Oct 01). Other requests for this document shall be referred to U.S. Army Medical Research and Materiel Command, 504 Scott Street, Fort Detrick, Maryland 21702-5012.				<b>12b. DISTRIBUTION CODE</b>
<b>13. ABSTRACT (Maximum 200 Words)</b> This research project involves the analysis of a clinical data set of frequency-domain optical mammograms (~150 patients) to assess the performance of this approach to breast cancer detection. The analysis of the breast images is complemented by theoretical and experimental studies to characterize the proposed algorithms of image processing. During the second year of this research project, we have significantly refined the perturbation approach that we started developing at the end of the first year to exploit the spectral information of the optical mammograms. The theoretical basis of this method, which is inspired by perturbation theory but is of much more general applicability than perturbation theory, is now well characterized. We have performed optical experiments on tissue-like synthetic samples to experimentally test the effectiveness of our new method for the case of optical inclusions having various sizes, shapes, and optical contrast. Furthermore, we have devised a new approach for the analysis of single-wavelength images that is aimed at identifying the regions of interest for which a spectral examination is performed. We are now in the final stage of characterization of this new scheme of image processing which will then be applied to the whole dataset of optical mammograms.				
<b>14. SUBJECT TERMS</b> optical mammography, near-infrared imaging, photon diffusion, optical tomography, near-infrared tissue spectroscopy				<b>15. NUMBER OF PAGES</b> 86
				<b>16. PRICE CODE</b>
<b>17. SECURITY CLASSIFICATION OF REPORT</b> Unclassified	<b>18. SECURITY CLASSIFICATION OF THIS PAGE</b> Unclassified	<b>19. SECURITY CLASSIFICATION OF ABSTRACT</b> Unclassified	<b>20. LIMITATION OF ABSTRACT</b> Unlimited	

NSN 7540-01-280-5500

Standard Form 298 (Rev. 2-89)  
Prescribed by ANSI Std. Z39-18  
298-102

## Table of Contents

Cover.....	
SF 298.....	2
Table of Contents.....	3
Introduction.....	4
Body.....	4
Key Research Accomplishments.....	14
Reportable Outcomes.....	16
Conclusions.....	16
References.....	17
Appendices.....	17

## INTRODUCTION

This research project involves the analysis of an existing clinical set (~150 patients) of frequency-domain optical mammograms to assess the performance of this approach to breast cancer detection. The analysis of the breast images is complemented by theoretical and experimental studies to characterize the proposed algorithms of image processing. The objective of this research is to identify the strengths and the weaknesses of the current instrument design, and to guide the design of new optical instrumentation for breast cancer detection.

## BODY

### Approved statement of work

The approved statement of work for this project is the following:

#### *Task 1.*

Compute and analyze the edge-corrected optical mammograms for all 150 patients (**Months 1-18**)

- a. Install the optical mammography software for the SUN workstation;
- b. Build the edge-effect-corrected images ( $N$ -images) from the amplitude and phase images;
- c. Carry out a comparison between the  $N$ -images and the tumor diagnosis for each patient;
- d. Analyze the wavelength dependence of the  $N$  parameter and the ac amplitude for different kinds of tumors;
- e. Collect a printed summary of all the 2,400  $N$ -images (150 patients, 2 breasts, 2 projections, 4 wavelengths) and the spectral features of all the tumors.

#### *Task 2.*

Perform the optical measurements on breast-like phantoms (**Months 19-24**)

- a. Prepare the breast-like phantoms (optical inhomogeneities + strongly scattering background);
- b. Collect and analyze the optical data;
- c. Repeat the experiment for a variety of sizes, shapes, optical contrasts, and inhomogeneous backgrounds.

#### *Task 3.*

Apply the method for the quantification of the tumor optical properties and construct the spectral chart for benign and malignant tumors (**Months 25-36**)

- a. Find the optical properties, and the hemoglobin-related parameters of the tumors;
- b. Build charts of benign and malignant regions in the  $\mu_a$ - $\mu_s'$  plane at four wavelengths;
- c. Determine whether malignant tumors show a specific spectral signature.

The first Grant period (year 01) was devoted to Task 1, and the results obtained were reported in the first year annual report. The second Grant period (year 02) was devoted to an extension of Tasks 1b and 1d and to Task 2.

### Task 1.b.

During year 01, we have obtained the so-called N-images for the whole dataset of optical mammograms. We briefly recall that the N-images are the result of an algorithm of image processing previously developed by us to minimize the effect of the breast thickness variability on the optical mammograms. The resulting images display a dimensionless parameter (called N) that is indicative of the optical density of the breast. We have found that N-images enhance the tumor detectability with respect to amplitude or phase images (i.e. with respect to images obtained from the raw optical data). After having examined the results for the whole dataset, we have found that all of the outstanding image regions associated with cancer, benign tumors, and blood vessels are characterized by an increased value of N. Such an increased value (peak) is always associated with a negative second spatial derivative. On the contrary, we have observed that areas that introduce edge effects (i.e. the artifacts associated with the breast thickness reduction by the edge of the breast image) are usually associated with a positive second spatial derivative of N.

As a result of the above findings, during year 02, we have started developing a new scheme of image processing based on the second derivative of N. This image processing approach consists of the following steps:

- I) Smooth the original N image by a low-pass spatial filter;
- II) Calculate the average of the second spatial derivative along eight directions through each image pixel ( $N''$ );
- III) Set all of the image pixels corresponding to a positive value of  $N''$  to white;
- IV) Set all of the pixels out of the breast to black;
- V) Display the image pixels with  $N'' < 0$  using a gray scale palette where white corresponds to  $N'' = 0$  and black corresponds to the maximum value of  $N''$ .

This algorithm of data processing keeps all of the strengths of the N-imaging and further improves on the quality of the image display. In fact, (a) the correction of the edge artifacts afforded by the N-image is further improved by taking the second derivative (because the edge zone will be typically set to white); (b) the automatic generation of N-images, which is a very important feature for the practical examinations of the images in a clinical setting, is also featured by the second derivative images; (c) secondary peaks in the N-images, which may be buried within the main peak, appear with sharper contrast in  $N''$  images, and (d) the shape of the areas of increased N are much better identified in the  $N''$  images rather than the N images. Figure 1 reports representative N images of the optical mammograms at 690 nm collected on a patient affected by cancer. The cancer, 3 cm in size, appears as a blurred region of higher N value in the craniocaudal (cc) and oblique (ob) views of the left (l) breast. No evident structures are visible in the N-images for the right breast. Figure 2 reports the  $N''$  image. The cancer appears now with a much better defined shape in the left breast, while new structures become evident in the right and left breast mammograms. In particular, we assign most of the structures that appear in the right breast  $N''$  images to blood vessels.

### Task 1.d.

During year 01, we have developed a perturbation approach, based on diffusion theory, to assign an absorption perturbation to each optical inhomogeneity detected in the breast. This perturbation approach is based on the fact that the absorption perturbation  $\Delta\mu_a$  (to within an unknown wavelength independent factor C) can be written as:

$$C\Delta\mu_a(\lambda) = \frac{1}{\mu'_{s0}(\lambda)} \cdot \frac{\Delta I}{I_0}(\lambda) \quad (1)$$

where  $\mu'_{s0}$  is the average reduced scattering coefficient of healthy breast tissue,  $I_0$  is the unperturbed optical intensity, and  $\Delta I$  is the measured intensity perturbation. Finally, we have fitted the spectrum of the absorption perturbation with a linear combination of the extinction spectra of oxy- and deoxy-hemoglobin. By considering the oxy- and deoxy-hemoglobin concentrations ( $[\text{HbO}_2]$  and  $[\text{Hb}]$ , respectively) as fitting parameters, we can translate the spectral information into the tumor oxygenation (given by  $[\text{HbO}_2]/([\text{Hb}] + [\text{HbO}_2])$ ).

During year 02, we have continued the spectral study by expanding the analysis performed during year 01 in two different ways:

- 1) We have observed that in the perturbation limit, the peak value of the second derivative of  $N$  ( $N''_{\text{max}}$ ) is proportional to the absorption perturbation introduced by the tumor. Therefore, we have performed the fit of the spectrum of  $N''(\lambda)$  (as described above) to find an oxygenation index (OI). This oxygenation index, which in a real perturbation case would coincide with the hemoglobin saturation at the tumor, is only qualitatively related to the oxygenation because real tumors are typically beyond the validity of perturbation theory. Of course, we only calculate the oxygenation index (OI) at the pixels where the second derivative is negative (gray areas in Fig. 2). If we now identify with false colors the regions with lowest values of oxygenation index, we find that we may be able to discriminate blood vessels from cancer. This is the case for our representative patient, for whom we report in Fig. 3 the false color OI images. In fact, the lowest value (blue in this color representation) only occurs at the cancer location. We are now in the process of testing this new idea on a subset of optical mammogram, to extend it subsequently to the whole dataset.
- 2) We have found that the right-hand side of Eq. (1) is not simply proportional to the absorption perturbation ( $\Delta\mu_a$ ) once we are not within the limits of perturbation theory. However, we have found that  $(\Delta I)_{\text{max}}/I_0$  is indeed only a function of the product  $\mu'_{s0}\Delta\mu_a$  even in cases beyond the realm of perturbation theory (under the assumption that  $\Delta\mu'_s = 0$ , as approximately true for breast tumors). We have found this result by calculating  $-(\Delta I)_{\text{max}}/I_0$  for the case of a large sphere (not a small perturbation) and various values of  $\mu'_{s0}$  and  $\Delta\mu_a$ . The fact that  $-(\Delta I)_{\text{max}}/I_0$  only depends on the product  $\mu'_{s0}\Delta\mu_a$  is illustrated in Fig. 4(a), while Fig. 4(b) shows the independence (to a good approximation) of  $-(\Delta I)_{\text{max}}/I_0$  on the background absorption  $\mu_{a0}$ . This has prompted the development of a new idea, which consists of identifying two wavelengths  $\lambda_1$  and  $\lambda_2$  such that  $(\Delta I)_{\text{max}}/I_0$  is the same at the two wavelengths. It turns out that because of the shape of the hemoglobin spectrum and the spectrum of typical breast tissue, this condition can be fulfilled to a good approximation using two wavelengths that are at least 50 nm apart (otherwise the approach has a large error). The basic idea is that at these two wavelengths, since  $(\Delta I)_{\text{max}}/I_0$  is the same, then also the product  $\mu'_{s0}\Delta\mu_a$  is the same, and therefore we can write:

$$\frac{\Delta\mu_a(\lambda_1)}{\Delta\mu_a(\lambda_2)} = \frac{\mu'_{s0}(\lambda_2)}{\mu'_{s0}(\lambda_1)} \quad (2)$$

This translates a measurement of the spectral ratio of the background reduced scattering (which can be performed with frequency-domain methods) into a measurement of the spectral ratio of the absorption perturbation, which is all that is needed for a quantitative



Patient 310: 3 cm cancer

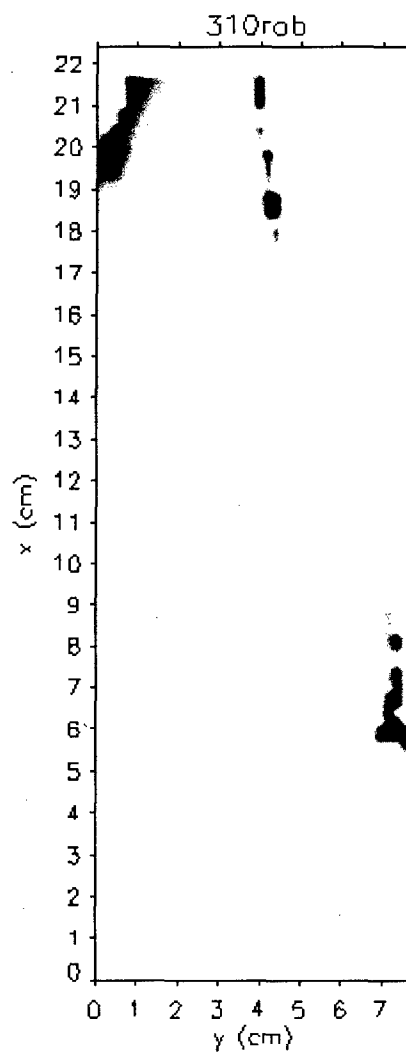
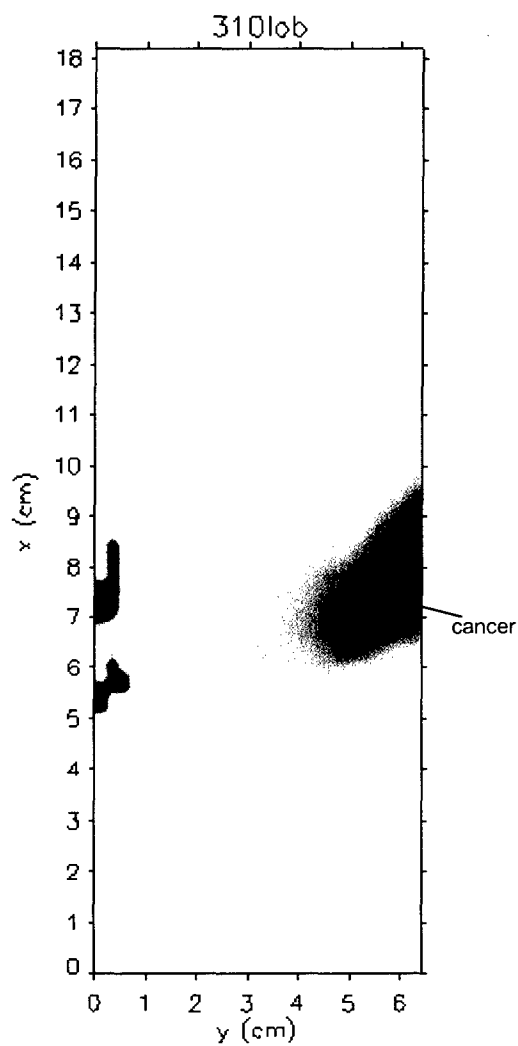
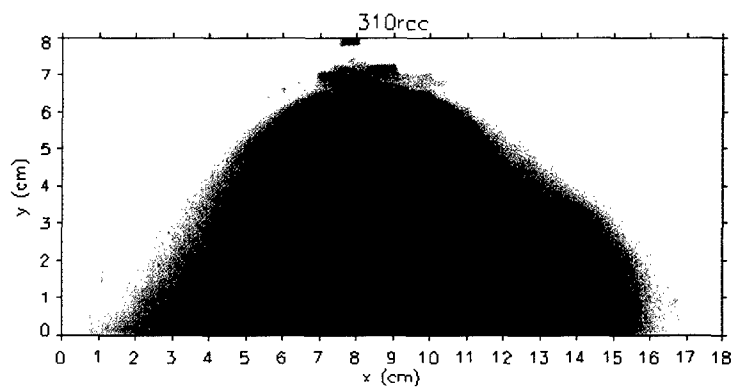
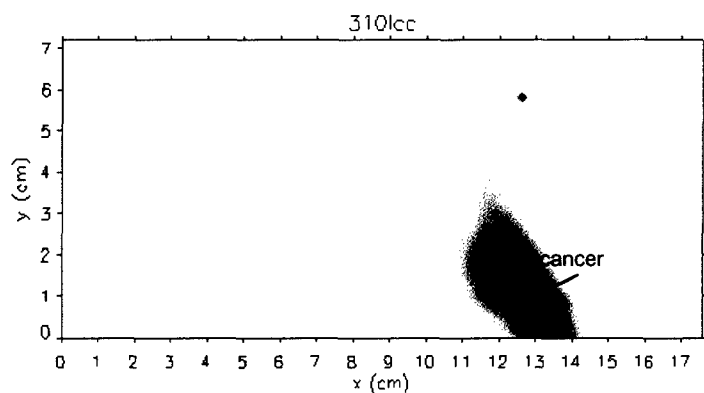
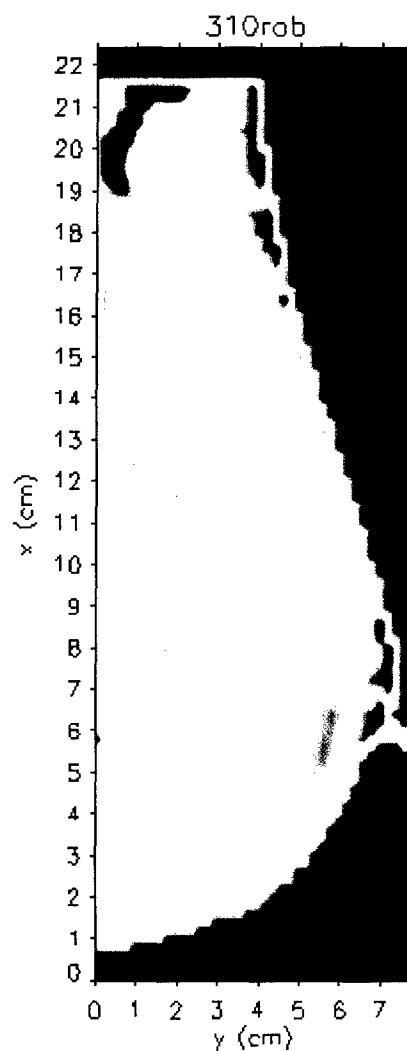
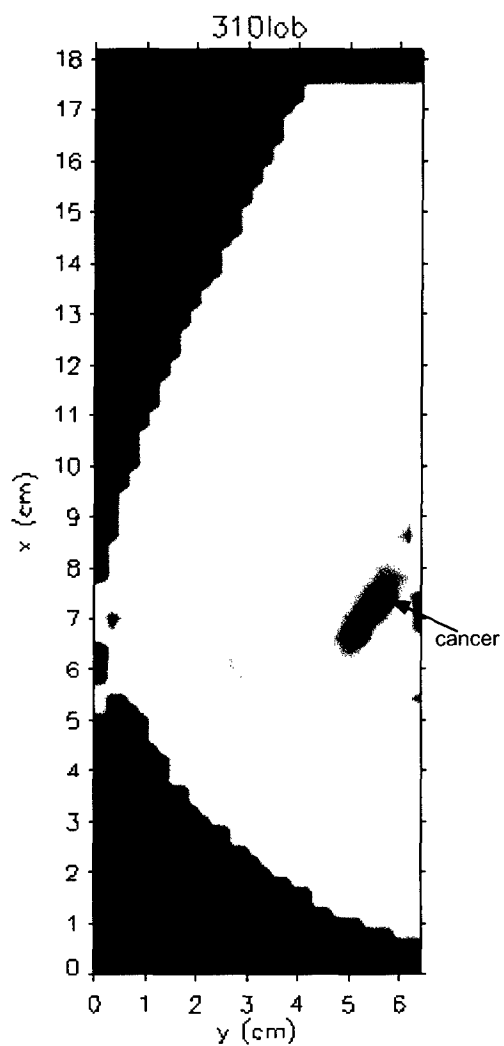
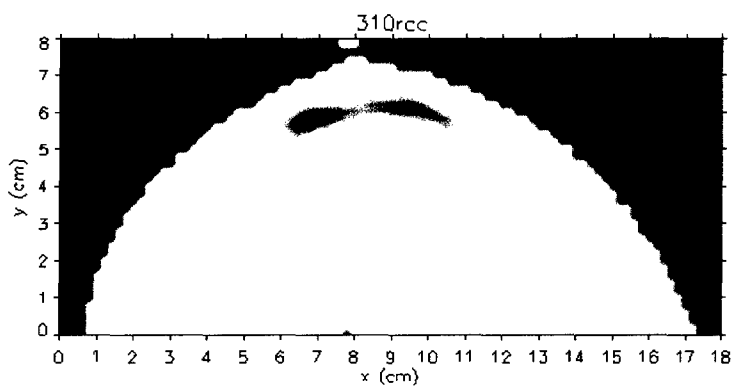
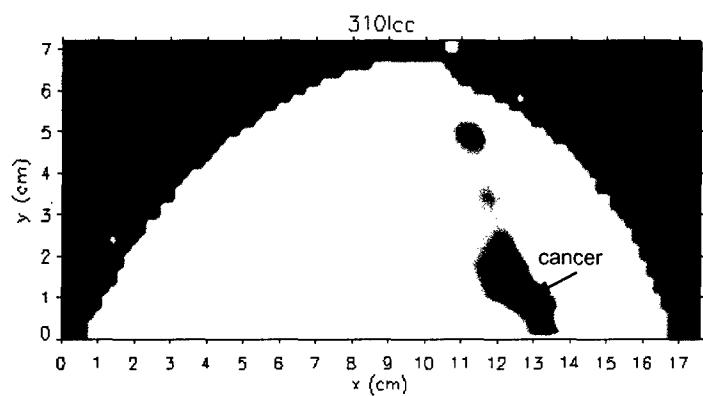


Figure 1. Original N-image ( $\lambda = 690$  nm).

Patient 310: 3 cm cancer



**Figure 2.** Second derivative ( $N''$ ) image.  $N'' < 0$  displayed in gray-scale (darker = more negative).  $N'' \geq 0$  set to white; background set to black.

Patient 310: 3 cm cancer

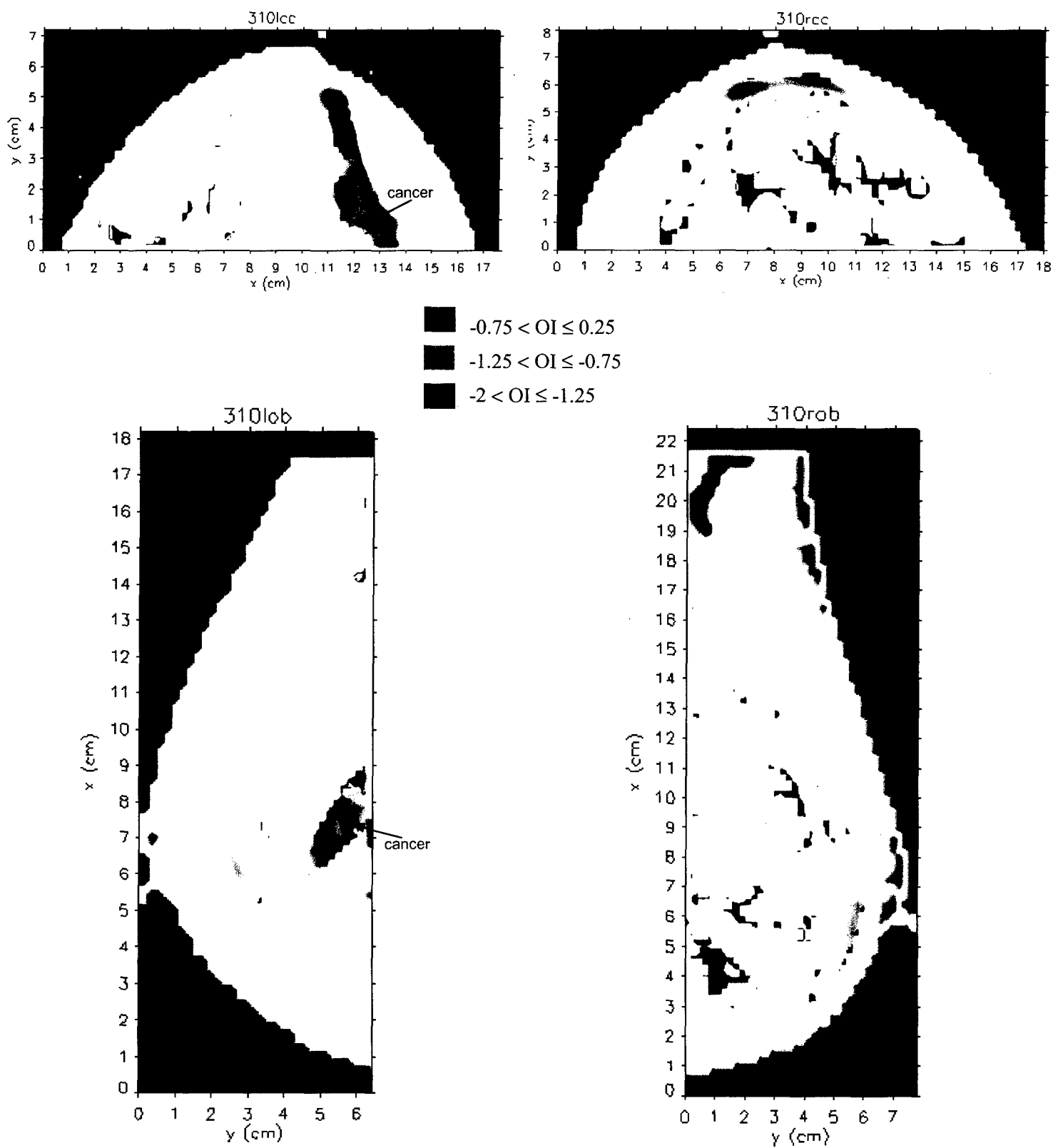


**Figure 3.** Oxygenation index (OI) image. OI values in range  $-2 \rightarrow 0.25$  displayed in color.

measurement of the tumor oxygenation. Even though the current dataset does not allow us to identify the two wavelengths  $\lambda_1$  and  $\lambda_2$  from a highly resolved spectrum (only four wavelengths are available), we can still try to extrapolate the data at the four wavelengths to a continuous spectrum to obtain indications on the applicability of our idea to clinical data. At any rate, this new approach is in line with the broad objective of this project of guiding the design of new optical instrumentation for breast cancer detection.

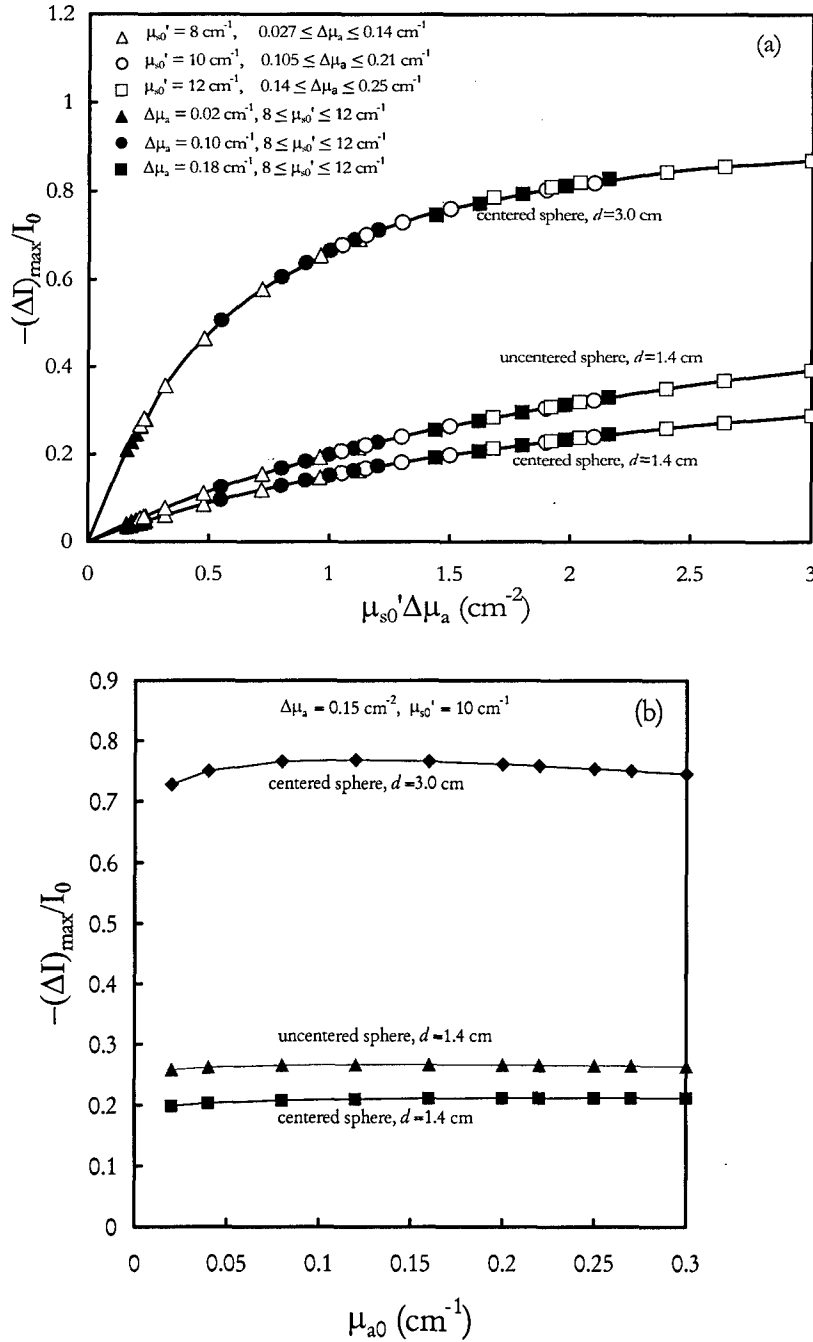


Fig. 4. Theoretical calculations of the dependence of  $-(\Delta I)_{\max}/I_0$  for a spherical inclusion on the background optical properties and on the absorption perturbation. The scattering perturbation is assumed to be zero, because the scattering contrast of tumors is typically much smaller than their absorption contrast.

## Task 2

We have performed a laboratory study that was divided into three segments: (1) preparation and optical characterization of inclusions to simulate tumors, (2) preparation and optical characterization of the background material (a highly-scattering, liquid, infinite medium), and (3) experimental procedure to investigate that  $\Delta I / I_0|_{\max}$  depends solely on the product  $\mu'_{s0}\Delta\mu_a$  (as theoretically predicted in the case of a spherical inclusion) for the case of cylindrical and irregularly-shaped objects embedded in a uniform turbid medium. Segments (1) and (2) pertain to Task 2a, while segment (3) pertains to tasks 2b and 2c.

### Task 2a

(1) Inclusions were comprised of a mixture of General Electric silicones, model No. RTV615 (clear) and model No. RTV11 (white). The white silicone was used as the scattering material and black India ink was used as the absorber. Two different mixtures were prepared with different optical properties, (the first with  $\mu_a \sim 0.05\text{--}0.08\text{ cm}^{-1}$  and  $\mu'_s \sim 9\text{--}12\text{ cm}^{-1}$  and the second with  $\mu_a \sim 0.11\text{--}0.19\text{ cm}^{-1}$  and  $\mu'_s \sim 9\text{--}11\text{ cm}^{-1}$  over the wavelength range of 752-840 nm considered by us) to cover the range of  $\Delta\mu_a$  from  $0.01\text{ cm}^{-1}$  to  $0.2\text{ cm}^{-1}$  that is representative of breast lesions *in vivo*. The optical properties were measured using frequency-domain data. The inclusion material was formed into irregular shapes (by cutting cylindrical shapes with razor blades) and into a 10 cm-long cylinder using the two different mixtures, thus creating two different sets of the same sizes and shapes. The cylinder had a diameter of 1.0 cm, while the irregular shapes were created to have the same volumes as spheres with 1.0 cm diameter ( $V = 1.4\text{ cm}^3$ ) and 1.4 cm diameter ( $V = 0.5\text{ cm}^3$ ), respectively.

(2) The background medium was comprised of 1 liter of Liposyn (10% lipids content) to 8 Liters of deionized water and was contained inside a rectangular vessel with dimensions of 27 cm width, 32 cm length, and 13 cm height. Frequency-domain measurements of  $\mu_{a0}$  over the wavelengths used by us ranged from  $0.006\text{ cm}^{-1}$  to  $0.04\text{ cm}^{-1}$  and those of  $\mu'_{s0}$  ranged from  $9\text{ cm}^{-1}$  to  $15\text{ cm}^{-1}$ . These value of the optical properties match typical near-infrared absorption and scattering coefficients in breast tissue ( $\mu_a(\text{breast}) \sim 0.03\text{ cm}^{-1}$  and  $\mu'_s(\text{breast}) \sim 12\text{ cm}^{-1}$ ) [1].

### Tasks 2b and 2c

(3) The experimental procedure to verify that  $\Delta I / I_0|_{\max}$  depends on the product  $\mu'_{s0}\Delta\mu_a$  was based on the arrangement shown in Fig. 5. A frequency-domain, near-infrared spectrometer (ISS, Inc., Champaign, IL, Model No. 96208) housed and controlled the laser sources and optical detectors used to obtain the measurements. The sources were laser diodes at six discrete wavelengths (752, 778, 786, 813, 830 and 840 nm) and the optical detector was a photomultiplier tube (Hamamatsu Photonics R928). The sources were intensity-modulated at a frequency of 110 MHz, multiplexed at a rate of 27 Hz for discrimination at the detector, and were coupled to 400  $\mu\text{m}$  core-diameter optical fibers that were collected into a fiber bundle with rectangular cross-section 1.2 mm in width and 3 mm in length. The detector was coupled to another fiber bundle of circular cross-section, 3 mm internal diameter. The ends of the illumination and collection fiber bundles were fully immersed in the Liposyn mixture to simulate an infinite medium. The source fiber and the collection fiber were then moved in tandem, remaining collinear all the time, at a rate of 0.65 mm/second. Data was acquired at every 0.5 seconds providing a measurement every 325  $\mu\text{m}$  over a scanning range of

14 cm. The source-detector separation for these experiments remained a constant 6 cm, which is representative of the thickness of a slightly compressed breast. Inclusions of different sizes and shapes were then suspended in the medium equidistant from the source and detector using Pasteur pipettes to hold them in place. The pipettes were filled with background medium to reduce the optical perturbation they might cause.

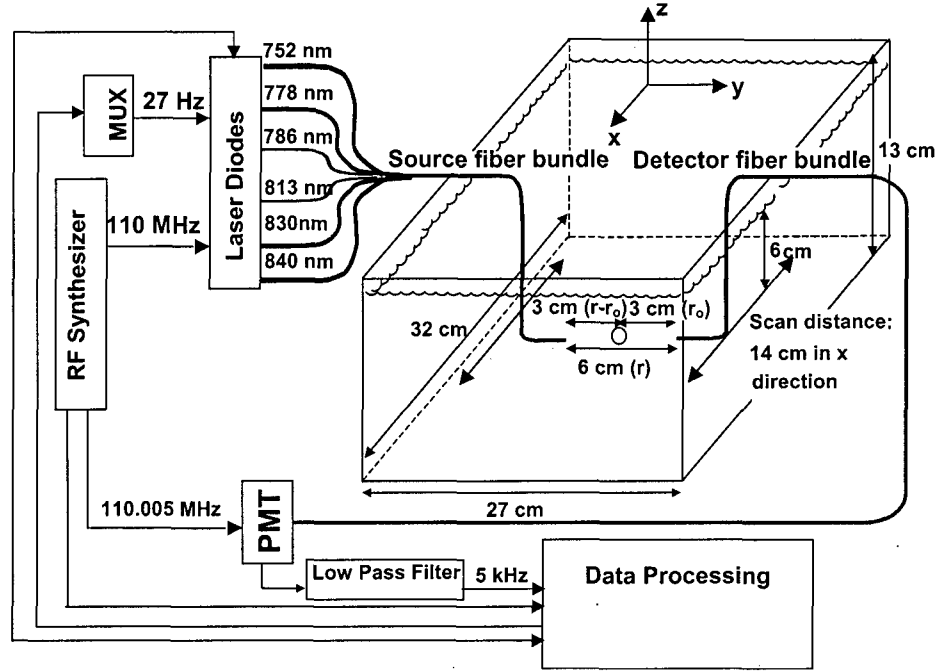


Fig. 5. Experimental setup for the optical measurements in a tissue-like strongly scattering medium containing tumor-simulating inclusions. MUX: multiplexer, PMT: photo-multiplier tube, RF: radio frequency.

### Results

The experimental results for  $\Delta I / I_0|_{\max}$  as a function of the product  $\mu_{s0}' \Delta \mu_a$  are reported in Fig. 6(a) for the irregularly-shaped inclusions, and in Fig. 6(b) for the cylindrical inclusion. In both cases, the fact that the experimental data of  $-\Delta I / I_0|_{\max}$  for a range of values of  $\mu_{s0}'$  and  $\Delta \mu_a$  are distributed along a single curve as a function of the product  $\mu_{s0}' \Delta \mu_a$  is indicative of the dependence of  $\Delta I / I_0|_{\max}$  on the product  $\mu_{s0}' \Delta \mu_a$ . In Figs. 6(a) and 6(b), the functions of  $\mu_{s0}' \Delta \mu_a$  are indicated by arbitrary continuous lines. The small deviations of the experimental points from the arbitrary smooth lines are assigned to experimental errors and to the approximate fulfillment of the condition  $\Delta \mu_s' = 0$ . These experiments confirm our hypothesis that  $\Delta I / I_0|_{\max}$  is only a function of the product  $\mu_{s0}' \Delta \mu_a$  even for objects with a relatively large size, cylindrical or irregular shape, and relatively high absorption contrast.

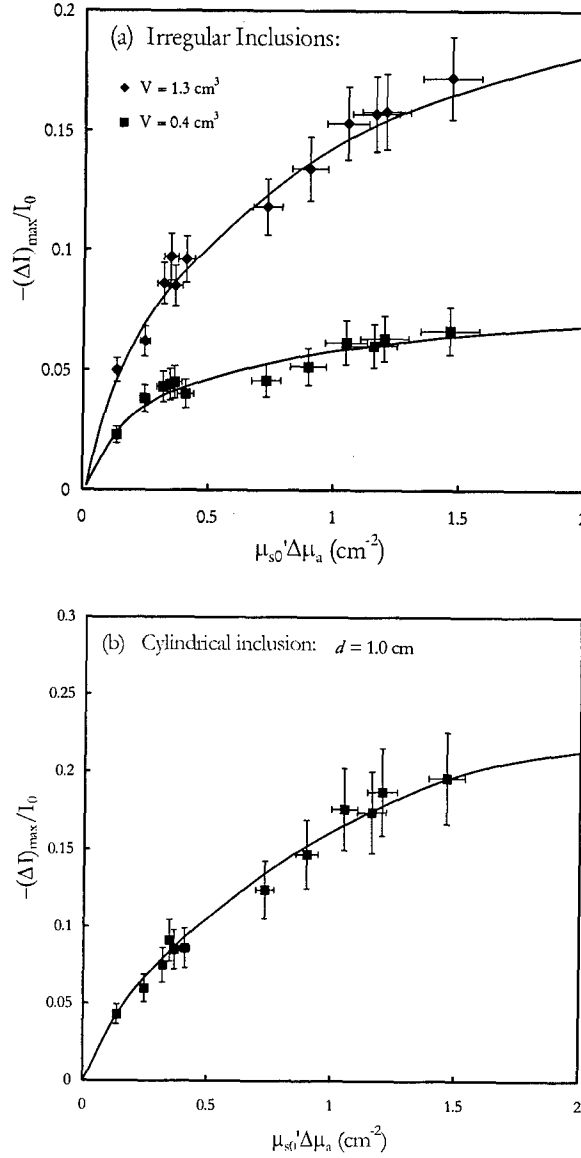


Fig. 6. Experimental results of the dependence of  $-(\Delta I)_{\max}/I_0$  on the product of the background scattering coefficient and the absorption perturbation. (a) Irregularly shaped inclusions, (b) cylindrical inclusion.

The relevance of these findings is illustrated in Fig. 7, which shows that we can accurately measure the oxygen saturation of tumors (modeled here by spherical inclusions) even if their size and absorption contrast is well beyond the limits of perturbation theory. We have computed the values of  $\Delta I/I_0|_{\max}$  at nine wavelengths (680, 700, 720, 730, 758, 780, 800, 840, and 880 nm) for a spherical inclusion in a case that mimics a realistic condition in optical mammography. The background scattering and absorption spectra were set equal to reported spectra for healthy breast tissue [2], we set the hemoglobin concentration of the embedded lesion to a value 60  $\mu$ M higher than that in the background, and we varied the hemoglobin saturation of the sphere over the full range 0-100%. We have compared the measurements of hemoglobin saturation obtained (1) by using perturbation theory [i.e. Eq. (1)] at two fixed wavelengths and (2) by using our method [i.e.

Eq. (2) with a linear correction that takes into account deviations from the condition  $(\Delta I)_{\max}/I_0(\lambda_1) = (\Delta I)_{\max}/I_0(\lambda_2)$  at two wavelengths that depend on the oxygenation of the inclusion. Both approaches require knowledge of the background reduced scattering coefficient, which can be measured with frequency-domain methods. The results of the perturbation analysis for a number of wavelength pairs are shown in Fig. 7(a) for a 1.4 cm-diameter sphere (on the mid-line between source and detector), in Fig. 7(c) for a 3.0 cm-diameter sphere (on the mid-line between source and detector), and in Fig. 7(e) for a 1.4 cm diameter sphere off the mid-line by 1.5 cm. The results of our new method are shown in Fig. 7(b) (sphere diameter: 1.4 cm; on the mid-line), Fig. 7(d) (sphere diameter: 3.0 cm; on the mid-line), and Fig. 7(f) (sphere diameter: 1.4 cm; 1.5 cm off the mid-line). These results show that our new method can achieve accurate measurements of the oxygenation of spherical regions over a wide range of oxygenation values (in particular from 40 to 100%) and independent of the size and location of the sphere.

### **Additional research**

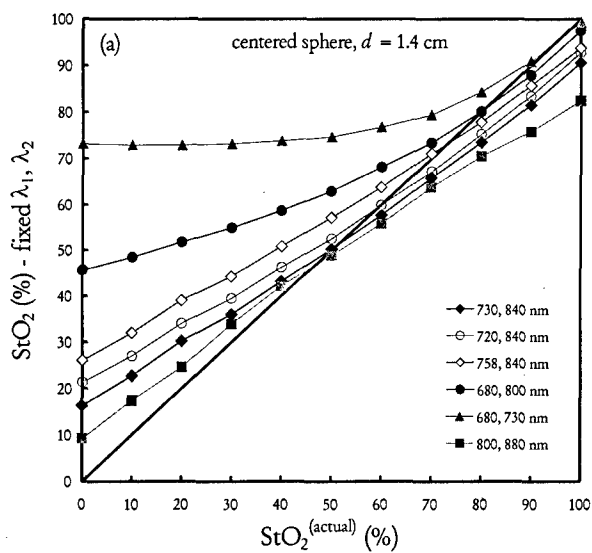
Some of our results on the measurements of oxygenation levels from spectral measurements have been developed in conjunction with an effort to measure the oxygenation of the venous compartment in the skeletal muscle of animal models (piglets) and human subjects. Our approach and findings in this area are reported in the manuscripts enclosed with this report.

## **KEY RESEARCH ACCOMPLISHMENTS**

- Development of a new scheme of image processing based on the second spatial derivative of the N images.
- Computation of a tumor oxygenation index (OI) based on the spectral dependence of the second derivative of N at the tumor.
- Combination of the above two points into a composite false-color breast image containing structural information (from the second derivative of N) and functional information (OI).
- Development of a new method to measure the tumor oxygenation from an appropriate choice of a wavelength pair that depends on the tumor oxygenation.
- Theoretical tests of the new method using the analytical solution for a spherical inclusion (tumor) embedded in a turbid medium (breast tissue).
- Experimental tests of the new method on breast-simulating turbid media.



Calculations using a fixed wavelength pair over the full  $\text{StO}_2$  range.



Calculations using wavelength pairs appropriately chosen for each  $\text{StO}_2$  value.

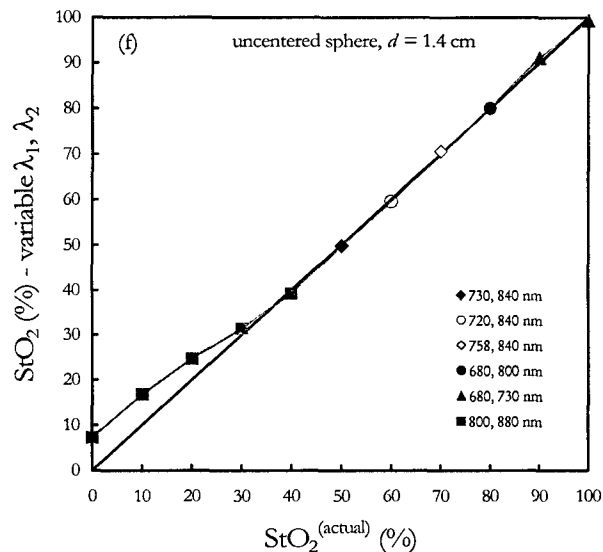
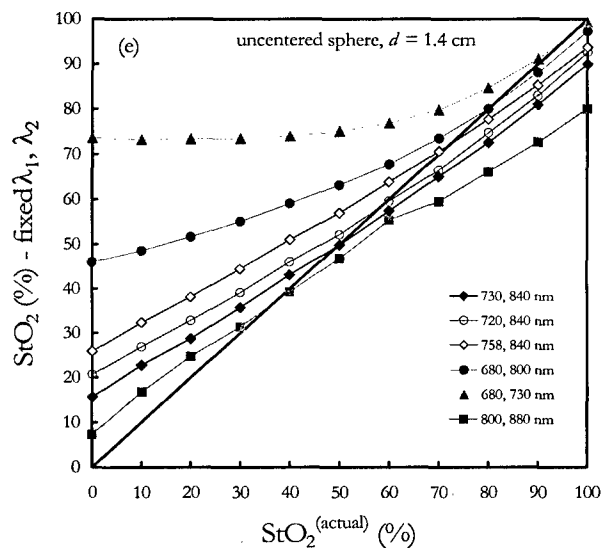
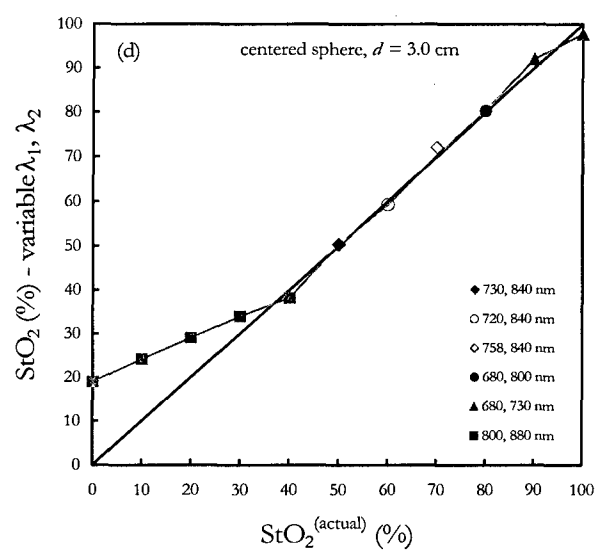
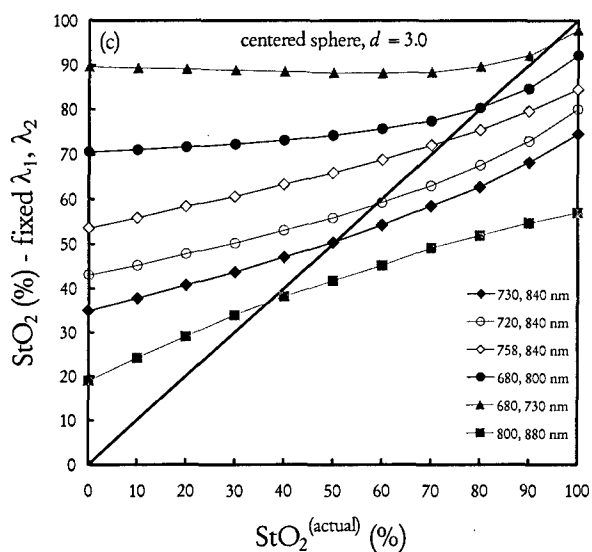
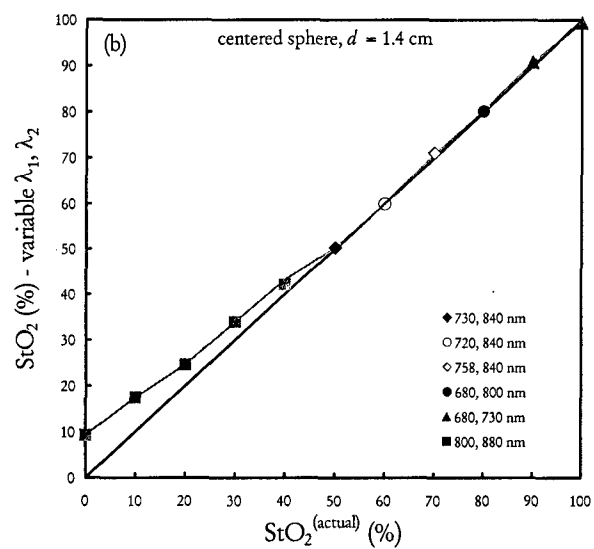


Fig. 7

Fig. 7 (previous page). Analysis of the effectiveness of our new method for measuring the tumor oxygenation (right panels) with respect to first order perturbation theory using fixed wavelength pairs (left panels). The calculated oxygenation values ( $y$  axes) are correlated with the actual oxygenation values ( $x$  axes) used in the theoretical calculation of the data.

## REPORTABLE OUTCOMES

### **Manuscripts (three copies of these manuscripts are enclosed with this report)**

S. Fantini and M. A. Franceschini, "Frequency-Domain Techniques for Tissue Spectroscopy and Imaging," in *Optical Biomedical Diagnostics*, V. V. Tuchin, Ed., (SPIE Press, Bellingham, WA, 2001), Chapter 7, (*accepted for publication*).

M. A. Franceschini, D. A. Boas, A. Zourabian, S. G. Diamond, S. Nadgir, D. W. Lin, J. B. Moore, and S. Fantini, "Near-Infrared Spiroximetry: Non-Invasive Measurement of Venous Saturation in Piglets and Human Subjects," *J. Appl. Physiol.*, (*accepted for publication*).

M. A. Franceschini, A. Zourabian, J. B. Moore, A. Arora, S. Fantini, and D. A. Boas, "Local Measurement of Venous Saturation in Tissue with Non-Invasive, Near-Infrared Respiratory-Oximetry," *Proc. SPIE* **4250**, 164-167 (2001).

Two manuscripts are currently in preparation. They will report our results in the areas of:

- 1) Quantitative oximetry of breast tumors with near-infrared spectral imaging;
- 2) Second derivative imaging combined with oxygenation imaging.

## CONCLUSIONS

We have developed a new image processing method (second derivative imaging) to better display the optical mammograms. This new method results in further improvement of contrast and detection of breast tumors with respect to the previous N-imaging approach. We have complemented this improved structural imaging approach with a functional imaging approach based on an oxygenation index computed from spectral features of the second derivative images. We have also refined the perturbative approach for spectral analysis developed during year 01. This refinement has led to a new method for measuring the tumor oxygenation with an excellent accuracy (from theoretical data) over the range of oxygenation 40-100%.

The relevance of our results is that single wavelength images that provide structural information can be superimposed with false color oxygenation images that provide functional information. Our new approach has the potential of quantifying the tumor oxygenation, so that optical discrimination of benign and malignant tumors may become feasible.

## REFERENCES

- [1] H. Heusmann, J. Kolzer, and G. Mitic, "Characterization of female breasts *in vivo* by time resolved and spectroscopic measurements in near infrared spectroscopy," J. Biomed. Opt. **1**, 425-434 (1996)
- [2] R. Cubbedu, A. Pifferi, P. Taroni, A. Torricelli, and G. Valentini, "Noninvasive absorption and scattering spectroscopy of bulk diffusive media: an application to the optical characterization of human breast," Appl. Phys. Lett. **74**, 874-876 (1999).

## APPENDIX

The appendix contains three copies each of the three manuscript listed in the "reportable outcomes" section.

# Local measurement of venous saturation in tissue with non-invasive, near-infrared respiratory-oximetry

Maria Angela Franceschini<sup>a,b</sup>, Anna Zourabian<sup>b</sup>, John B. Moore<sup>b</sup>, Aradhana Arora<sup>a</sup>, Sergio Fantini<sup>a</sup>, and David A. Boas<sup>b</sup>

<sup>a</sup> Bioengineering Center, Department of Electrical Engineering and Computer Science, Tufts University, 4 Colby Street, Medford, MA 02155-6013, phone (617) 627-4321, e-mail: [mari@EECS.TUFTS.EDU](mailto:mari@EECS.TUFTS.EDU)

<sup>b</sup> NMR Center, Massachusetts General Hospital, Harvard Medical School, 13<sup>th</sup> Street Bldg. 149 (rm 2301), Charlestown, MA 02129

## ABSTRACT

We present preliminary results of non-invasive, near-infrared measurements of venous saturation (SvO<sub>2</sub>) on the leg muscle of three anesthetized piglets. We have quantified the local SvO<sub>2</sub> by analyzing the optical spectrum of the amplitude of the absorption oscillations synchronous with breathing. To induce a variation in the muscle SvO<sub>2</sub>, we performed measurements during a protocol involving a cyclic change in the fraction of oxygen inspired by the piglet over the range 10-100% (by volume). In all three piglets, we have found a good agreement between the SvO<sub>2</sub> values measured non-invasively with near-infrared spectroscopy (NIRS) and those measured invasively by the analysis of venous blood samples.

**Keywords:** Near-infrared, tissue spectroscopy, frequency-domain, pulse oximetry, venous saturation.

## 1. INTRODUCTION

The hemoglobin concentration in blood-perfused tissues shows temporal fluctuations that are induced by physiological and metabolic activity. For example, the arterial pulsation associated with the systolic-diastolic blood pressure variation induces hemoglobin concentration oscillations at the heartbeat frequency. These oscillations are exploited by pulse oximeters to measure the arterial saturation.<sup>1,2</sup> Other fluctuations on a longer time scale of seconds or tens of seconds are associated with vasomotion activity, heart rate fluctuations, and breathing.<sup>3-6</sup> Near-infrared tissue spectroscopy (NIRS), being exquisitely sensitive to the absorption of hemoglobin, is an effective tool to measure the hemoglobin concentration in tissues and its temporal fluctuations. Furthermore, one can optically discriminate the oxy- and deoxy-hemoglobin species because of their different near-infrared absorption spectra.

In this article, we present an optical study of the hemoglobin fluctuations at the breathing frequency in the leg muscle of newborn piglets. Under the hypothesis that the venous compartment gives the dominant contribution to the hemoglobin oscillations at the breathing frequency, we have used this oscillatory component to measure the venous saturation. This hypothesis was originally reported by Wolf *et al.*<sup>7</sup> This measurement of venous saturation is local, non-invasive, can be done continuously, and does not require any perturbation such as cuff occlusion, dye injection, or gas inhalation.

## 2. METHODS

### 2.1. Tissue spectrometer

The optical measurements were performed with a multi-channel tissue spectrometer operating in the frequency-domain (Model 96208, ISS, Inc., Champaign, IL).<sup>8,9</sup> For the measurements reported here, we employed two photomultiplier tube (PMT) detectors and eight laser diodes emitting at 633, 670, 691, 752, 778, 786, 830, and 840 nm. The eight light sources, which were intensity modulated at a frequency of 110 MHz, were electronically multiplexed at a rate of 100 Hz to time-share the two parallel PMT detectors. As a result, a complete acquisition cycle over the eight wavelengths took 80 ms. The laser diodes and the PMT's were all coupled to fiber optics. The eight individual source fibers, each 400  $\mu\text{m}$  in internal diameter, were closely arranged into a fiber bundle having a rectangular cross-section of  $3.5 \times 2.0 \text{ mm}^2$ . The detector fiber bundles were 1.5 mm in internal diameter (we also tested 3.0 mm fiber bundles and we found no significant difference with respect to the results obtained with the 1.5 mm bundles). The optical fibers were placed in contact with the skin of the piglet by means of a flexible, plastic probe. This probe arranged the tips of the source and detector fiber bundles along a line with the two detector bundles at distances of 1.0 and 2.0 cm, respectively, from the source bundle. The data processing and instrument control were performed by software running under Windows 98. This software allowed for the real-time display of the average intensity, amplitude, and phase data.

### 2.2. Measurement protocol

We measured three piglets. Each piglet was anesthetized (3-4% Isoflurane inhalation) and intubated. The animal was not ventilated and breathed freely throughout the experiment. Femoral cut-downs were performed into the left inferior femoral vein and artery to insert catheters for periodic arterial and femoral venous blood gas monitoring. The optical probe was always located on the right (non-catheterized) posterior leg, with one exception (piglet #3) where data were also collected on the catheterized leg (left) for comparison. On the first piglet (14 days old, 3.75 kg body weight) we performed two oxygenation cycles. Each cycle consisted of varying the fraction of inspired oxygen ( $\text{FiO}_2$ ) approximately every four minutes through the values of 40%, 15%, 10%, and 100% (by volume). During each specific value of  $\text{FiO}_2$  we acquired about 3,000 optical data points ( $4 \text{ min} \times [60 \text{ s/min}] / [80 \text{ ms/data point}]$ ). On the second piglet (16 days old, 5.5 kg body weight) we repeated the  $\text{FiO}_2$  cycle four times (after the first two cycles we moved the optical probe to a different location on the same leg). The only difference with respect to the  $\text{FiO}_2$  cycle performed on piglet #1 was that on piglet #2 we maintained each particular  $\text{FiO}_2$  level for about six minutes (i.e. about 4,500 data points). On the third piglet (15 days old, 5.39 kg body weight) we performed three  $\text{FiO}_2$  cycles where the  $\text{O}_2$  volume fraction assumed the sequential values of 40%, 20%, 17.5%, 15%, 12.5%, 10%, and 100%. Each  $\text{FiO}_2$  value was maintained for about six minutes. In all three piglets, an invasive measurement of  $\text{SvO}_2$  from a femoral vein blood sample was performed at the end of each  $\text{FiO}_2$  interval using a conventional blood gas analyzer (Instrumentation Laboratory, model 13040-11 pH/Blood Gas Analyzer). Throughout the experiment, we monitored the arterial pulsation, heart rate and arterial saturation ( $\text{SaO}_2$ ) with a commercial pulse oximeter (Nellcor, N-200) attached to the piglet's right foot, and the respiratory motion with a strain gauge belt (Sleepmate/Newlife Technologies, Resp-EZ) placed around the piglet's chest. The readings of the pulse oximeter and the strain gauge were recorded continuously and simultaneously with the collection of near-infrared data. Motion artifacts in the optical data were minimized by securing the piglet's leg to the operating table.

### 2.3. Data analysis

We used the modified Beer-Lambert law approach<sup>10</sup> to translate the temporal intensity changes into variations in the tissue absorption, under the assumption that the tissue scattering is slowly-varying. We continuously measured the optical pathlength using our frequency-domain data and diffusion theory. The mean pathlength was measured at the end of each  $\text{FiO}_2$  period by quantifying the average (over 1,000 points, or 80 s) absorption and reduced scattering coefficients of the tissue using the frequency-domain multi-distance method.<sup>11</sup> In this case, the multi-distance scheme was realized by the two detector fiber bundles at two different distances (1.0 and 2.0 cm) from the single source fiber bundle. The different fiber throughput and detector sensitivity for the two detector channels was accounted for by a preliminary calibration measurement on an optically characterized synthetic tissue-like sample. The validity of the calibration procedure was verified at the end of each measurement session by re-positioning the optical probe on the calibration sample. The measured values of the optical pathlengths in the piglet's leg at the eight wavelengths were updated every time the  $\text{FiO}_2$  was changed. This long integration time for the pathlength measurements (80 s) realized a low-pass filter that minimized the time-varying contributions from the hemoglobin oscillations resulting from the arterial pulsation and breathing. Furthermore, the multi-distance measurement scheme for the pathlength measurement provided some level of spatial averaging as well. By contrast, the optical data for the

measurement of venous saturation were acquired with an 80 ms temporal resolution and using a single source-detector distance (1 cm).

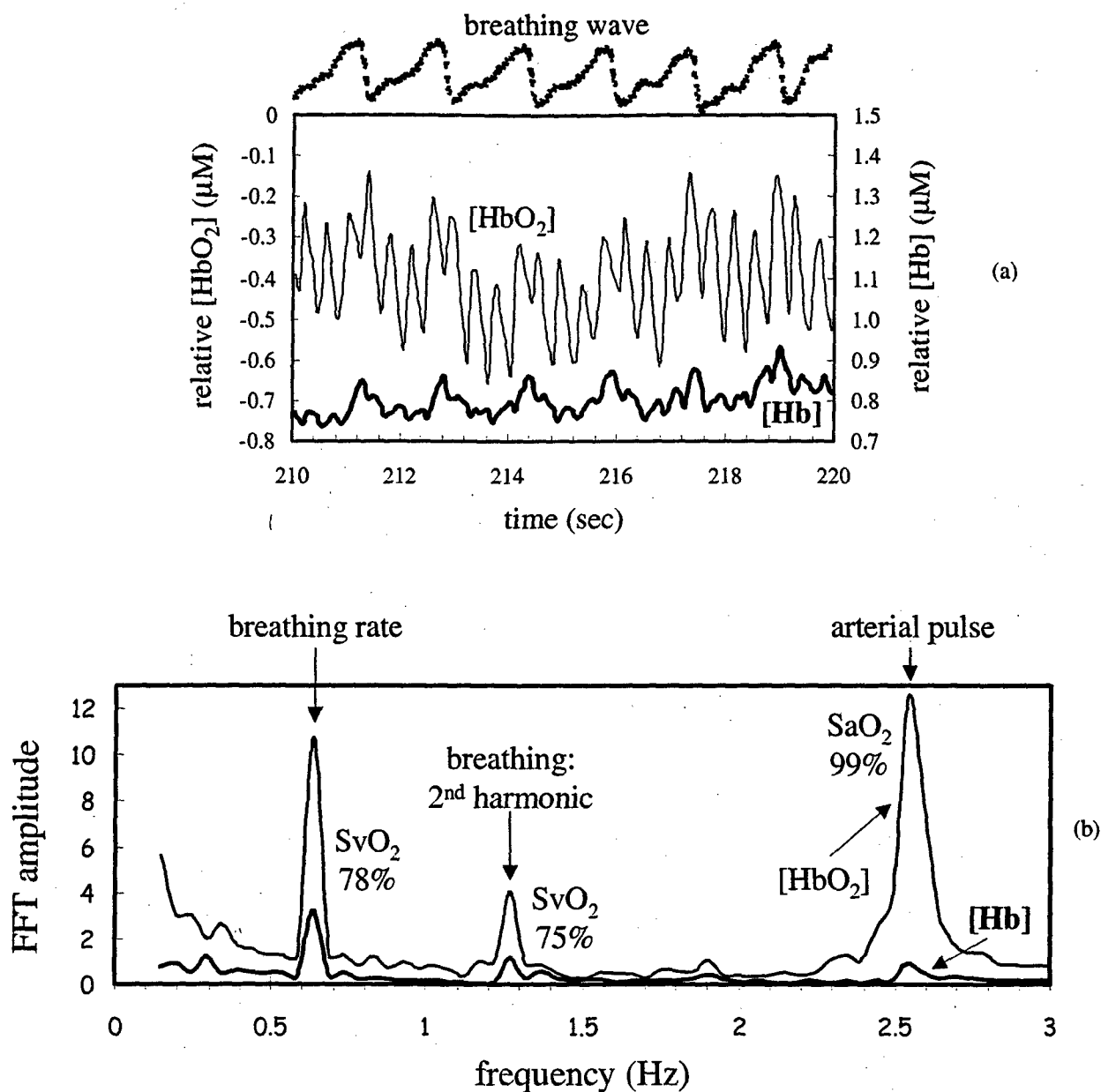
To compute the venous saturation, we measured the amplitude of the absorption oscillations at the breathing frequency at the eight wavelengths considered. We quantified the amplitude of the breathing-induced absorption oscillations by taking the sum of the amplitudes of the fast Fourier transform of  $\Delta\mu_a$  over the breathing band or its second harmonic. We evaluated the fast Fourier transform of  $\Delta\mu_a$  over 256 data points, corresponding to a time trace 20.5 s long, to achieve reliable and reproducible spectra from a number of breathing periods. Furthermore, we averaged about 800 successive Fourier transforms (each computed from a data set shifted by one data point with respect to the previous one), so that the total number of data points resulting in a single venous saturation reading was on the order of 1,000 (corresponding to a train of data 80 s long). This 80 s-long data set was chosen to be at the end of each  $\text{FiO}_2$  period. The spectrum of the amplitude of the absorption oscillations synchronous with breathing was fitted to a linear combination of the oxy- and deoxy-hemoglobin extinction spectra. The fitted parameters were the oscillatory concentrations of oxy-hemoglobin ( $[\text{HbO}_2]_{\text{osc}}$ ) and deoxy-hemoglobin ( $[\text{Hb}]_{\text{osc}}$ ). The hemoglobin saturation of the hemoglobin compartment oscillating synchronously with breathing is then given by  $[\text{HbO}_2]_{\text{osc}} / ([\text{HbO}_2]_{\text{osc}} + [\text{Hb}]_{\text{osc}})$ . We observe that this procedure can be applied to an oscillatory hemoglobin component at any frequency. At the heartbeat frequency, this procedure yields the arterial saturation.<sup>12</sup> Here, we apply it to the breathing frequency to obtain the venous saturation.

### 3. RESULTS

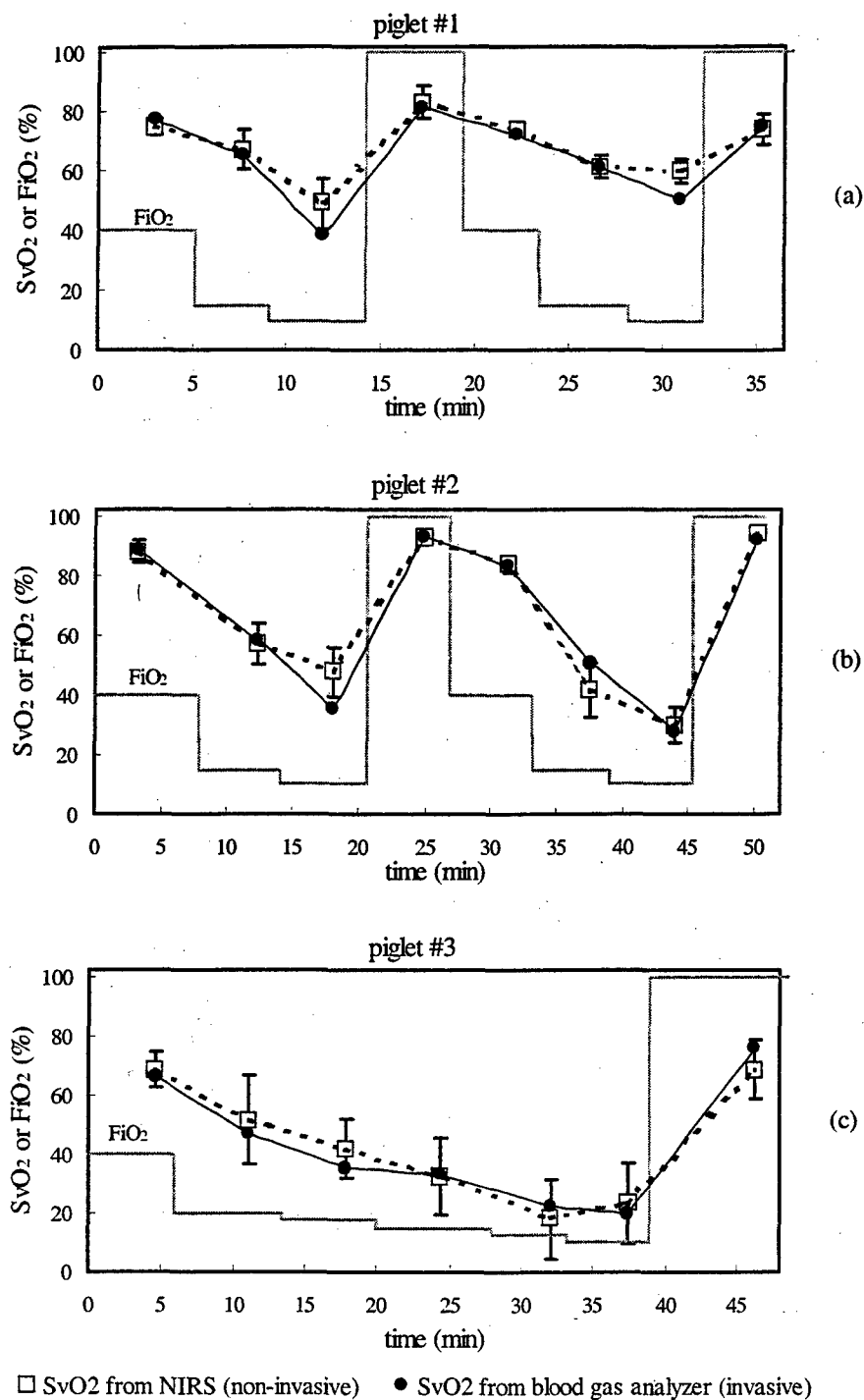
Figure 1 shows typical temporal traces (panel (a)) and amplitude spectra (panel (b)) of the relative oxy- and deoxy-hemoglobin concentrations measured on the piglet's leg. The temporal traces of  $[\text{Hb}]$  and  $[\text{HbO}_2]$  are obtained by fitting the measured absorption spectrum at each time with a linear combination of the oxy- and deoxy-hemoglobin extinction spectra. Figure 1(b) shows the values of the venous saturation measured from the fundamental (0.63 Hz;  $\text{SvO}_2 = 78\%$ ) and from the second harmonic (1.26 Hz;  $\text{SvO}_2 = 75\%$ ) of the breathing period. Figure 1(b) also shows the  $[\text{HbO}_2]$  and  $[\text{Hb}]$  peaks at the heartbeat frequency (2.54 Hz) from which we have been able to measure the arterial saturation ( $\text{SaO}_2 = 99\%$ ). By comparison, the invasive measurement of venous and arterial saturation with the blood gas analyzer gave values of 77.5% and 99%, respectively. The oscillatory components of the  $[\text{Hb}]$  and  $[\text{HbO}_2]$  traces at the breathing and heartbeat frequencies are readily identifiable in Fig. 1(a), which also shows the breathing wave recorded by the strain gauge placed around the piglet's chest. In a number of cases, we found more reliable results for  $\text{SvO}_2$  by analyzing the absorption peaks at the second harmonic rather than at the fundamental of the breathing rate. In Fig. 1 we show the time traces and the amplitude spectra of the oxy- and deoxy-hemoglobin concentrations because they are easier to visualize than the eight absorption traces and spectra. We note that computing the venous saturation from the oxy- and deoxy-hemoglobin traces is equivalent to using the eight absorption traces, provided that the absorption oscillations at the eight wavelengths are in phase. This follows from the fact that both the Fourier transform and the fitting procedure to translate the absorption changes into hemoglobin concentration changes are linear operations.

Figure 2 shows the comparison between the venous saturation values measured non-invasively with near-infrared spectroscopy (open squares) and invasively with a gas analysis of a venous blood sample (filled circles). In Fig. 2, we report the results for the first two  $\text{FiO}_2$  cycles in piglet #1 (panel (a)) and piglet #2 (panel (b)), and for the last  $\text{FiO}_2$  cycle in piglet #3. Figure 2 also shows the temporal evolution of  $\text{FiO}_2$  during the measurement.

Figure 3 summarizes our results on the three piglets examined. The shape of the symbols indicate the piglet (circles: piglet #1; squares: piglet #2; triangles: piglet #3), while the filling indicates the side of the near-infrared measurement (filled: right leg; open: left leg).



**Fig. 1.** (a) Temporal traces and (b) amplitude spectra of the oxy- and deoxy-hemoglobin concentrations ( $[\text{HbO}_2]$  and  $[\text{Hb}]$ , respectively) measured in piglet #1 while  $\text{FiO}_2$  was set to 40%. Panel (a) also shows the signal recorded by the strain gauge belt to monitor the breathing wave. The venous saturation ( $\text{SvO}_2$ ) measured from the amplitudes of the Fourier transforms at the fundamental and second harmonic of the breathing frequency are shown in panel (b), which also shows the arterial saturation ( $\text{SaO}_2$ ) measured from the peak at the arterial pulsation frequency. For comparison, the values of  $\text{SvO}_2$  and  $\text{SaO}_2$  measured invasively by the blood gas analyzer were 77.5% and 99%, respectively.



**Fig. 2.** Comparison between the venous saturation values measured non-invasively with NIRS (squares) and invasively from blood samples (circles) on (a) piglet #1, (b) piglet #2, and (c) piglet #3. The temporal evolution of the  $FiO_2$  level during the measurement is also shown. The lines that connect the points are added to guide the eye. The error bars indicate standard deviation errors from the approximately 800 Fourier transforms averaged for each NIRS reading of  $SvO_2$ .



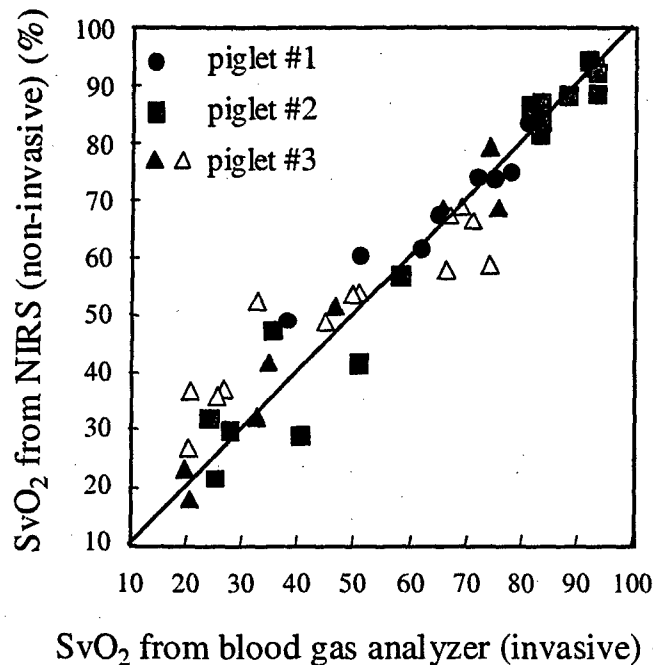


**Fig. 3.** Overall correlation between the venous saturation values measured non-invasively with NIRS (y-axis) and invasively by a blood gas analyzer (x-axis). The circles refer to piglet #1, the squares to piglet #2, and the triangles to piglet #3. The open triangles indicate two  $\text{FiO}_2$  cycles where the non-invasive optical data were acquired on the same leg (left) that was catheterized for the collection of blood samples for the invasive measurement of  $\text{SvO}_2$ .

#### 4. DISCUSSION

We found a good agreement between the venous saturation values measured non-invasively with near-infrared Fourier-oximetry and invasively by gas analysis of venous blood samples. This can be seen in the representative traces shown in Fig. 2 as well as in the overall summary shown in Fig. 3. All the results reported here are based on the analysis of the peaks at the second harmonic of the breathing frequency. While during normoxia and hyperoxia the results obtained by using the fundamental frequency are comparable to the results based on the second harmonic, in some hypoxic cases the calculations at the fundamental frequency yielded negative values of  $\text{SvO}_2$ . The invasive measurements were always performed on the left leg, while the non-invasive measurements were usually performed on the right leg. This raises a question as to whether it makes sense to compare measurements on different legs. We have found indications that under our experimental conditions this comparison is meaningful. In fact, several near-infrared measurements performed on the same leg used for the collection of blood samples (left) have reproduced the measurements on the right leg (see, for instance the open symbols in Fig. 3). Furthermore, we did not find significant differences by moving the probe to different locations of the same leg.

#### 5. CONCLUSION

We have reported our initial results of venous saturation measurements based on the analysis of the near-infrared oscillations with breathing. The non-invasive assessment of venous saturation by near-infrared tissue spectroscopy complements previously demonstrated optical measurements of tissue<sup>13-16</sup> and arterial<sup>12,17</sup> saturation. Therefore, these preliminary results may lead to the design of a single instrument capable of providing simultaneous non-invasive readings of local arterial, tissue, and venous saturation.

## ACKNOWLEDGMENTS

MAF acknowledges financial support from the US National Institutes of Health (NIH) Grant R01-MH62854. DAB acknowledges financial support from NIH R29-NS38842 and from the Center for Innovative Minimally Invasive Therapies. This research was funded in part by the US Army, under Cooperative Agreement No. DAMD17-99-2-9001. This publication does not necessarily reflect the position or the policy of the Government, and no official endorsement should be inferred.

## REFERENCES

1. T. Aoyagi, M. Kishi, K. Yamaguchi, and S. Watanabe, "Improvement of the Earpiece Oximeter," In: *Abstracts of the Japanese Society of Medical Electronics and Biological Engineering*, Tokyo, Japan, 90-91 (1974).
2. Y. Mendelson, "Pulse Oximetry: Theory and Applications for Noninvasive Monitoring," *Clin. Chem.* **38**, 1601-1607 (1992).
3. C. E. Elwell, H. Owen-Reece, M. Cope, A. D. Edwards, J. S. Wyatt, E. O. R. Reynolds, D. T. Delpy, "Measurement of changes in cerebral hemodynamic during inspiration and expiration using near infrared spectroscopy," *Adv. Exp. Med. Biol.* **388**, 619-626 (1994).
4. Y. Hoshi, M. Tamura, "Fluctuations in the cerebral oxygenation state during the resting period in functional mapping studies of the human brain," *Med. Biol. Eng. Comput.* **35**, 328-330 (1997).
5. C. Nolte, M. Kohl, U. Scholz, M. Weih, A. Villringer, "Characterization of the pulse signal over the human head by near infrared spectroscopy," *Adv. Exp. Med. Biol.* **454**, 115-123 (1998).
6. V. Toronov, M. A. Franceschini, M. Filiaci, M. Wolf, S. Fantini, and E. Gratton, "Near-Infrared Study of Fluctuations in Cerebral Hemodynamics During Rest and Motor Stimulation: Spatial Mapping and Temporal Analysis," *Med. Phys.* **27**, 801-815 (2000).
7. M. Wolf, G. Duc, M. Keel, P. Niederer, "Continuous noninvasive measurement of cerebral arterial and venous oxygen saturation at the bedside in mechanically ventilated neonates," *Crit. Care Med.* **9**, 1579-1582 (1997).
8. S. Fantini, M. A. Franceschini, J. S. Maier, S. A. Walker, B. Barbieri, and E. Gratton, "Frequency-Domain Multichannel Optical Detector for non-Invasive Tissue Spectroscopy and Oximetry," *Opt. Eng.* **34**, 32-42 (1995).
9. M. A. Franceschini, D. Wallace, B. Barbieri, S. Fantini, W. W. Mantulin, S. Pratesi, G. P. Donzelli, and E. Gratton, "Optical Study of the Skeletal Muscle During Exercise with a Second Generation Frequency-Domain Tissue Oximeter," in *Optical Tomography and Spectroscopy of Tissue: Theory, Instrumentation, Model, and Human Studies II*, B. Chance and R. R. Alfano, Editors, *Proc. SPIE* **2979**, 807-814 (1997).
10. D. T. Delpy, M. Cope, P. van der Zee, S. Arridge, S. Wray, and J. Wyatt, "Estimation of Optical Pathlength through Tissue from Direct Time of Flight Measurement," *Phys. Med. Biol.* **33**, 1433-1442 (1988).
11. S. Fantini, M. A. Franceschini, J. B. Fishkin, B. Barbieri, and E. Gratton, "Quantitative Determination of the Absorption Spectra of Chromophores in Strongly Scattering Media: a Light-Emitting-Diode Based Technique," *Appl. Opt.* **33**, 5204-5213 (1994).
12. M. A. Franceschini, E. Gratton, and S. Fantini, "Non-Invasive Optical Method to Measure Tissue and Arterial Saturation: an Application to Absolute Pulse Oximetry of the Brain," *Opt. Lett.* **24**, 829-831 (1999).
13. E. Gratton, S. Fantini, M. A. Franceschini, G. Gratton, and M. Fabiani, "Measurements of Scattering and Absorption Changes in Muscle and Brain," *Phil. Trans. R. Soc. of Lond. B* **352**, 727-735 (1997).
14. B. J. Tromberg, O. Coquoz, J. B. Fishkin, T. Pham, E. R. Anderson, J. Butler, M. Cahn, J. D. Gross, V. Venugopalan, and D. Pham, "Non-Invasive Measurements of Breast Tissue Optical Properties Using Frequency-Domain Photon Migration," *Phil. Trans. R. Soc. Lond. B* **352**, 661-668 (1997).
15. B. Chance, M. Cope, E. Gratton, N. Ramanujam, and B. Tromberg, "Phase measurement of light absorption and scatter in human tissues," *Rev. Sci. Instru.* **69**, 3457-3481 (1998).
16. M. C. van der Sluijs, W. N. Colier, R. J. Houston, B. Oeseburg, "New and highly sensitive continuous-wave near-infrared spectrophotometer with multiple detectors" in *Photon Propagation in Tissues III*, David A. Benaron; Britton Chance; Marco Ferrari; Eds., *Proc. SPIE* Vol. **3194**, 63-72 (1997).
17. A. Zourabian, A. Siegel, B. Chance, N. Ramanujam, M. Rode, D. A. Boas, "Trans-abdominal monitoring of fetal arterial blood oxygenation using pulse oximetry," *Journal of Biomedical Optics* **5**, 391-405 (2000).

# innovative techniques

## AQ: 1 Near-infrared spirometry: noninvasive measurements of venous saturation in piglets and human subjects

MARIA ANGELA FRANCESCHINI,<sup>1,2</sup> DAVID A. BOAS,<sup>2</sup> ANNA ZOURABIAN,<sup>2</sup> SOLOMON G. DIAMOND,<sup>2</sup> SHALINI NADGIR,<sup>1</sup> DAVID W. LIN,<sup>1</sup> JOHN B. MOORE,<sup>2</sup> AND SERGIO FANTINI<sup>1</sup>

<sup>1</sup>Bioengineering Center, Department of Electrical Engineering and Computer Science Tufts University, Medford 02155-6013; and <sup>2</sup>NMR Center, Massachusetts General Hospital, Harvard Medical School, Charlestown, Massachusetts 02129

Received 24 May 2001; accepted in final form 20 August 2001

Franceschini, Maria Angela, David A. Boas, Anna Zourabian, Solomon G. Diamond, Shalini Nadgir, David W. Lin, John B. Moore, and Sergio Fantini. Near-infrared spirometry: noninvasive measurements of venous saturation in piglets and human subjects. *J Appl Physiol* 91: 000-000, 2001.—We present a noninvasive method to measure the venous oxygen saturation ( $SvO_2$ ) in tissues using near-infrared spectroscopy (NIRS). This method is based on the respiration-induced oscillations of the near-infrared absorption in tissues, and we call it spirometry (the prefix spiro means respiration). We have tested this method in three piglets (hind leg) and in eight human subjects (vastus medialis and vastus lateralis muscles). In the piglet study, we compared our NIRS measurements of the  $SvO_2$  ( $SvO_2$ -NIRS<sub>resp</sub>) with the  $SvO_2$  of blood samples.  $SvO_2$ -NIRS<sub>resp</sub> and  $SvO_2$  of blood samples agreed well over the whole range of  $SvO_2$  considered (20–95%). The two measurements showed an average difference of 1.0% and a standard deviation of the difference of 5.8%. In the human study, we found a good agreement between  $SvO_2$ -NIRS<sub>resp</sub> and the  $SvO_2$  values measured with the NIRS venous occlusion method. Finally, in a preliminary test involving muscle exercise,  $SvO_2$ -NIRS<sub>resp</sub> showed an expected postexercise decrease from the initial baseline value and a subsequent recovery to baseline.

tissue spectroscopy; frequency-domain; pulse oximetry; hemoglobin saturation

calculated from published values of the molar extinction coefficients of oxyhemoglobin ( $HbO_2$ ) and deoxyhemoglobin ( $Hb$ ) (43, 53).

Oxygen saturation of the pulmonary capillary blood in rabbits has been measured by using dynamic invasive techniques (48). Near-infrared light in the wavelength range from 700 to 900 nm results in a sufficient penetration depth for the noninvasive optical monitoring of skeletal muscle, cerebral gray matter, and breast tissue. As a result, near-infrared techniques allow a noninvasive assessment of hemoglobin saturation for a wide range of applications, such as the study of muscle metabolism (7, 9, 12, 29, 45), the diagnosis of vascular disorders (2, 20, 32, 33, 44, 49), functional brain imaging (3, 10, 24, 30, 35, 50), and breast cancer detection (23, 28, 40, 42, 46).

If near-infrared light is highly sensitive to the oxygen saturation of hemoglobin, then its large penetration depth inside tissues implies that the arterial, venous, and capillary compartments all contribute to the optical signal. The average hemoglobin oxygenation measured with near-infrared spectroscopy (NIRS) (19, 34, 41) is usually referred to as tissue oxygen saturation ( $StO_2$ ).  $StO_2$  values are assumed to be in between arterial and local venous saturation values ( $SaO_2$  and  $SvO_2$ , respectively). A number of research studies have investigated the relationship between the near-infrared (noninvasive) measurement of  $StO_2$  and the values of  $SaO_2$  and local  $SvO_2$  measured invasively from drawn blood samples (31, 51). The contribution of the arterial compartment to the noninvasive optical signal can be isolated because of its unique temporal dynamics associated with the systolic-diastolic blood pressure variation at the heartbeat frequency (1). The

THE POSSIBILITY OF USING LIGHT to measure the oxygen saturation of hemoglobin in vivo has been explored since the 1940s (37). The feasibility of optical blood oximetry stems from the oxygenation dependence of the optical spectrum of hemoglobin. This is illustrated in Fig. 1, which shows the absorption spectra of 100  $\mu M$  hemoglobin for oxygen saturation values of 0, 20, 40, 60, 80, and 100%. The spectra of Fig. 1 were

Address for reprint requests and other correspondence: M. A. Franceschini, Bioengineering Center, Dept. of Electrical Engineering and Computer Science, Tufts Univ., 4 Colby St., Medford, MA 02155-6013 (E-mail: mari@eecs.tufts.edu).

The costs of publication of this article were defrayed in part by the payment of page charges. The article must therefore be hereby marked "advertisement" in accordance with 18 U.S.C. Section 1734 solely to indicate this fact.

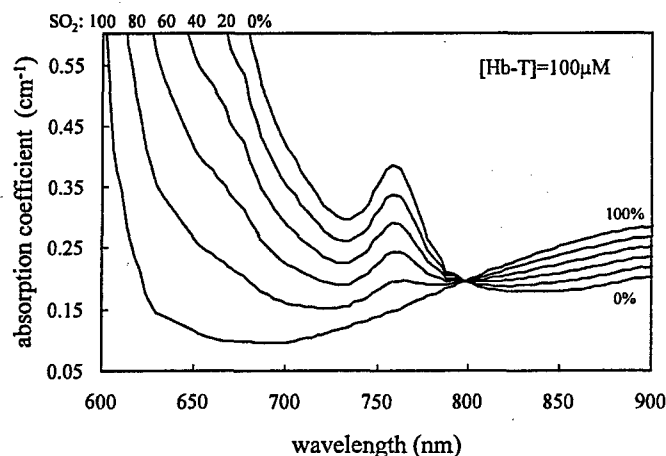


Fig. 1. Near-infrared absorption spectra of 100  $\mu\text{M}$  hemoglobin concentration ( $[\text{Hb-T}]$ , where T stands for total) for different values of the oxygen saturation ( $\text{SO}_2$ ) in the range of 0–100%. The curve for  $\text{SO}_2 = 0\%$  corresponds to the deoxyhemoglobin (Hb) absorption spectrum, whereas the curve for  $\text{SO}_2 = 100\%$  corresponds to the oxyhemoglobin ( $\text{HbO}_2$ ) absorption spectrum. These spectra have been computed from published spectra of the molar extinction coefficients of  $\text{HbO}_2$  and Hb (43, 53).

pulsatile component of the optical signals at two or more wavelengths at the heartbeat frequency is used by conventional (1, 36) or self-calibrated (21) pulse oximeters to measure the  $\text{SaO}_2$ .  $\text{SaO}_2$  is a parameter that provides information about the ventilation and the oxygen exchange in the lungs. In contrast,  $\text{SvO}_2$  is a parameter that reflects the local balance between blood flow and oxygen consumption. The noninvasive optical measurement of  $\text{SvO}_2$  is complicated by the fact that the isolation of the contribution of the venous compartment to the noninvasive optical signal is not straightforward. There are no clinical devices presently capable of monitoring  $\text{SvO}_2$  noninvasively.

A number of experimental approaches have been proposed to measure  $\text{SvO}_2$  from induced local changes in the venous blood volume. For instance, proposed approaches involve a venous occlusion in a limb (13, 39, 55, 56), tilting the patient's head down by 15 degrees (47), a partial jugular vein occlusion (15, 54), or mechanical ventilation (52). In all these approaches,  $\text{SvO}_2$  is optically measured as the ratio between the increases in the  $\text{HbO}_2$  concentration ( $[\text{HbO}_2]$ ) and the total hemoglobin concentration (equal to  $[\text{HbO}_2] + [\text{Hb}]$ , where  $[\text{Hb}]$  is deoxyhemoglobin concentration) induced by the local increase in venous blood volume. To overcome the limitations of these methods, which can either be applied only to the limbs (venous occlusion method) or require an external perturbation (partial jugular vein occlusion, mechanical ventilation, and tilting methods), we propose an alternative approach that is an extension of the method of Wolf et al. (52). This approach involves no external perturbations and is applicable to subjects who are breathing either spontaneously or synchronously with a metronome set at their average respiratory frequency. Furthermore, this method can provide continuous and real-time monitoring of  $\text{SvO}_2$ . The basic idea is to measure  $\text{SvO}_2$  from the

amplitude of the optically measured  $[\text{HbO}_2]$  and  $[\text{Hb}]$  oscillations at the respiratory frequency. The basic hypothesis, originally formulated in this context and tested on the brain of mechanically ventilated infants by Wolf et al., is that the oscillatory components of  $[\text{HbO}_2]$  and  $[\text{Hb}]$  at the breathing rate are mostly representative of the venous compartment. Because the venous compliance is  $\sim 20$  times as large as the arterial compliance (4), a given change in the blood pressure in the veins causes a venous volume change  $\sim 20$  times as large as the arterial volume change corresponding to the same pressure change in the arteries. During normal breathing, the inspiration phase involves a decrease in the intrathoracic pressure and an increased pressure gradient between the peripheral venous system and the intrathoracic veins. This causes blood to be drawn from the extrathoracic veins into the intrathoracic vessels and heart (26). Because of the vein valves, venous return is increased more by inspiration than it is decreased by expiration (38). The net effect is the so-called respiratory pump that facilitates the venous return from the periphery by the respiration-induced periodic fluctuations in the central venous pressure (38). As a result of the respiratory pump, the peripheral venous blood volume oscillates at the respiratory frequency, decreasing during inspiration and increasing during expiration.

It is on this oscillatory component at the respiratory frequency that we base our near-infrared measurement of the  $\text{SvO}_2$ . We coin the term *spiroximeter* to indicate an instrument for measuring the  $\text{SvO}_2$  from respiration-induced oscillations in the venous blood pressure and in the venous volume fraction in tissues. It must be observed that respiration may also induce perturbations to the heart rate (respiratory sinus arrhythmia) and consequently to the cardiac output and arterial blood pressure. As a result, the arterial compartment volume may, in general, also oscillate at the respiratory frequency; thus near-infrared spiroximetry data must be carefully examined to guarantee a reliable reading of  $\text{SvO}_2$ .

We report a validation study conducted on the hind leg of three piglets, in which we compared the near-infrared measurements of  $\text{SvO}_2$  ( $\text{SvO}_2\text{-NIRS}$ ) with the  $\text{SvO}_2$  values obtained by the gas analysis of venous blood samples ( $\text{SvO}_2\text{-blood}$ ). To show the applicability of spiroximetry to human subjects, we also conducted a preliminary test on the vastus medialis and vastus lateralis muscles of healthy volunteers at rest and postexercise.

## MATERIALS AND METHODS

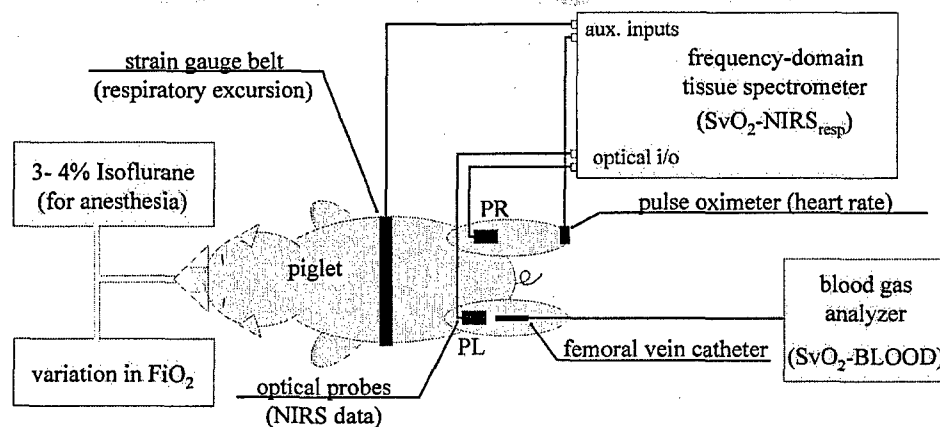
**Tissue spectrometer.** The near-infrared measurements were performed with a frequency-domain tissue spectrometer (model 96208, ISS, Champaign, IL) (18, 25). This instrument uses two parallel photomultiplier tube detectors that are time shared by eight multiplexed laser diodes emitting at 636, 675, 691, 752, 780, 788, 830, and 840 nm, respectively. The frequency of intensity modulation is 110 MHz, and heterodyne detection is performed with a cross-correlation frequency of 5 kHz. The multiplexing rate, i.e., the frequency

of sequential laser switching, is 100 Hz. As a result, 50 cross-correlation periods are acquired during the on time of each laser diode, and a complete acquisition cycle over the eight wavelengths is completed every 80 ms. The laser diodes and the photomultiplier tubes are all coupled to fiber optics. The eight individual illumination fibers, each 400  $\mu\text{m}$  in internal diameter, are arranged into a fiber bundle having a rectangular cross-section of  $3.5 \times 2.0 \text{ mm}^2$ . The collecting circular fiber bundles are 3.0 mm in internal diameter. The optical fibers are placed in contact with the skin by means of a flexible plastic probe. The optical probe arranges the tips of the illuminating and collecting fiber bundles along a line, with the two collecting fiber bundles at distances of 1.0 and 2.0 cm from the single illuminating bundle. In some cases, we have used a second tissue spectrometer to perform simultaneous measurements on both legs (piglets 2 and 3) or at different locations on the same leg (human subjects). In the second tissue spectrometer (which used the optical probes PL and HVL defined below), the 840-nm laser diode was replaced by a laser diode emitting at 814 nm.

**Measurements on piglets.** We performed measurements on three piglets that were  $15 \pm 1$  days old and weighed  $5 \pm 1 \text{ kg}$ . The experimental arrangement for the piglet measurements is schematically illustrated in Fig. 2. The piglets were anesthetized by inhalation of 3–4% isoflurane administered by means of a breathing mask applied to the piglet's snout. The animals were not mechanically ventilated, and they breathed freely throughout the experiment. A strain-gauge belt (Sleepmate/Newlife Technologies, Resp-EZ) was placed around the piglet's thorax to continuously monitor the respiratory excursion. A pulse oximeter (Nellcor, N-200) continuously recorded the heart rate at the foot of the right hind leg. The analog outputs from the strain gauge and the pulse oximeter were fed to the auxiliary input ports of the tissue spectrometer for continuous coregistration of optical and physiological data. A femoral cutdown was performed into the left inferior femoral vein to insert a catheter for periodic blood sampling. The femoral venous blood samples were run through a commercial blood-gas analyzer (Instrumentation Laboratory, model

1304 pH/blood-gas analyzer) to obtain invasive readings of  $\text{SvO}_2$ -blood. One optical probe (identified as *probe PR*) was always located on the right (noncatheterized) hind leg. In piglets 2 and 3, a second probe (*probe PL*) was placed on the catheterized (left) leg. The protocol consisted of varying the femoral  $\text{SvO}_2$  over the approximate range of 20–95% by modulating the volume fraction of oxygen inspired by the piglet ( $\text{FI}_{\text{O}_2}$ ) over the range of 10–100%. The oxygenation cycles performed on the three piglets are illustrated in Fig. 3. Each cycle consisted of varying the  $\text{FI}_{\text{O}_2}$  approximately every 4–6 min through the values of ~40, 75, 10, and 100% (piglets 1 and 2) or ~40, 20, 17.5, 15, 12.5, 10, and 100% (piglet 3). We performed two ( $\text{FI}_{\text{O}_2}$ ) cycles on piglet 1, four on piglet 2, and three on piglet 3. For each specific value of  $\text{FI}_{\text{O}_2}$ , we acquired about 3,000 optical data points [ $4 \text{ min} \times (60 \text{ s/min}) / (80 \text{ ms/data point})$ ] or more. During cycles C and D on piglet 2, the optical probe PR was slightly moved with respect to the location examined during cycles A and B, to collect data on two different muscle volumes during the two cycle pairs A-B and C-D. Optical probe PR always collected data on the right hind leg, whereas probe PL was placed on the left hind leg during cycles A and B of piglet 2 and cycles A and B of piglet 3 (we did not collect data with the optical probe PL on piglet 1, during cycles C-D on piglet 2, and during cycle C on piglet 3). In all three piglets, the invasive measurement of  $\text{SvO}_2$  from a femoral vein blood sample was performed at the end of each  $\text{FI}_{\text{O}_2}$  interval, as shown in Fig. 3. Motion artifacts were minimized in the optical data by securing the piglet's legs to the operating table. The protocol was approved by the Institutional Review Board of the Massachusetts General Hospital, where the piglet experiments were performed.

**Measurements on human subjects.** We performed measurements on eight healthy human subjects (6 men and 2 women; mean age of 24.5 yr, age range of 20–35 yr). The subjects sat on a comfortable chair and rested for 10–15 min before the experimental protocol was started. A pneumatic cuff was placed around the right thigh of the subject to later induce a venous occlusion by inflating the cuff to a pressure of 70 mmHg. A pulse oximeter probe (Nellcor, N-200) was placed



**AQ: 11** Fig. 2. Experimental arrangement for the piglet study. A breathing mask applied to the piglet's snout provided the 3–4% isoflurane anesthetic and was connected to the oxygen line for variations in the fraction of inspired oxygen ( $\text{FI}_{\text{O}_2}$ ). A strain-gauge belt and a pulse oximeter monitored the respiratory excursion and the heart rate, respectively, and their analog outputs were directed to the auxiliary inputs of the frequency-domain tissue spectrometer (ISS, Champaign, IL, model 96208). One or two optical probes (PR on the right hind leg and PL on the left hind leg) of the tissue spectrometer were used to measure the near-infrared tissue absorption with a time resolution of 80 ms. The absorption oscillations at the respiratory frequency were processed to provide measurement of the venous  $\text{O}_2$  saturation ( $\text{SvO}_2$ -NIRS<sub>resp</sub>) (NIRS is near-infrared spectroscopy). Invasive measurements of the venous  $\text{O}_2$  saturation (designated  $\text{SvO}_2$ -blood) were obtained by gas analysis of venous blood samples collected by a femoral vein catheter. aux, Auxiliary. **AQ: 8** optical i/o, optical input/output

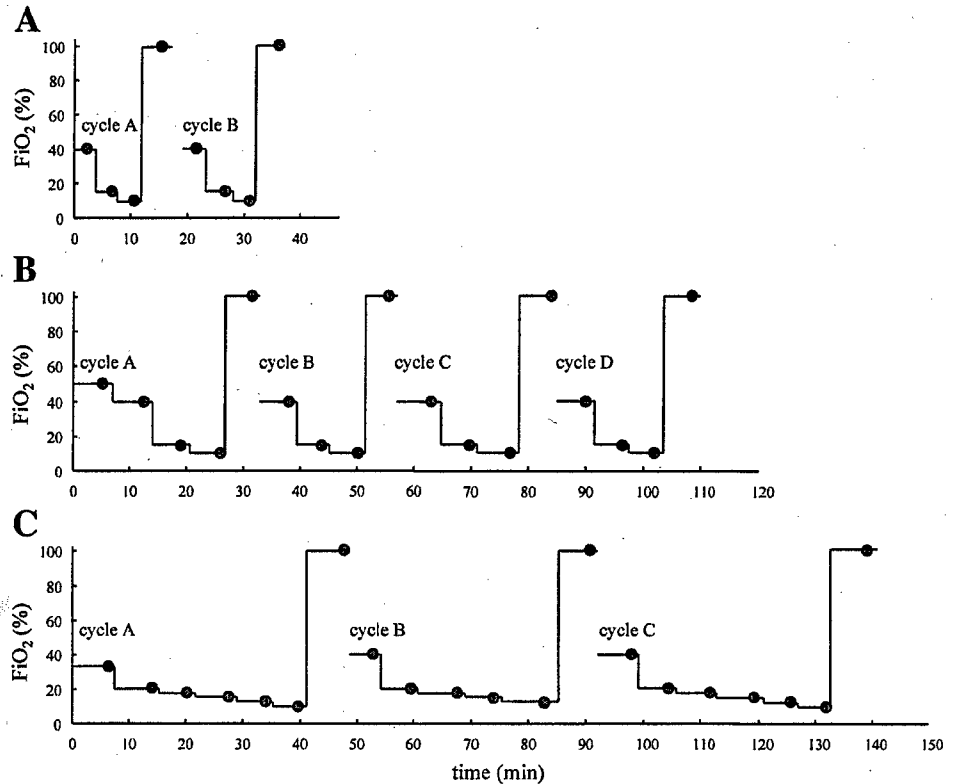


Fig. 3. Schematic representation of  $\text{FiO}_2$  cycles for piglet 1 (A), piglet 2 (B), and piglet 3 (C). •, Time at which venous blood samples were run through the blood-gas analyzer for  $\text{SvO}_2$ -blood measurements.

no 1751ic

on the index finger of the left hand. A strain-gauge belt (Sleepmate/Newlife Technologies, Resp-EZ) was placed around the subject's upper abdomen to monitor the respiratory excursion. As in the piglet experiment, we used the analog outputs of the pulse oximeter and strain gauge for continuous coregistration of the physiological and near-infrared data. Two optical probes were placed on the right thigh; the first probe (probe HVM) was positioned on top of a visible superficial vein of the vastus medialis muscle, and the second probe (probe HVL) was placed on the vastus lateralis muscle, far from visible superficial veins. During the measurements, we asked the subject to breathe regularly, following a metronome whose frequency was set to the average breathing rate of the subject at rest (typically 14–15 breaths/min). During the whole experiment, the subject was asked to breathe at the same frequency as the metronome pace. No subjects experienced any discomfort or difficulties with this procedure. The measurement protocol consisted of 2 min of baseline (we acquired 1,535 optical data points at 80 ms/point), followed by 40 s of venous occlusion, and a final recovery period of a few minutes. A few subjects performed an additional exercise routine to test the effect of exercise on the measured value of  $\text{SvO}_2$ -NIRS<sub>resp</sub> on the muscle. The exercise consisted of raising the right foot, voluntarily contracting the leg muscles (isometric contraction), until the subject felt tired. The human study was approved by the Institutional Review Board of Tufts University, where the human experiments were performed; all subjects gave their written, informed consent.

*Near-infrared data processing for the measurement of  $\text{SvO}_2$ .* We used a modified Beer-Lambert law approach (14) to translate the temporal intensity ratio collected at each wavelength  $[I(\lambda, t)/I(\lambda, t_0)]$ , where  $I$  is intensity,  $\lambda$  is wavelength, and  $t$  is time] at a distance of 1.0 cm from the illumination point, into a time variation in the tissue absorption  $[\Delta\mu_a(\lambda, t)]$ ,

where  $\mu_a$  is the tissue absorption coefficient]. This approach was implemented by applying the following equation (14)

$$\Delta\mu_a(\lambda, t) = \frac{1}{L_{\text{eff}}} \ln \left[ \frac{I(\lambda, 0)}{I(\lambda, t)} \right] \quad (1)$$

where  $L_{\text{eff}}$  is the effective optical pathlength from the illuminating point to the light collection point. We measured  $L_{\text{eff}}$  by quantifying  $\mu_a$  and the reduced scattering coefficient ( $\mu'_s$ ) using the frequency-domain multidistance method (17). The diffusion-theory relationship that gives  $L_{\text{eff}}$  in terms of  $\mu_a$ ,  $\mu'_s$ , and the source-detector separation ( $r$ ) in a semi-infinite turbid medium (where the illumination and collection points are at the boundary of the turbid medium) is the following (17)

$$L_{\text{eff}} = \frac{3\mu'_s r^2}{2(r\sqrt{3\mu_a\mu'_s + 1})} \quad (2)$$

More details on this hybrid frequency-domain [to measure  $L_{\text{eff}}(\lambda)$ ] and continuous wave (modified Beer-Lambert law) approach are given in Refs. 14, 17, 21, and 22. Equation 2 shows that for typical values of the near-infrared  $\mu_a$  and  $\mu'_s$ , say  $\mu_a = 0.1 \text{ cm}^{-1}$  and  $\mu'_s = 10 \text{ cm}^{-1}$ , the value of  $L_{\text{eff}}$  is  $\sim 5.5 \text{ cm}$  for  $r = 1 \text{ cm}$ . The multi-distance scheme was implemented by considering the data collected by the two fiber bundles located at two different distances (1.0 and 2.0 cm) from the source fiber bundle. At these source detector distances, the diffusion regime of light propagation in tissues is already established (18). As an alternative to the diffusion equation model to describe the spatial dependence of the optical signal, empirical approaches have been proposed (6). The different sensitivity of the two detector channels was accounted for by a preliminary calibration measurement on a synthetic tissue-like sample. The applicability of the initial calibration to the

AQ: 3

and  $t_0$  is the time  
starting time

whole data set was verified at the end of each measurement session by repositioning the optical probe on the calibration sample. We typically reproduced the calibration values of the block optical coefficients to within 10%. In the piglet experiments, we updated the measured values of  $L_{\text{eff}}$  at each wavelength every time the  $\text{FiO}_2$  was changed. Specifically,  $L_{\text{eff}}$  was computed, according to Eq. 2, from average measurements of  $\mu_a$  and  $\mu_s'$  over the last 80 s of each period corresponding to a specific  $\text{FiO}_2$  value. For the measurements on human subjects, we computed an initial value of  $L_{\text{eff}}$  (at each wavelength) over the first 2 min of baseline, and we used this value for the analysis of the data over the whole measurement session. The long integration time for the mean pathlength measurements (80 s in the piglet experiment, 120 s in the human subjects measurements) realized a low-pass filter that minimized the time-varying contributions from the Hb oscillations caused by the arterial pulsation and breathing. Furthermore, the two-distance measurement scheme for the mean pathlength measurement also provided some level of spatial averaging. In contrast, the optical data for the measurement of  $\text{SvO}_2$  were acquired with an 80-ms temporal resolution and with the use of a single source-detector distance (1 cm).

To measure the  $\text{SvO}_2$ , we followed a two-step procedure. First, we computed the amplitude of the absorption oscillations at the respiratory frequency at each of the eight wavelengths considered. Second, we fit the spectrum of the experimental absorption amplitude with the hemoglobin absorption spectrum. We have used two alternative methods to quantify the absorption oscillations at the respiratory frequency. The first method is based on the fast Fourier transform (FFT) of  $\Delta\mu_a(t)$ . The sum of the amplitudes of the FFT of  $\Delta\mu_a$  over the respiratory frequency band yields a measure of the amplitude of the respiration-induced absorption oscillations. This method assumes that the Fourier spectrum of  $\Delta\mu_a$  clearly shows a discernable peak at the respiratory frequency. The second method is based on a band-pass (BP) filter of  $\Delta\mu_a(t)$  and on a modeling algorithm (MA) (sine-wave fit). The BP filter serves the purpose of isolating the absorption oscillations at the respiratory frequency by suppressing higher and lower frequency components in  $\Delta\mu_a(t)$ . The MA consists of fitting a sine wave to  $\Delta\mu_a(\text{BP})$  over each respiratory cycle. The amplitude of the fitted sine wave gives an estimate of the absorption oscillation amplitude at the respiratory frequency. As a result, the second method (BP + MA) achieves a reading of  $\text{SvO}_2$  from each individual respiration cycle, whereas the first method (FFT) requires multiple respiration cycles to produce a  $\text{SvO}_2$  reading. Both methods provide phase readings that can be used to verify that the respiration-induced absorption oscillations at different wavelengths are in phase with each other. We indicate the  $\text{SvO}_2$  measurement according to the FFT and BP + MA methods with  $\text{SvO}_2\text{-NIRS}_{\text{resp}}(\text{FFT})$  and  $\text{SvO}_2\text{-NIRS}_{\text{resp}}(\text{BP})$ , respectively.

In the piglet experiments, we evaluated the FFT of  $\Delta\mu_a$  over 256 data points, corresponding to a time trace of 20.5 s, to achieve reliable spectra from a number of breathing periods (typically 13–16). Furthermore, we averaged about 800 successive FFTs (each computed from a data set shifted by one data point with respect to the previous one), so that the total number of data points resulting in a single  $\text{SvO}_2$  reading was on the order of 1,000, corresponding to a train of data 80 s long. This 80-s-long data set was chosen to be at the end of each  $\text{FiO}_2$  period, and it coincides with the 80-s period over which we measured  $L_{\text{eff}}$ . In the human subject experiment, we used 512 points for the FFT because the breathing frequency was lower (0.22–0.26 Hz) than that of the piglets

(0.6–0.9 Hz) and we wanted to have a similar number of breathing periods. As in the piglets experiment, we averaged the results from multiple (500–1,000) successive FFTs.

The spectrum of the amplitude of the absorption oscillations at the respiratory frequency  $[\Delta\mu_a^{\text{resp}}(\lambda_i)]$  was fitted with a linear combination of the HbO<sub>2</sub> and Hb extinction spectra,  $[\sum_i \Delta\mu_a^{\text{resp}}(\lambda_i) \Delta[\text{HbO}_2]^{\text{resp}} + \sum_i \text{Hb}(\lambda_i) \Delta[\text{Hb}]^{\text{resp}}]$  where  $\Delta[\text{HbO}_2]^{\text{resp}}$  and  $\Delta[\text{Hb}]^{\text{resp}}$  are the extinction coefficients of HbO<sub>2</sub> and Hb, respectively (43, 53). The fitting parameters were the amplitudes of the oscillatory  $[\text{HbO}_2]$  ( $\Delta[\text{HbO}_2]^{\text{resp}}$ ) and  $[\text{Hb}]$  ( $\Delta[\text{Hb}]^{\text{resp}}$ ) at the respiratory frequency. The minimization of the sum of the squares of the residuals, i.e.,  $\sum_i [\Delta\mu_a^{\text{resp}}(\lambda_i) - \Delta\mu_a^{\text{resp}}(\lambda_i)]^2$ , yields a linear system whose solution gives the following best fit concentrations of amplitude of the oscillatory  $[\text{HbO}_2]$  and  $[\text{Hb}]$  (11)

$$\Delta[\text{HbO}_2]^{\text{resp}} = \frac{[\sum_i \Delta\mu_a^{\text{resp}}(\lambda_i) \epsilon_{\text{HbO}_2}(\lambda_i)] [\sum_i \epsilon_{\text{Hb}}^2(\lambda_i)] - [\sum_i \Delta\mu_a^{\text{resp}}(\lambda_i) \epsilon_{\text{Hb}}(\lambda_i)] [\sum_i \epsilon_{\text{HbO}_2}(\lambda_i) \epsilon_{\text{Hb}}(\lambda_i)]}{[\sum_i \epsilon_{\text{HbO}_2}^2(\lambda_i)] [\sum_i \epsilon_{\text{Hb}}^2(\lambda_i)] - [\sum_i \epsilon_{\text{HbO}_2}(\lambda_i) \epsilon_{\text{Hb}}(\lambda_i)]^2} \quad (3) \text{ Conc or oxy}$$

$$\Delta[\text{Hb}]^{\text{resp}} = \frac{[\sum_i \Delta\mu_a^{\text{resp}}(\lambda_i) \epsilon_{\text{Hb}}(\lambda_i)] [\sum_i \epsilon_{\text{HbO}_2}^2(\lambda_i)] - [\sum_i \Delta\mu_a^{\text{resp}}(\lambda_i) \epsilon_{\text{HbO}_2}(\lambda_i)] [\sum_i \epsilon_{\text{HbO}_2}(\lambda_i) \epsilon_{\text{Hb}}(\lambda_i)]}{[\sum_i \epsilon_{\text{HbO}_2}^2(\lambda_i)] [\sum_i \epsilon_{\text{Hb}}^2(\lambda_i)] - [\sum_i \epsilon_{\text{HbO}_2}(\lambda_i) \epsilon_{\text{Hb}}(\lambda_i)]^2} \quad (4)$$

The oxygen saturation of the hemoglobin compartment oscillating synchronously with respiration ( $\text{SvO}_2\text{-NIRS}_{\text{resp}}$ ) is then given by

$$\text{SvO}_2\text{-NIRS}_{\text{resp}} = \frac{\Delta[\text{HbO}_2]^{\text{resp}}}{\Delta[\text{HbO}_2]^{\text{resp}} + \Delta[\text{Hb}]^{\text{resp}}} = \frac{[\sum_i \Delta\mu_a^{\text{resp}}(\lambda_i) \epsilon_{\text{HbO}_2}(\lambda_i)] [\sum_i \epsilon_{\text{Hb}}^2(\lambda_i)] - [\sum_i \Delta\mu_a^{\text{resp}}(\lambda_i) \epsilon_{\text{Hb}}(\lambda_i)] [\sum_i \epsilon_{\text{HbO}_2}(\lambda_i) \epsilon_{\text{Hb}}(\lambda_i)]}{[\sum_i \Delta\mu_a^{\text{resp}}(\lambda_i) \epsilon_{\text{HbO}_2}(\lambda_i)] [\sum_i \epsilon_{\text{Hb}}(\lambda_i) [\epsilon_{\text{Hb}}(\lambda_i) - \epsilon_{\text{HbO}_2}(\lambda_i)] - [\sum_i \Delta\mu_a^{\text{resp}}(\lambda_i) \epsilon_{\text{Hb}}(\lambda_i)] [\sum_i \epsilon_{\text{HbO}_2}(\lambda_i) [\epsilon_{\text{Hb}}(\lambda_i) - \epsilon_{\text{HbO}_2}(\lambda_i)]} \quad (5)$$

It is important to note that for the determination of  $\text{SvO}_2\text{-NIRS}_{\text{resp}}$  one only needs to know  $L_{\text{eff}}$  to within a wavelength-independent factor. In fact, Eq. 5 shows that a common, wavelength-independent multiplicative factor in  $\Delta\mu_a(\lambda_i)$  cancels out in the expression for  $\text{SvO}_2\text{-NIRS}_{\text{resp}}$ . In contrast, the wavelength dependence of  $L_{\text{eff}}$  is important for the measurement of  $\text{SvO}_2$  with our method, and this is why we have opted to measure  $L_{\text{eff}}$  at each wavelength using the multidistance, frequency-domain technique. It is also important to observe that our method requires that 1) oscillations of  $\mu_a$  at the respiratory frequency to be reliably attributed to hemoglobin (and not, for instance, to motion artifacts), 2) the hemoglobin concentration fluctuations to result from the volume oscillation of a hemoglobin compartment rather than from periodic fluctuations in the blood flow, and 3) the fluctuating hemoglobin compartment responsible for the measured  $\Delta\mu_a$  to be mainly the venous compartment. In our measurements, we have considered each one of the three above points. The assignment of the absorption oscillations to hemoglobin (point 1) was done by requiring that the hemoglobin spectrum fits the absorption data relatively well. To this aim, we requested that the average absolute value of the relative residuals, defined as  $\overline{\text{res}}^{\text{fit}} = 1/N \sum_{i=1}^N |\Delta\mu_a^{\text{fit}}(\lambda_i) - \Delta\mu_a^{\text{resp}}(\lambda_i)| / \Delta\mu_a^{\text{fit}}(\lambda_i)$ , where  $N$  is the number of wavelengths considered, be at most twice the experimental percent error in  $\Delta\mu_a^{\text{resp}}$ . We also used the standard deviation of the  $\text{SvO}_2\text{-NIRS}_{\text{resp}}(\text{FFT})$  values obtained with the 800 (piglet experiment) or 500–1,000 (human experiment) successive FFTs to estimate the



error in  $SvO_2$ -NIRS<sub>resp</sub>(FFT). We discarded the cases having a standard deviation error in  $SvO_2$ -NIRS<sub>resp</sub> greater than 15%. The assignment of the absorption oscillations to volume rather than blood flow fluctuations (*point 2*) is achieved by verifying that the absorption oscillations at the eight wavelengths are in phase. In fact, blood flow fluctuations induce out-of-phase oscillations in the [HbO<sub>2</sub>] and [Hb] (because of the increased rates of inflow of HbO<sub>2</sub> and washout of Hb), as opposed to the in-phase oscillations of HbO<sub>2</sub> and Hb that result from volume pulsations. The third point, namely the requirement that the absorption oscillations at the respiratory frequency are representative of venous blood, is investigated by 1) comparing the  $SvO_2$ -NIRS from the respiratory hemoglobin oscillations ( $SvO_2$ -NIRS<sub>resp</sub>) with the corresponding values measured by gas analysis of  $SvO_2$ -blood (piglet experiments) or by the NIRS venous occlusion method ( $SvO_2$ -NIRS<sub>vo</sub>) (human subject experiments), 2) studying the effect on the [Hb] and [HbO<sub>2</sub>] oscillations at the respiratory frequency of a venous occlusion induced between the lungs and the peripheral measurement area (the thigh muscles in human subject experiments), and 3) by recording the effect of muscle exercise on the near-infrared measurements of  $SvO_2$  [ $SvO_2$ -NIRS<sub>resp</sub>(BP)] in human subjects.

## RESULTS

**F4** Figure 4 reports average spectra of  $L_{eff}$  measured for a source-detector separation of 1 cm. Figure 4A refers to piglet measurements conducted at two different values of  $FiO_2$ , whereas Fig. 4B refers to human measurements with probes HVM and HVL. The error bars in

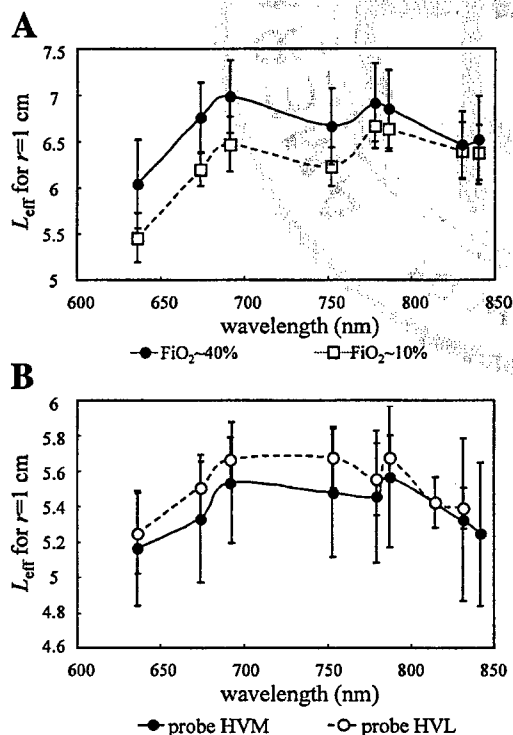


Fig. 4. Near-infrared spectra of the effective optical pathlength ( $L_{eff}$ ) measured on the piglet's leg (A) and a human thigh muscle (B) for a source-detector separation ( $r$ ) of 1 cm. In A, different symbols refer to 2 different values of  $FiO_2$ . In B, different symbols refer to 2 different thigh muscles (vastus medialis for probe HVM and vastus lateralis for probe HVL). The lines join the points as an aid to the eye.

Fig. 4 represent the standard deviations over multiple measurements (multiple  $FiO_2$  cycles and piglets for Fig. 4A and multiple subjects for Fig. 4B).

In the piglet experiment, we discarded 11 (from a total of 67)  $SvO_2$ -NIRS<sub>resp</sub>(FFT) measurements because the standard deviation over 800 FFTs exceeded 15%. These discarded  $SvO_2$ -NIRS<sub>resp</sub>(FFT) readings occurred as follows: one (of 8) in *piglet 1*, two (of 26) in *piglet 2*, and eight (of 33) in *piglet 3*. One discarded reading was assigned to motion artifacts, whereas the other ten discarded measurements all occurred at low- $FiO_2$  values (10–17.5%) corresponding to  $SvO_2$ -blood values of 20–50%. We were not able to apply the BP method to *piglet 2* and to the  $FiO_2$  cycles A and B of *piglet 3* because of irregular absorption oscillation waveforms that were not reliably processed by the BP + MA approach.

Figure 5 shows typical temporal traces of the relative [HbO<sub>2</sub>] and [Hb] measured on the piglet's leg (with optical probe PR) (Fig. 5A) and on the human vastus medialis muscle at rest (Fig. 5B) and during venous occlusion on the upper thigh (optical probe HVM) (Fig. 5C). The temporal traces of [Hb] and [HbO<sub>2</sub>] are obtained by fitting the measured spectrum of  $\Delta\mu_a(\lambda, t)$  (whose value at each wavelength was obtained from Eq. 2) with a linear combination of the HbO<sub>2</sub> and Hb extinction spectra. This procedure results in the application of Eqs. 3 and 4 without the superscript "resp" on  $\Delta\mu_a$ ,  $\Delta[HbO_2]$ , and  $\Delta[Hb]$ . Two oscillatory components are clearly visible in the relative [HbO<sub>2</sub>] and [Hb] traces of Fig. 5A: the first one, associated with the heartbeat (as shown by the pulse oximeter data; top trace in Fig. 5) is at a frequency of ~2.5 Hz, whereas the second one, associated with respiration (as shown by the strain gauge signal; second trace from the top in Fig. 5), is at a frequency of ~0.65 Hz. Only the latter oscillatory component (at a frequency of ~0.23 Hz in human subjects) is clearly visible in Fig. 5B, whereas neither is present in Fig. 5C. Figure 5, B and C, shows additional low-frequency oscillations associated with changes in blood pressure and heart rate. We observe that the strain-gauge signal (second trace from the top in Fig. 5) increases during inspiration and decreases during expiration. The BP filter described in the previous section aims at isolating the oscillatory component at the respiratory frequency by filtering out higher and lower frequency components. The relative [HbO<sub>2</sub>] and [Hb] traces after BP filtering are shown in Fig. 5, bottom. In the case reported in Fig. 5, which is representative of the results reported in this article for  $SvO_2$ -NIRS<sub>resp</sub>, the oscillatory components of [HbO<sub>2</sub>] and [Hb] at the respiratory frequency are in phase with each other and disappear during venous occlusion.

Figure 6 illustrates representative  $\Delta\mu_a^{resp}$  spectra  $R_6$  measured on the piglet's leg (probe PR) (Fig. 6A), and on the human vastus medialis muscle at rest (Fig. 6B), and during venous occlusion on the upper thigh (probe HVM) (Fig. 6C). The y-axis of each panel of Fig. 6 refers to the values of  $\Delta\mu_a^{resp}$  obtained with the BP filter method. The values of  $\Delta\mu_a^{resp}$  computed with the FFT method are normalized by a wavelength-independent



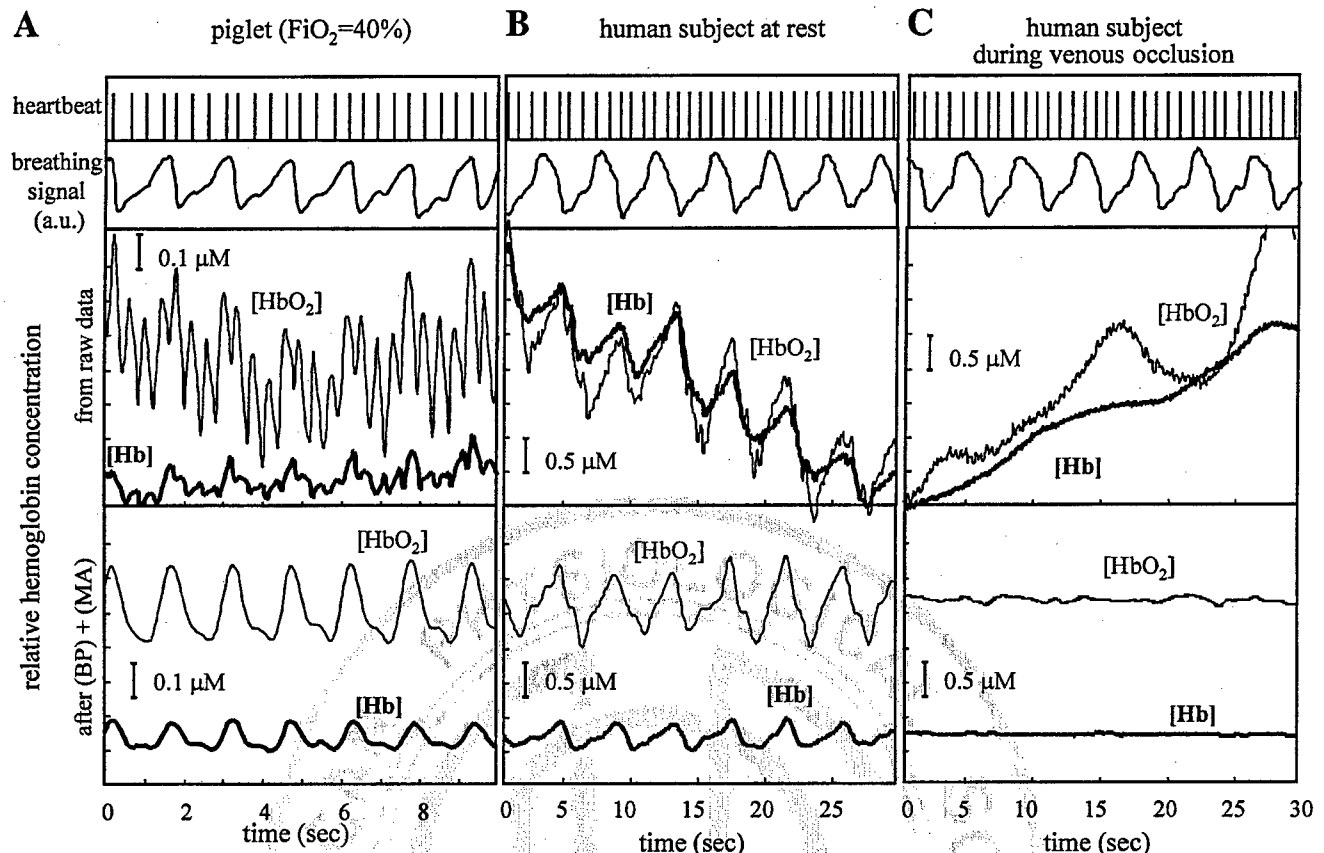


Fig. 5. Representative traces of the relative  $\text{HbO}_2$  concentrations ( $[\text{HbO}_2]$ ) and  $\text{Hb}$  concentrations ( $[\text{Hb}]$ ) measured on the piglet's leg (with optical probe PR) (A) and on the human vastus medialis muscle at rest (B) and during venous occlusion on the upper thigh (optical probe HVM) (C). Bottom panels report the  $[\text{Hb}]$  traces after processing with the digital band-pass filter [band pass (BP) + modeling algorithm (MA)] designed to isolate the oscillations at the respiratory frequency. Top trace represents the piglet's heartbeat monitored by the pulse oximeter. Second trace from the top is the strain gauge signal that monitors the respiratory excursion. The strain gauge signal increases during inspiration and decreases during expiration. a.u., Arbitrary units.

factor to match the BP value of  $\Delta\mu_a^{\text{resp}}$  at 636 nm. The relatively high value of  $\epsilon_{\text{fit}}^{\text{fit}}$  during venous occlusion (Fig. 6C) is an indication of the poor fit, which in turn results from the lack of hemoglobin oscillations at the respiratory frequency (see Fig. 5C, bottom, and the y-axis values of Fig. 5C compared with those of Fig. 5B). Figure 6 also shows the best fit of the hemoglobin absorption spectrum to the BP  $\Delta\mu_a^{\text{resp}}$  and to the FFT  $\Delta\mu_a^{\text{resp}}$ . The best-fit hemoglobin spectra represent the oxygen saturation of hemoglobin, as illustrated in Fig. 1. The value of  $\text{SvO}_2\text{-NIRS}_{\text{resp}}$  is given by Eq. 5.

Figure 7 compares the measurements of  $\text{SvO}_2\text{-NIRS}_{\text{resp}}(\text{BP})$ ,  $\text{SvO}_2\text{-NIRS}_{\text{resp}}(\text{FFT})$ , and  $\text{SvO}_2\text{-blood}$  during cycle A of piglet 1 and during cycle C of piglet 3. The  $\text{SvO}_2\text{-NIRS}_{\text{resp}}(\text{BP})$  traces reported in Fig. 7 were obtained by performing a running average of the breath-to-breath values obtained with the BP method. In Fig. 7, the averaging procedure consists of a 5-point (in Fig. 7A) or 15-point (in Fig. 7B) running average. The assessment of the agreement between the measurements of  $\text{SvO}_2\text{-NIRS}_{\text{resp}}(\text{FFT})$  and  $\text{SvO}_2\text{-blood}$  in the full piglet study is carried out according to the procedure described by Bland and Altman (5). Figure 8A plots the

results of the NIRS method based on the respiratory oscillations of the tissue absorption against the invasive measurement of  $\text{SvO}_2\text{-blood}$ . The shape of the symbols in Fig. 8A indicates the piglet number, whereas the type of fill indicates the location of the NIRS measurement. The range of  $\text{SvO}_2\text{-blood}$  values considered in this study is ~20–95%. The error bars in Fig. 8A are the standard deviations computed from the results of ~800 successive FFTs (as described in MATERIALS AND METHODS). Figure 8B displays the difference between the two readings vs. their average, and it quantifies the discrepancy between the two methods and the possible dependence of such a difference on the level of  $\text{SvO}_2$ . The mean difference between  $\text{SvO}_2\text{-NIRS}_{\text{resp}}$  and  $\text{SvO}_2\text{-blood}$  over the full oxygenation range considered in this study is 1.0% (a measurement of the bias of the  $\text{SvO}_2\text{-NIRS}_{\text{resp}}$  measurement), and the standard deviation of the difference is 5.8%. Figure 8B does not show any striking dependence of the difference on the mean. If we take the values of mean difference  $\pm 2$  SD as the limits of agreement of the two methods (5), we get an estimate of the maximal discrepancies between  $\text{SvO}_2\text{-NIRS}_{\text{resp}}(\text{FFT})$  and  $\text{SvO}_2\text{-blood}$  of -10.6% and +12.6%.

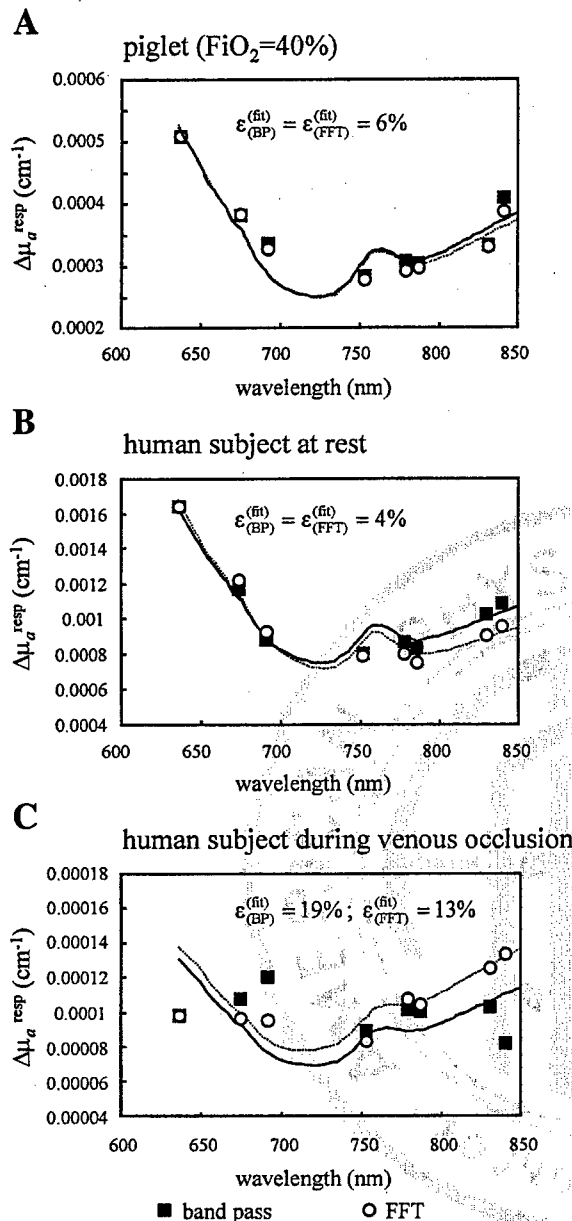


Fig. 6. Representative change in respiratory tissue absorption coefficient ( $\Delta\mu_a^{\text{resp}}$ ) spectra measured with the BP and fast Fourier transform (FFT) methods on the piglet's leg (*probe PR*) (A) and on the human vastus medialis muscle at rest (B) and during venous occlusion on the upper thigh (*probe HVM*) (C). The experimental 8-point  $\Delta\mu_a^{\text{resp}}$  spectra were fitted with the hemoglobin absorption spectrum (with the hemoglobin concentration and extinction as fitting parameters). The values of  $\epsilon^{\text{fit}}$  (defined in the text) for the BP and FFT spectra give a measure of the quality of the fit.

In the human experiment, we found that the NIRS values of  $\text{SvO}_2$  measured with *probe HVM* (placed on top of a visible vein) were typically smaller than those measured with *probe HVL* (placed far from any visible vein). Furthermore, the amplitude of the oscillatory absorption at the respiration (heartbeat) frequency was typically greater (smaller) for the data collected with *probe HVM* than with *probe HVL*. Of the 16  $\text{SvO}_2\text{-NIRS}_{\text{resp}}$  measurements (8 subjects, 2 locations),

we discarded only 2 measurements (because of a value of  $\Sigma^{\text{fit}}$  greater than twice the error in  $\Delta\mu_a^{\text{resp}}$ ), both collected with *probe HVL*. Figure 9 compares the  $\text{SvO}_2\text{-NIRS}_{\text{resp}}$  values measured in the human subjects at rest in which the FFT method and the BP filtering approach were used. Figure 9A shows the good agreement of the two measurements, and Fig. 9B quantifies the average difference (0.9%) and the maximum discrepancies of  $-5.1$  and  $+6.9\%$ , as given by the mean  $\pm$  twice the standard deviation of the differences. Figure 10 reports a similar comparison between  $\text{SvO}_2\text{-NIRS}_{\text{resp}}(\text{FFT})$  and  $\text{SvO}_2\text{-NIRS}_{\text{vO}}$ . As described by Yoxall and Weindling (56), under the assumption that a venous occlusion induces an initial increase in the venous blood volume,  $\text{SvO}_2\text{-NIRS}_{\text{vO}}$  is given by  $[\text{HbO}_2]_0/[\text{Hb}-\text{T}]_0$ , where the dots indicate a time derivative and the subscript 0 indicates the initial time that immediately follows the onset of venous occlusion. The agreement between  $\text{SvO}_2\text{-NIRS}_{\text{resp}}(\text{FFT})$  and  $\text{SvO}_2\text{-NIRS}_{\text{vO}}$  is good, with an average deviation of 0.8% and maximum discrepancies of  $-4.2$  and  $+5.8\%$ . Two horizontal lines in Figs. 8B and 9B indicate the range given by the mean difference  $\pm 2$  SD. The maximum discrepancy among  $\text{SvO}_2\text{-NIRS}_{\text{resp}}(\text{FFT})$ ,  $\text{SvO}_2\text{-NIRS}_{\text{resp}}(\text{BP})$ , and  $\text{SvO}_2\text{-NIRS}_{\text{vO}}$  is less than the maximum deviation between  $\text{SvO}_2\text{-NIRS}_{\text{resp}}(\text{FFT})$  and  $\text{SvO}_2\text{-blood}$  found in piglets (see Fig. 8B).

The effect of muscle exercise on the measurement of  $\text{SvO}_2\text{-NIRS}_{\text{resp}}(\text{BP})$  on top of a visible superficial vein (*probe HVM*) is illustrated in Fig. 11. Although  $\text{SaO}_2$  (measured with a pulse oximeter) is unaffected by the exercise,  $\text{SvO}_2\text{-NIRS}_{\text{resp}}(\text{BP})$  shows a significant postexercise decrease from a baseline value of 75–78% down to a minimum value of  $\sim 54\%$ . The recovery to the baseline value of  $\text{SvO}_2\text{-NIRS}_{\text{resp}}(\text{BP})$  occurs after  $\sim 30$  s. By using the BP approach, we could monitor  $\text{SvO}_2\text{-NIRS}_{\text{resp}}$  at every breathing period, i.e., every  $\sim 5$  s, thus achieving a real-time monitoring of  $\text{SvO}_2$ . We observe that we could not obtain meaningful measurements of  $\text{SvO}_2\text{-NIRS}_{\text{resp}}$  during exercise because of motion artifacts.

## DISCUSSION

**Various methods for measuring  $\text{SvO}_2$ .** The method presented in this article to measure  $\text{SvO}_2$  from the near-infrared absorption oscillations at the respiratory frequency (spiroximetry) can be implemented by using a FFT or a digital BP filter in conjunction with a MA. We have indicated the measurements of  $\text{SvO}_2$  obtained with these two approaches with the notations  $\text{SvO}_2\text{-NIRS}_{\text{resp}}(\text{FFT})$  and  $\text{SvO}_2\text{-NIRS}_{\text{resp}}(\text{BP})$ , respectively. An alternative method for measuring  $\text{SvO}_2$  with NIRS is based on a previously described venous occlusion protocol (13, 39, 55, 56). We have identified the results of this measurement procedure with the notation  $\text{SvO}_2\text{-NIRS}_{\text{vO}}$ . In the human study, the NIRS measurements were conducted at two locations on the thigh. One location was on top of a visible superficial vein of the vastus medialis muscle (*probe HVM*), and the second location was far from visible superficial veins on the

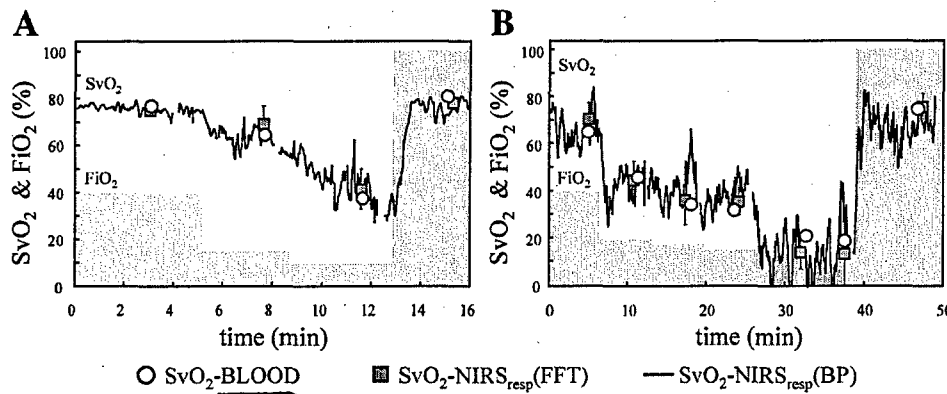


Fig. 7. Comparison between the continuous measurement of  $SvO_2$ -NIRS<sub>resp</sub> (BP) and the discontinuous measurements of  $SvO_2$ -NIRS<sub>resp</sub>(FFT) and  $SvO_2$ -blood. A refers to cycle A of piglet 1, whereas B refers to cycle C of piglet 3. The values of  $FiO_2$  (%), left y-axes during the experiment are indicated by the shaded profiles.

vastus lateralis muscle (*probe HVL*). Finally, the invasive measurement of  $SvO_2$  performed by the gas analysis of venous blood samples is indicated with  $SvO_2$ -blood. In this section, we discuss the different features of these measurements of  $SvO_2$ , and the comparison of their results, as reported in Figs. 7–9.

The FFT and BP filter approaches to near-infrared spirometry. The major advantage of the BP approach is that it allows for a real-time measurement of  $SvO_2$  by providing a reading of  $SvO_2$ -NIRS<sub>resp</sub>(BP) at every respiration cycle. Consequently, this method is particularly effective during transients, as illustrated by the recovery of the  $SvO_2$ -NIRS<sub>resp</sub>(BP) traces corresponding to the sudden increase of  $FiO_2$  to 100% in piglets (see Fig. 6, A and B), or to the end of the exercise period in human subjects (see Fig. 11). On the other hand, the BP filter + MA method is susceptible to fluctuations in the respiratory frequency and to irregular respiration patterns. This accounts for the fact that we did not get reliable readings of  $SvO_2$ -NIRS<sub>resp</sub>(BP) in piglet 2 and in  $FiO_2$  cycles A and B of piglet 3. The FFT method was more robust, producing reliable readings in 56 of 67 cases (84%) in the piglet study and in 14 of 16 cases (87%) in the human study. It is important to observe that 10 of the 11 discarded readings in piglets occurred

at low- $SvO_2$ -NIRS-blood values (20–50%), and one was assigned to motion artifacts. Both discarded readings in the human study were collected with *probe HVL*, which was placed far from visible veins. Therefore, we have found indications that the measurement of  $SvO_2$ -NIRS<sub>resp</sub>(FFT) is particularly robust at  $SvO_2$  values >50% (in piglets) and when the optical probe is placed on top of a visible superficial vein (in human subjects). Although the FFT method, which is based on a measurement of the integrated peak at the respiratory frequency, is less sensitive than the BP method to irregular respiration patterns, it is not applicable during transients. In fact, we did not obtain reliable readings of  $SvO_2$  when the time frame used to compute  $SvO_2$ -NIRS<sub>resp</sub>(FFT) (80 s in piglets, 80–120 s in human subjects) included significant changes in the  $SvO_2$ . When both the FFT and the BP methods can be applied, they provide  $SvO_2$ -NIRS<sub>resp</sub> measurements that are in excellent agreement, as shown in Figs. 6 and 9. The differences between the two measurements (standard deviation of 3.0%) are comparable with measurement errors and significantly less than the maximum deviation between  $SvO_2$ -NIRS<sub>resp</sub>(FFT) and  $SvO_2$ -blood (approximately  $\pm 10\%$ ) observed in the piglet study (see Fig. 8B).

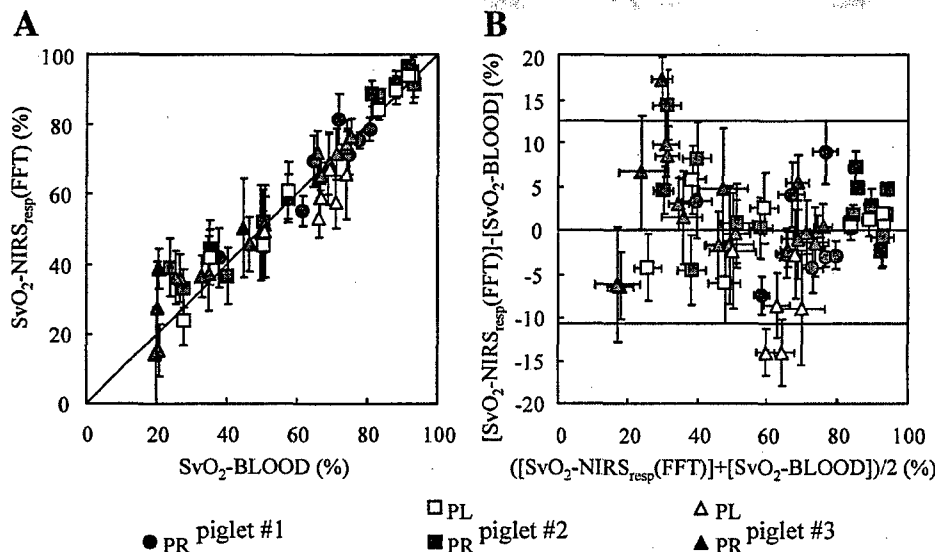
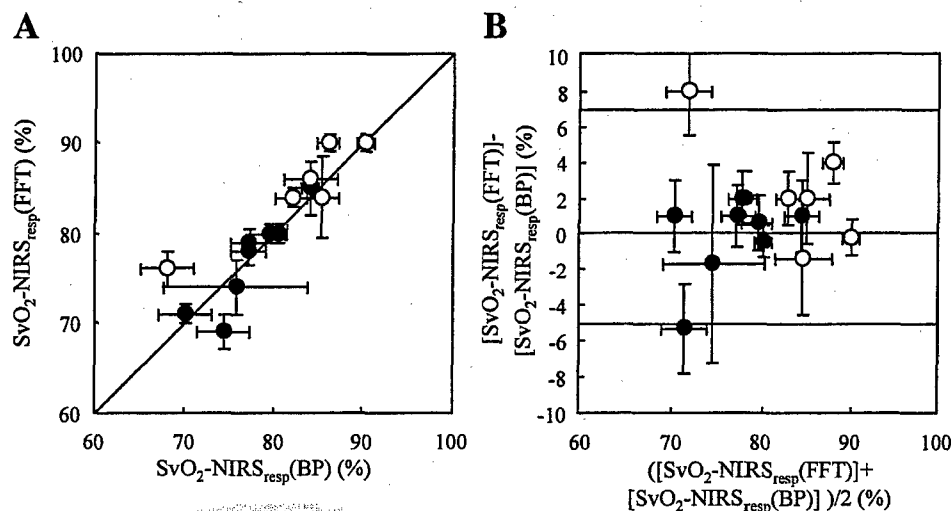


Fig. 8. Comparison of  $SvO_2$ -NIRS<sub>resp</sub>(FFT) and  $SvO_2$ -blood in the piglet study. The shape of the symbols refer to the piglet (circles, piglet 1; squares, piglet 2; triangles, piglet 3), whereas the filling indicates the measurement side (filled symbols, right leg, i.e., *probe PR*; open symbols, left leg, i.e., *probe PL*). A:  $SvO_2$ -NIRS<sub>resp</sub>(FFT) is plotted vs.  $SvO_2$ -blood. B: difference is plotted vs. the average of the 2 measurements. Two horizontal lines indicate the range given by mean difference  $\pm 2$  SD (SD is the standard deviation of the difference between the 2 measurements).

Fig. 9. Comparison of  $SvO_2$ -NIRS<sub>resp</sub> (FFT) and  $SvO_2$ -NIRS<sub>resp</sub>(BP) in the human study. ●, Vastus medialis muscle; i.e., probe HVM. ○, Vastus lateralis muscle; i.e., probe HVL. Probe HVM was placed on top of a visible superficial vein, whereas probe HVL was far from visible veins. A:  $SvO_2$ -NIRS<sub>resp</sub>(FFT) is plotted vs.  $SvO_2$ -NIRS<sub>resp</sub>(BP). B: difference is plotted vs. the average of the 2 measurements. Two horizontal lines in B indicate the range given by mean difference  $\pm$  2 SD.



The NIRS inf means of

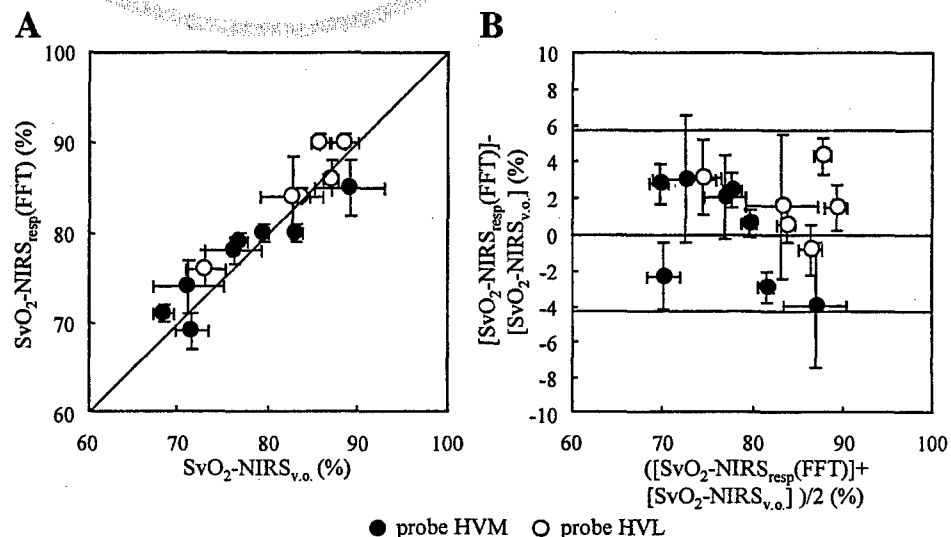
ven. SAT based on resp-induced  
abs. osc. ( ) and on the ven occlusion ( )

Measurements of  $SvO_2$ -NIRS<sub>resp</sub> and  $SvO_2$ -NIRS<sub>vo</sub>  
Both of these NIRS methods to measure the  $SvO_2$  (NIRS<sub>resp</sub> and NIRS<sub>vo</sub>) rely on a change in the volume fraction of venous blood in the tissue. The two major differences between the two methods are as follows. 1) The NIRS<sub>vo</sub> method requires an external perturbation consisting of a pneumatic-cuff-induced venous occlusion, whereas the NIRS<sub>resp</sub> method is only based on the intrinsic blood pressure oscillations induced by normal respiration and can be applied continuously. 2) The NIRS<sub>vo</sub> method can be applied only to limbs, whereas the NIRS<sub>resp</sub> method can, in principle, be applied to any tissue and in particular to the brain, as already shown by Wolf et al. (52). However, we stress that it is always important to verify that the [HbO<sub>2</sub>] and [Hb] oscillate in phase at the respiratory frequency for the NIRS<sub>resp</sub> method to provide reliable measurements of  $SvO_2$ . For instance, Elwell et al. (16) reported out-of-phase oscillations of [Hb] and [HbO<sub>2</sub>] in the human brain,

which would indicate a blood flow rather than volume oscillations, thus rendering the NIRS<sub>resp</sub> method inapplicable. In our human study, we found an excellent agreement between  $SvO_2$ -NIRS<sub>resp</sub>(FFT) and  $SvO_2$ -NIRS<sub>vo</sub>, with a maximum deviation on the order of  $\pm 4-5\%$  (see Fig. 10).

Optical probes PR, PL, HVM, and HVL. In the piglet study, we have found no significant difference between the  $SvO_2$ -NIRS<sub>resp</sub>(FFT) data collected with probes PR (on the right leg) and PL (on the left leg, where the venous catheter was inserted) (see Fig. 8A). This result indicates that noninvasive measurements of  $SvO_2$  on one leg can be meaningfully compared with invasive measurements of  $SvO_2$  on the other leg. In the human study, we found some differences between the  $SvO_2$ -NIRS measurements with probe HVM (placed on top of a visible superficial vein in the vastus medialis muscle) and with probe HVL (placed far from visible veins on the vastus lateralis muscle). As shown in Figs. 8 and 9, the  $SvO_2$ -NIRS

Fig. 10. Comparison of  $SvO_2$ -NIRS<sub>resp</sub> (FFT) and  $SvO_2$ -NIRS<sub>vo</sub> (venous occlusion) in the human study. ●, Vastus medialis muscle; i.e., probe HVM. ○, Vastus lateralis muscle; i.e., probe HVL. Probe HVM was placed on top of a visible superficial vein, whereas probe HVL was far from visible veins. A:  $SvO_2$ -NIRS<sub>resp</sub>(FFT) is plotted vs.  $SvO_2$ -NIRS<sub>vo</sub>. B: difference is plotted vs. the average of the 2 measurements. Two horizontal lines in B indicate the range given by mean difference  $\pm$  2 SD.



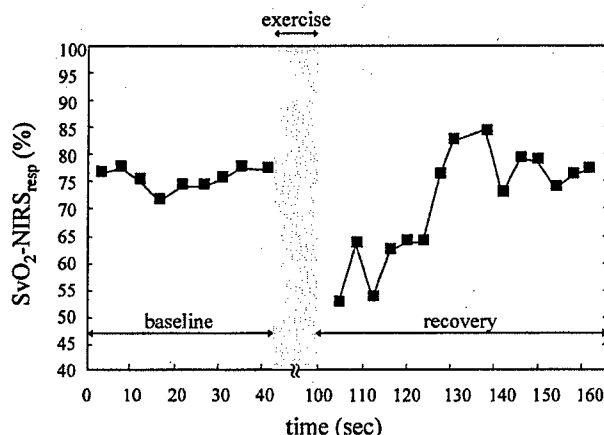


Fig. 11. Continuous measurement of  $SvO_2$ -NIRS<sub>resp</sub>(BP) with optical probe HVM (vastus medialis muscle, on top of a visible superficial vein) on a healthy human subject during baseline and after isometric muscle exercise (recovery).

readings (with both the NIRS<sub>resp</sub> and NIRS<sub>vo</sub> method) of probe HVM (see Figs. 8 and 9) were typically smaller than the readings of probe HVL (see Figs. 8 and 9). We assign this result to a partial contribution from the capillary and/or arterial compartments picked up by probe HVL. In fact, although the optical data from probe HVM shown in Fig. 4, B and C, do not show any visible contribution from the arterial pulsation, data from probe HVL (not shown) do contain pulsatile components at the heartbeat frequency. As a result, we believe that the optical probe should be placed on top of visible superficial veins for more accurate readings of  $SvO_2$ -NIRS<sub>resp</sub> on human subjects. We believe that the reason that  $SvO_2$ -NIRS<sub>resp</sub> readings in the piglet study were in close agreement with the invasive measurement of  $SvO_2$ , despite the evident arterial pulsation in Fig. 5A, is related to the smaller extent of respiratory sinus arrhythmia in piglets with respect to humans. In fact, respiratory sinus arrhythmia is the main origin of the arterial oscillations at the respiratory frequency (38). The larger role played by respiratory sinus arrhythmia in human subjects with respect to piglets will probably require a more careful interpretation of the optical data for sioximetry. However, the results of Fig. 11 show the practical applicability of sioximetry to human subjects, so that we do not expect respiratory sinus arrhythmia to introduce an intrinsic limitation of the method.

**Noninvasive vs. invasive measurements of  $SvO_2$ .** The comparison between  $SvO_2$ -NIRS<sub>resp</sub>(FFT) and  $SvO_2$ -blood in the piglet study shows a maximum deviation range of -10.6% to +12.6%. The local character of the  $SvO_2$  (as opposed to the systemic nature of the  $SaO_2$ ) requires some caution in the comparison of invasive ( $SvO_2$ -blood) and noninvasive ( $SvO_2$ -NIRS) measurements of  $SvO_2$ . In fact, in our piglet study,  $SvO_2$ -blood was measured from blood samples drawn from the femoral vein, whereas  $SvO_2$ -NIRS<sub>resp</sub> was measured with an optical probe placed on the leg

muscle. It is likely that the NIRS oscillatory signal (at the respiratory frequency) is not just representative of the femoral vein and may therefore be indicative of the oxygen consumption at different tissue areas than those affecting the femoral vein saturation. This fact may not lead to significant differences under rest conditions, but it may be important under stress. Although we found a good agreement between  $SvO_2$ -NIRS<sub>resp</sub>(FFT) and  $SvO_2$ -blood over the whole range of  $FI_{O_2}$  values considered (see Fig. 8), we observed a meaningfully greater standard deviation of the differences over the 20–55%  $SvO_2$ -blood range ( $SD = 7.8\%$ ) than in the 55–95% range ( $SD = 3.6\%$ ).

**Effect of muscle exercise on  $SvO_2$ -NIRS<sub>resp</sub>(BP).** The result reported in Fig. 11 serves the purpose of further illustrating the potential of the  $SvO_2$ -NIRS<sub>resp</sub>(BP) measurement approach. In fact, Fig. 11 shows the feasibility of monitoring the  $SvO_2$  in real time on a breath-to-breath basis (one data point every 4–5 s). Furthermore, the baseline  $SvO_2$ -NIRS<sub>resp</sub>(BP) value of 75–78% and the exercise-induced drop indicate the venous origin of the saturation measurement, since the  $SaO_2$  measurement provided by the pulse oximeter stayed constant at  $98 \pm 1\%$  for the whole measurement period. On the other hand, Fig. 11 reports only one representative case, and more studies are required to quantify the effect of muscle exercise on the measurement of  $SvO_2$ -NIRS<sub>resp</sub>.

In conclusion, we have presented a noninvasive approach to measure the  $SvO_2$  in tissues from the near-infrared spectrum of the amplitude of respiration-induced absorption oscillations. We have implemented this approach, which we call near-infrared sioximetry, by processing the optical data with a FFT method or with a digital BP filter in conjunction with a MA. More sophisticated data processing schemes may further improve the effectiveness and the range of applicability of sioximetry. The  $SvO_2$  measurements reported in this article complement previously demonstrated NIRS measurements of  $StO_2$  (8, 27) and  $SaO_2$  (21). Therefore, our results may lead to the design of a noninvasive optical instrument capable of providing simultaneous and real-time measurements of local  $SaO_2$ ,  $StO_2$ , and  $SvO_2$ .

We thank Aradhana Arora, Matthew Hoimes, and Tanya Fridman for technical assistance during the preliminary measurements on human subjects and Dennis Hueber and Valentina Quaresima for helpful discussions. We also thank Enrico Gratton for lending us the eight-wavelength laser board used in this study. We are grateful to the volunteers who participated in this study.

This research is supported by the National Institutes of Health Grants R01-MH-62854 (to M. A. Franceschini) and R29-NS-38842 (to D. A. Boas) and by the US Army Awards DAMD17-99-2-9001 (to D. A. Boas) and DAMD17-99-1-9218 (to S. Fantini). D. A. Boas acknowledges financial support from the Center for Innovative Minimally Invasive Therapies.

The material presented does not necessarily reflect the position or the policy of the U.S. Government, and no official endorsement should be inferred.

## REFERENCES

1. Aoyagi T, Kishi M, Yamaguchi K, and Watanabe S. Improvement of the earpiece oximeter. In: *Abstracts of the Japanese Society of Medical Electronics and Biological Engineering, Tokyo, Japan, 1974*, p. 90-91.
2. Bank W, Park J, Lech G, and Chance B. Near-infrared spectroscopy in the diagnosis of mitochondrial disorders. *Biofactors* 7: 243-245, 1998.
3. Benaron DA, Hintz SR, Villringer A, Boas D, Kleinschmidt A, Frahm J, Hirth C, Obrig H, van Houten JC, Kermit EL, Cheong WF, and Stevenson DK. Noninvasive functional imaging of human brain using light. *J Cereb Blood Flow Metab* 20: 469-477, 2000.
4. Berne RM and Levy MN. *Cardiovascular Physiology* (7th ed.). St. Louis, MO: Mosby Year Book, 1997, p. 196.
5. Bland JM and Altman DG. Statistical methods for assessing agreement between two methods of clinical measurement. *Lancet* 1: 307-310, 1986.
6. Butler JP, Miki H, Suzuki S, and Takishima T. Step response of lung surface-to-volume ratio by light-scattering stereology. *J Appl Physiol* 67: 1873-1880, 1989.
7. Casavola C, Paunescu LA, Fantini S, and Gratton E. Blood flow and oxygen consumption with near-infrared spectroscopy and venous occlusion: spatial maps and the effect of time and pressure of inflation. *J Biomed Opt* 5: 269-276, 2000.
8. Chance B, Cope M, Gratton E, Ramanujam N, and Tromberg BJ. Phase measurement of light absorption and scatter in human tissues. *Rev Sci Instrum* 68: 3457-3481, 1998.
9. Chance B, Dait M, Zhang C, Hamaoka T, and Hagerman F. Recovery from exercise-induced desaturation in the quadriceps muscle of elite competitive rowers. *Am J Physiol Cell Physiol* 262: C766-C775, 1992.
10. Colier WN, Quaresima V, Wenzel R, van der Sluijs MC, Oeseburg B, Ferrari M, and Villringer A. Simultaneous near-infrared spectroscopy monitoring of left and right occipital areas reveals contralateral hemodynamic changes upon hemifield paradigm. *Vision Res* 41: 97-102, 2001.
11. Cope M. *The Application of Near-Infrared Spectroscopy to Non-Invasive Monitoring of Cerebral Oxygenation in the Newborn Infant* (PhD thesis). London: Biomedical Optics Research Group, University College, 1991, p. 263-269. [Online] <http://www.med-physics.ucl.ac.uk/research/borg/homepages/mcope/index.htm> [2001, May 10]
12. De Blasi R, Cope M, Elwell C, Safoue F, and Ferrari M. Noninvasive measurement of human forearm oxygen consumption by near infrared spectroscopy. *Eur J Appl Physiol* 67: 20-25, 1993.
13. De Blasi RA, Ferrari M, Natali A, Conti G, Mega A, and Gasparetto A. Noninvasive measurement of forearm blood flow and oxygen consumption by near-infrared spectroscopy. *J Appl Physiol* 76: 1388-1393, 1994.
14. Delpy DT, Cope M, van der Zee P, Arridge S, Wray S, and Wyatt JS. Estimation of optical pathlength through tissue from direct time of flight measurement. *Phys Med Biol* 33: 1433-1442, 1988.
15. Elwell CE, Matcher SJ, Tysczuk L, Meek JH, and Delpy DT. Measurement of cerebral venous saturation in adults using near infrared spectroscopy. *Adv Exp Med Biol* 411: 453-460, 1997.
16. Elwell CE, Owen-Reece H, Cope M, Edwards AD, Wyatt JS, Reynolds EOR, and Delpy DT. Measurement of changes in cerebral haemodynamic during inspiration and expiration using near infrared spectroscopy. *Adv Exp Med Biol* 388: 619-626, 1994.
17. Fantini S, Franceschini MA, Fishkin JB, Barbieri B, and Gratton E. Quantitative determination of the absorption spectra of chromophores in strongly scattering media: a light-emitting-diode based technique. *Appl Opt* 33: 5204-5213, 1994.
18. Fantini S, Franceschini MA, and Gratton E. Effective source term in the diffusion equation for photon transport in turbid media. *Appl Opt* 36: 156-163, 1997.
19. Fantini S, Franceschini MA, Maier JS, Walker SA, Barbieri B, and Gratton E. Frequency-domain multichannel optical detector for non-invasive tissue spectroscopy and oximetry. *Opt Eng* 34: 32-42, 1995.
20. Franceschini MA, Fantini S, Palumbo R, Pasqualini L, Vaudo G, Franceschini E, Gratton E, Palumbo B, Innocente S, and Mannarino E. Quantitative near-infrared spectroscopy on patients with peripheral vascular disease. *Proc SPIE* 3194: 112-115, 1998.
21. Franceschini MA, Gratton E, and Fantini S. Non-invasive optical method to measure tissue and arterial saturation: an application to absolute pulse oximetry of the brain. *Opt Lett* 24: 829-831, 1999.
22. Fantini S, Hueber D, Franceschini MA, Gratton E, Rosenfeld W, Stubblefield PG, Maulik D, and Stankovic MR. Non-invasive optical monitoring of the newborn piglet brain using continuous-wave and frequency-domain methods. *Phys Med Biol* 44: 1543-1563, 1999.
23. Franceschini MA, Moesta KT, Fantini S, Gaida G, Gratton E, Jess H, Mantulin WW, Seeber M, Schlag PM, and Kaschke M. Frequency-domain instrumentation enhances optical mammography: initial clinical results. *Proc Natl Acad Sci USA* 94: 6468-6473, 1997.
24. Franceschini MA, Toronov V, Filiaci ME, Gratton E, and Fantini S. On-line optical imaging of the human brain with 160-ms temporal resolution. *Opt Express* 6: 49-57, 2000.
25. Franceschini MA, Wallace D, Barbieri B, Fantini S, Mantulin WW, Pratesi S, Donzelli GP, and Gratton E. Optical study of the skeletal muscle during exercise with a second generation frequency-domain tissue oximeter. *Proc SPIE* 2979: 807-814, 1997.
26. Fung YC. *Biomechanics—Circulation* (2nd ed.). New York: Springer-Verlag, 1997, p. 243.
27. Gratton E, Fantini S, Franceschini MA, Gratton G, and Fabiani M. Measurements of scattering and absorption changes in muscle and brain. *Philos Trans R Soc Lond B Biol Sci* 352: 727-735, 1997.
28. Grosenick D, Wabnitz H, and Rinneberg H. Time-resolved imaging of solid phantoms for optical mammography. *Appl Opt* 36: 221-231, 1997.
29. Hamaoka T, Iwane H, Shimomitsu T, Katsumura T, Murase N, Nishio S, Osada T, Kurosawa Y, and Chance B. Noninvasive measures of oxidative metabolism on working human muscles by near-infrared spectroscopy. *J Appl Physiol* 81: 1410-1417, 1996.
30. Hoshi Y and Tamura M. Near-infrared optical detection of sequential brain activation in the prefrontal cortex during mental tasks. *Neuroimage* 5: 292-297, 1997.
31. Hueber DM, Franceschini MA, Ma HY, Xu Q, Ballesteros JR, Fantini S, Wallace D, Ntziachristos V, and Chance B. Non-invasive and quantitative near-infrared hemoglobin spectrometry in the piglet brain during hypoxic stress, using a frequency-domain multi-distance instrument. *Phys Med Biol* 46: 41-62, 2001.
32. Komiya T, Shigematsu H, Yasuhara H, and Muto T. Near-infrared spectroscopy grades the severity of intermittent claudication in diabetics more accurately than ankle pressure measurement. *Br J Surg* 87: 459-466, 2000.
33. Kooijman HM, Hopman MT, Colier WN, van der Vliet JA, and Oeseburg B. Near infrared spectroscopy for noninvasive assessment of claudication. *J Surg Res* 72: 1-7, 1997.
34. Liu H, Boas DA, Zhang Y, Yodh AG, and Chance B. Determination of optical properties and blood oxygenation in tissue using continuous NIR light. *Phys Med Biol* 40: 1983-1993, 1995.
35. Meek JH, Elwell CE, Khan MJ, Romaya J, Wyatt JS, Delpy DT, and Zeki S. Regional changes in cerebral haemodynamics as a result of a visual stimulus measured by near infrared spectroscopy. *Proc R Soc Lond B Biol Sci* 261: 351-356, 1995.
36. Mendelson Y. Pulse oximetry: theory and applications for non-invasive monitoring. *Clin Chem* 38: 1601-1607, 1992.
37. Millikan GA. The oximeter, an instrument for measuring continuously the oxygen saturation of arterial blood in man. *Rev Sci Instrum* 13: 434-444, 1942.
38. Mohrman DE and Heller LJ. *Cardiovascular Physiology* (4th ed.). New York: McGraw-Hill, Health Professions Division, 1997, p. 177.

---

## CHAPTER 7

# FREQUENCY-DOMAIN TECHNIQUES FOR TISSUE SPECTROSCOPY AND IMAGING

Sergio Fantini  
Maria Angela Franceschini  
*Tufts University, USA*

### CONTENTS

7.1	Introduction / 2
7.2	Instrumentation, Modulation Methods, and Signal Detection / 2
7.2.1	Lasers and arc lamps / 3
7.2.2	Pulsed sources / 3
7.2.3	Laser diodes and light-emitting diodes (LEDs) / 4
7.2.4	Optical detectors / 4
7.2.5	Heterodyne detection, digital signal processing, and Fourier filtering / 4
7.2.6	A frequency-domain tissue spectrometer / 5
7.3	Modeling Light Propagation in Scattering Media / 9
7.3.1	The Boltzmann transport equation (BTE) / 9
7.3.2	Expansion of the Boltzmann equation in spherical harmonics / 10
7.3.3	The $P_N$ approximation / 13
7.3.4	The $P_1$ approximation / 13
7.3.5	The reduced scattering coefficient / 16
7.3.6	The $P_1$ equation and the standard diffusion equation (SDE) / 17
7.3.7	Solution of the standard diffusion equation in the frequency domain / 19
7.4	Tissue Spectroscopy and Oximetry / 20
7.4.1	Optical properties of biological tissue / 20
7.4.2	Absorption spectroscopy of tissues / 22
7.4.3	Near-infrared tissue oximetry / 23
7.4.4	Measurements of optical scattering in tissues / 27
7.5	Optical Imaging of Tissues / 29
7.5.1	General concepts / 29
7.5.2	Noninvasive optical imaging of the human brain / 30
7.5.3	Optical mammography / 33
7.6	Future Directions / 37
	Acknowledgments / 39
	References / 39



### 7.2.1 LASERS AND ARC LAMPS

The emission of continuous-wave lasers and arc lamps can be modulated using devices based on the electro-optical (Pockels cells)<sup>4</sup> or acousto-optical<sup>5,6</sup> effect. A Pockels cell is a birefringent crystal whose indices of refraction can be varied by applying an electric field. The application of a time-varying voltage to the Pockels cell modulates the relative phase delay of the light components polarized along the two principal axes of the cell. If this relative phase delay, or retardation, oscillates between 0 and  $\pi$  when the modulated Pockels cell is sandwiched between two crossed linear polarizers, each at an angle of 45 deg with respect to the principal axes of the cell, one achieves an intensity modulator. In fact, no light is transmitted when the retardation is 0, while all light is transmitted when the retardation is  $\pi$ . An acousto-optic modulator is a material that uses the piezoelectric and the photoelastic effects to convert an oscillating electric field into mechanical vibrations, which in turn induce a spatially dependent index of refraction. When a standing acoustic wave is established, the acousto-optic crystal behaves as an oscillating refractive index grating that modulates the transmitted light by time-varying diffraction. Both electro-optic and acousto-optic devices require the light beam to be collimated. In the case of arc lamps, appropriate collimation optics are required. Pockels cells provide effective modulations up to about 500 MHz, and acousto-optic modulators up to about 300 MHz.

The wavelength of the laser is chosen on the basis of the requirements of the particular application (absorption band of a chromophore, optimal penetration depth in tissues, etc.). Examples of externally modulated cw lasers suitable for optical studies of tissues include the krypton ion (647 nm) and He-Ne (633 nm) lasers. Dye lasers pumped by either argon or krypton afford continuous tunability over a wide spectral range that covers the whole visible band. Arc lamps (Xe, Xe-Hg, etc.) provide continuous spectral emission from the UV (230 nm) to the near-infrared (1100 nm). Therefore, they are ideal sources for spectroscopic studies when a wide and continuous spectral range is required.

### 7.2.2 PULSED SOURCES

It is possible to achieve a large modulation bandwidth by exploiting the harmonic content of pulsed sources with high repetition rates. These sources can be either mode-locked pulsed lasers (Nd:YAG, Ti:sapphire, dye lasers, etc.)<sup>7</sup> or synchrotron radiation.<sup>8,9</sup> The repetition rate of the pulses gives the fundamental frequency, whereas the pulse width determines the width of the power spectrum band. The power spectrum of mode-locked lasers extends well above 10 GHz, an upper limit in frequency-domain spectroscopy imposed by the optical detectors rather than the light sources. The wavelengths of the above-mentioned lasers are 1064 nm for the Nd:YAG, 660–1180 nm (tunable) for the Ti:sapphire, and 625–780 nm (tunable) for dye lasers using DCM or oxanine 1 dyes. A unique pulsed source is provided by synchrotron radiation, which continuously covers the UV/visible/near-infrared spectrum.



to-voltage conversion and low-pass filtering, the low-frequency signal is digitized. The A/D sampling rate is an integer multiple of  $\Delta f$  ( $n\Delta f$ ), so that the digital sampling is synchronous with the cross-correlation signal. The sampling theorem<sup>22</sup> states that  $n$  must be equal to at least 2 for the complete determination of the harmonic at frequency  $\Delta f$ . A higher sampling rate allows for the discrimination of higher harmonics. Typical values of  $n$  range from 4 to 256. The digital signal processing consists of a preliminary average of the data sampled over a number of cross-correlation periods, followed by the discrimination of the frequency harmonic at  $\Delta f$  by discrete Fourier transform. The first filter (averaging) causes destructive interference of all the frequencies that are not multiples of  $\Delta f$ , while the discrete Fourier transform resolves each harmonic of  $\Delta f$ . The rejection of higher harmonics is accomplished by a factor greater than 2000 (Ref. [21]). Figure 7.1 shows a schematic illustration of the heterodyne detection and digital acquisition.

### 7.2.6 A FREQUENCY-DOMAIN TISSUE SPECTROMETER

We now describe a specific frequency-domain instrument for near-infrared spectroscopy and imaging of tissues. After the initial design and the implementation of a working prototype at the University of Illinois,<sup>23</sup> this instrument has undergone engineering and software development at ISS, Inc., Champaign, IL. A schematic diagram of the instrument is shown in Figure 7.2. The light sources are laser diodes that are DC biased near threshold for laser operation. A superimposed 110-MHz radio-frequency current signal modulates the optical output of the laser diodes with a modulation depth close to 100%. The optical detectors are photomultiplier

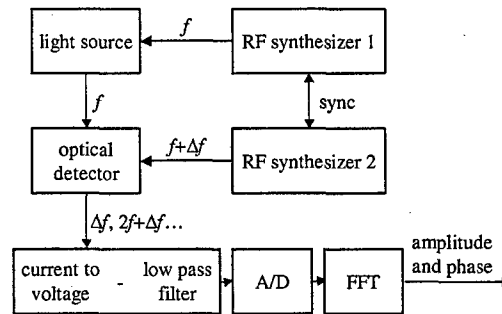


**Figure 7.1** Heterodyne detection scheme and digital signal processing with Fourier filter. The intensity of the light source is modulated at a radio-frequency (RF)  $f$ , typically on the order of 100 MHz. The beating between the detected signal at frequency  $f$  and the down-conversion signal at frequency  $f + \Delta f$  determines a low frequency component  $\Delta f$  that is filtered, digitized (A/D), and fast Fourier transformed (FFT) to yield the amplitude and phase readings. The two radio-frequency synthesizers are synchronized (sync).

that the 758-nm lasers (now discontinued) can be replaced by 690-nm lasers (for instance, Hitachi HL6738MG). Furthermore, the laser diodes are mounted on interchangeable boards, so that one can change the laser wavelength according to the specific application. For instance, one can use boards containing lasers emitting at eight different wavelengths for tissue spectroscopy (for instance, Figure 7.5 reports data collected at 633, 670, 751, 776, 786, 814, 830, and 841 nm (Ref. [24])). Alternatively, one can use a laser board containing diodes emitting at the same wavelength to maximize the number of source locations in single-wavelength optical imaging. In general, the instrument provides 2 parallel detectors and 16 sources, resulting in 32 source-detector channels. The optical probes shown in Figure 7.2 are designed to perform quantitative tissue oximetry. They implement the multi-distance measurement scheme<sup>10,25</sup> that was found to be robust and accurate for *in-vivo* applications. This scheme consists of placing multiple (in this case, four) source fibers at different distances from the single detector fiber. In this fashion, one measures the spatial dependence of the DC intensity, AC amplitude, and phase data, which is related to the tissue optical coefficients by a diffusion model (see Section 7.3.7). If two wavelengths are used, each illumination location consists of two source fibers (one per wavelength). One of the advantages of the multidistance scheme is its insensitivity to motion artifacts, which allows for measurement while the subject moves or exercises [see Figure 7.6c]. Multiple laser diodes time-share the optical detector by means of a multiplexing circuit that turns the laser diodes on and off in sequence, so that only one laser is on at any given time. The multiplexing rate, which determines the on-time of each laser diode, is adjustable by software. A typical multiplexing rate of 100 Hz corresponds to a 10-ms on-time per diode. The laser rise time, determined by protection circuitry, is about 1 ms. Therefore, the data collected during the first 1 ms of the on-time period of each laser are discarded. During a typical 10-ms-long laser on-time, 45 cross-correlation periods are processed (the 5-kHz cross-correlation frequency corresponds to a period of 0.2 ms). As few as 25 cross-correlation periods (5 ms) can be processed per laser on-time, leading to a maximum multiplexing rate of about 170 Hz. Faster computers and higher cross-correlation frequencies may further increase the data acquisition rate. A number of multiplexing cycles (selected by software) can be averaged to increase the signal-to-noise ratio when fast measurements are not required.

The instrumental noise, which depends on the acquisition time, is typically much smaller than the physiological fluctuations observed *in vivo*. The noise can be estimated by the standard deviation of the temporal fluctuations of the measured data. Figure 7.3 shows typical temporal traces of the average intensity, amplitude, phase, absorption coefficient, and reduced scattering coefficient measured with an acquisition time per diode of 160 ms (average of sixteen 10-ms cycles) on a tissuelike solid phantom (made of silicone). The optical coefficients of the phantom [Figure 7.3d] match typical optical properties of blood-perfused tissues in the near-infrared. The standard deviation errors in the various readings are reported in Table 7.1. The instrumental errors decrease for longer acquisition times.

### 7.3 MODELING LIGHT PROPAGATION IN SCATTERING MEDIA

#### 7.3.1 THE BOLTZMANN TRANSPORT EQUATION (BTE)

The Boltzmann transport equation (BTE) is a balance relationship that describes the flow of particles in scattering and absorbing media. The propagation of light in optically turbid media can be modeled by the transport equation, where the photons are treated as the transported particles. If we denote the angular photon density with  $u(\mathbf{r}, \hat{\Omega}, t)$ , which is defined as the number of photons per unit volume per unit solid angle traveling in direction  $\hat{\Omega}$  at position  $\mathbf{r}$  and time  $t$ , we can write the BTE as follows:<sup>26</sup>

$$\begin{aligned} \frac{\partial u(\mathbf{r}, \hat{\Omega}, t)}{\partial t} = & -v\hat{\Omega} \cdot \nabla u(\mathbf{r}, \hat{\Omega}, t) - v(\mu_a + \mu_s)u(\mathbf{r}, \hat{\Omega}, t) \\ & + v\mu_s \int_{4\pi} u(\mathbf{r}, \hat{\Omega}', t) f(\hat{\Omega}', \hat{\Omega}) d\hat{\Omega}' + q(\mathbf{r}, \hat{\Omega}, t), \end{aligned} \quad (7.1)$$

where  $v$  is the speed of light in the medium,  $\mu_a$  is the absorption coefficient (units of  $\text{cm}^{-1}$ ),  $\mu_s$  is the scattering coefficient (units of  $\text{cm}^{-1}$ ),  $f(\hat{\Omega}', \hat{\Omega})$  is the phase function or the probability density of scattering a photon that travels along direction  $\hat{\Omega}'$  into direction  $\hat{\Omega}$ , and  $q(\mathbf{r}, \hat{\Omega}, t)$  is the source term.  $q(\mathbf{r}, \hat{\Omega}, t)$  has units of  $\text{s}^{-1} \text{m}^{-3} \text{sr}^{-1}$  and represents the number of photons injected by the light source per unit volume, per unit time, per unit solid angle at position  $\mathbf{r}$ , time  $t$ , and direction  $\hat{\Omega}$ . The left-hand side of Eq. (7.1) represents the temporal variation of the angular photon density. Each one of the terms on the right-hand side represents a specific contribution to this variation. The first term is the net gain of photons at position  $\mathbf{r}$  and direction  $\hat{\Omega}$  due to the flow of photons. The second term is the loss of photons at  $\mathbf{r}$  and  $\hat{\Omega}$  as a result of collisions (absorption and scattering). The third term is the gain of photons at  $\mathbf{r}$  and  $\hat{\Omega}$  due to scattering. Finally, the fourth term is the gain of photons due to the light sources. Let us now define some of the quantities used to describe photon transport.

*Angular photon density:  $u(\mathbf{r}, \hat{\Omega}, t)$*

$u(\mathbf{r}, \hat{\Omega}, t)$  is defined such that  $u(\mathbf{r}, \hat{\Omega}, t) d\mathbf{r} d\hat{\Omega}$  represents the number of photons in  $d\mathbf{r}$  that travel in a direction within  $d\hat{\Omega}$  around  $\hat{\Omega}$ . The units of  $u(\mathbf{r}, \hat{\Omega}, t)$  are  $\text{m}^{-3} \text{sr}^{-1}$ .

*Photon radiance:  $L(\mathbf{r}, \hat{\Omega}, t)$*

$L(\mathbf{r}, \hat{\Omega}, t) = vu(\mathbf{r}, \hat{\Omega}, t)$ .  $L(\mathbf{r}, \hat{\Omega}, t) d\hat{\Omega}$  represents the number of photons traveling per unit time per unit area (perpendicular to  $\hat{\Omega}$ ) in a range of directions within  $d\hat{\Omega}$  around  $\hat{\Omega}$ . The units of  $L(\mathbf{r}, \hat{\Omega}, t)$  are  $\text{s}^{-1} \text{m}^{-2} \text{sr}^{-1}$ .

*Photon density:  $U(\mathbf{r}, t)$*

$U(\mathbf{r}, t) = \int_{4\pi} u(\mathbf{r}, \hat{\Omega}, t) d\hat{\Omega}$ . The photon density is the number of photons per unit volume. The units are  $\text{m}^{-3}$ .

nomials, by recalling that a function  $H(x)$  (which is sectionally continuous together with its derivative in the interval  $[-1, 1]$ ) has the general Legendre series representation<sup>31</sup>

$$H(x) = \sum_{l=0}^{\infty} \frac{2l+1}{2} H_l P_l(x), \quad (7.5)$$

where  $P_l(x)$  is the Legendre polynomial of order  $l$ , and  $H_l = \int_{-1}^1 H(x') P_l(x') dx'$ . We then write

$$\begin{aligned} f(\hat{\Omega}' \cdot \hat{\Omega}) &= \sum_{l=0}^{\infty} \frac{2l+1}{4\pi} f_l P_l(\hat{\Omega}' \cdot \hat{\Omega}) \\ &= \sum_{l=0}^{\infty} \sum_{m=-l}^l f_l Y_l^{m*}(\hat{\Omega}') Y_l^m(\hat{\Omega}), \end{aligned} \quad (7.6)$$

where the last expression follows from the addition theorem for spherical harmonics,<sup>31</sup> namely  $P_l(\hat{\Omega}' \cdot \hat{\Omega}) = 4\pi/(2l+1) \sum_{m=-l}^l Y_l^{m*}(\hat{\Omega}') Y_l^m(\hat{\Omega})$ . Here,  $f_l = 2\pi \int_{-1}^1 f(\cos \gamma) P_l(\cos \gamma) d(\cos \gamma)$ .

By substituting these expressions into Eq. (7.1), we obtain

$$\begin{aligned} \sum_{l=0}^{\infty} \sum_{m=-l}^l \left\{ \left[ \frac{\partial}{\partial t} + v \hat{\Omega} \cdot \nabla + v(\mu_a + \mu_s) \right] u_{lm}(\mathbf{r}, t) Y_l^m(\hat{\Omega}) - q_{lm}(\mathbf{r}, t) Y_l^m(\hat{\Omega}) \right. \\ \left. - v \mu_s \int_{4\pi} u_{lm}(\mathbf{r}, t) Y_l^m(\hat{\Omega}') \sum_{l'=0}^{\infty} \sum_{m'=-l'}^{l'} f_{l'} Y_{l'}^{m'*}(\hat{\Omega}') Y_{l'}^{m'}(\hat{\Omega}) d\hat{\Omega}' \right\} = 0. \end{aligned} \quad (7.7)$$

The integral in  $d\hat{\Omega}'$  can be calculated using the orthogonality property of the spherical harmonics:  $\int_{4\pi} Y_{l'}^{m'*}(\hat{\Omega}') Y_{l'}^{m'}(\hat{\Omega}') d\hat{\Omega}' = \delta_{ll'} \delta_{mm'}$ . The BTE thus becomes

$$\sum_{l=0}^{\infty} \sum_{m=-l}^l \left( \left\{ \frac{\partial}{\partial t} + v \hat{\Omega} \cdot \nabla + v[\mu_s(1 - f_l) + \mu_a] \right\} u_{lm}(\mathbf{r}, t) - q_{lm}(\mathbf{r}, t) \right) Y_l^m(\hat{\Omega}) = 0. \quad (7.8)$$

We then multiply this equation by  $Y_L^{M*}(\hat{\Omega})$  and integrate over  $\hat{\Omega}$  to obtain the relationship between the specific coefficients  $u_{LM}$  and  $q_{LM}$ , and all the coefficients of the spherical harmonic expansion of  $u$ ,  $u_{lm}$ :

$$\begin{aligned} \frac{\partial}{\partial t} u_{LM}(\mathbf{r}, t) + v[\mu_s(1 - f_l) + \mu_a] u_{LM}(\mathbf{r}, t) \\ + v \sum_{l=0}^{\infty} \sum_{m=-l}^l \int_{4\pi} \hat{\Omega} \cdot \nabla u_{lm}(\mathbf{r}, t) Y_l^m(\hat{\Omega}) Y_L^{M*}(\hat{\Omega}) d\hat{\Omega} = q_{LM}(\mathbf{r}, t). \end{aligned} \quad (7.9)$$

$$\begin{aligned}
& \frac{\partial}{\partial t} u_{LM}(\mathbf{r}, t) + v[\mu_s(1 - f_L) + \mu_a] u_{LM}(\mathbf{r}, t) \\
& + \frac{1}{2} \left[ \frac{(L - M + 1)(L - M + 2)}{(2L + 1)(2L + 3)} \right]^{1/2} \left( \frac{\partial}{\partial x} - i \frac{\partial}{\partial y} \right) v u_{L+1}^{M-1}(\mathbf{r}, t) \\
& - \frac{1}{2} \left[ \frac{(L + M)(L + M - 1)}{(2L + 1)(2L - 1)} \right]^{1/2} \left( \frac{\partial}{\partial x} - i \frac{\partial}{\partial y} \right) v u_{L-1}^{M-1}(\mathbf{r}, t) \\
& - \frac{1}{2} \left[ \frac{(L + M + 2)(L + M + 1)}{(2L + 1)(2L + 3)} \right]^{1/2} \left( \frac{\partial}{\partial x} + i \frac{\partial}{\partial y} \right) v u_{L+1}^{M+1}(\mathbf{r}, t) \\
& + \frac{1}{2} \left[ \frac{(L - M - 1)(L - M)}{(2L + 1)(2L - 1)} \right]^{1/2} \left( \frac{\partial}{\partial x} + i \frac{\partial}{\partial y} \right) v u_{L-1}^{M+1}(\mathbf{r}, t) \\
& + \left[ \frac{(L + M + 1)(L - M + 1)}{(2L + 1)(2L + 3)} \right]^{1/2} \frac{\partial}{\partial z} v u_{L+1}^M(\mathbf{r}, t) \\
& + \left[ \frac{(L - M)(L + M)}{(2L - 1)(2L + 1)} \right]^{1/2} \frac{\partial}{\partial z} v u_{L-1}^M(\mathbf{r}, t) = q_{LM}(\mathbf{r}, t). \quad (7.13)
\end{aligned}$$

### 7.3.3 THE $P_N$ APPROXIMATION

The expansion of the BTE into spherical harmonics has led to an infinite set of equations with indices  $L$  (ranging from 0 to  $\infty$ ) and  $M$  (ranging from  $-L$  to  $L$ ). Truncation of the Laplace series at  $L = N$ , leads to the so-called  $P_N$  approximation. The reason for this name is that the last term in the truncated Laplace series contains  $Y_N^M(\hat{\Omega})$  which can be written in terms of the associated Legendre functions  $P_N^M(x)$ , which in turn can be written in terms of the Legendre polynomial  $P_N(x)$ . The relationships are the following:

$$Y_N^M(\hat{\Omega}) = (-1)^M \left[ \frac{(2N + 1)(N - M)!}{4\pi(N + M)!} \right]^{1/2} P_N^M(\cos \theta) e^{iM\phi}, \quad (7.14)$$

$$P_N^M(x) = (1 - x^2)^{M/2} \frac{d^M}{dx^M} P_N(x). \quad (7.15)$$

### 7.3.4 THE $P_1$ APPROXIMATION

We now consider the  $P_1$  approximation, which is often used to describe photon migration in tissues. In the  $P_1$  approximation  $u_{LM}(\mathbf{r}, t)$  is set to 0 for  $L > 1$ . In the  $P_1$  approximation, Eq. (7.13) is a set of four equations. The first, for  $L = 0$ ,  $M = 0$ :

$$\begin{aligned}
& \frac{\partial}{\partial t} u_{0,0}(\mathbf{r}, t) + v[\mu_s(1 - f_0) + \mu_a] u_{0,0}(\mathbf{r}, t) + \frac{1}{2} \sqrt{\frac{2}{3}} \left( \frac{\partial}{\partial x} - i \frac{\partial}{\partial y} \right) v u_{1,-1}(\mathbf{r}, t) \\
& - \frac{1}{2} \sqrt{\frac{2}{3}} \left( \frac{\partial}{\partial x} + i \frac{\partial}{\partial y} \right) v u_{1,1}(\mathbf{r}, t) + \sqrt{\frac{1}{3}} \frac{\partial}{\partial z} v u_{1,0}(\mathbf{r}, t) = q_{0,0}(\mathbf{r}, t); \quad (7.16)
\end{aligned}$$

$$\begin{aligned}
&= \sqrt{\frac{4\pi}{3}} v \left[ \sqrt{\frac{1}{2}} (-u_{1,1}(\mathbf{r}, t) + u_{1,-1}(\mathbf{r}, t)) \hat{\mathbf{x}} \right. \\
&\quad \left. - i \sqrt{\frac{1}{2}} (u_{1,1}(\mathbf{r}, t) + u_{1,-1}(\mathbf{r}, t)) \hat{\mathbf{y}} + u_{1,0}(\mathbf{r}, t) \hat{\mathbf{z}} \right]. \quad (7.21)
\end{aligned}$$

The set of four Eqs. (7.16)–(7.19) of the  $P_1$  approximation are thus equivalent to the following two equations (one scalar and one vectorial):

$$\frac{\partial}{\partial t} U(\mathbf{r}, t) + v [\mu_s(1 - f_0) + \mu_a] U(\mathbf{r}, t) + \nabla \cdot \mathbf{J}(\mathbf{r}, t) = \sqrt{4\pi} q_{0,0}(\mathbf{r}, t), \quad (7.22)$$

$$\begin{aligned}
&\frac{1}{v} \frac{\partial}{\partial t} \mathbf{J}(\mathbf{r}, t) + [\mu_s(1 - f_1) + \mu_a] \mathbf{J}(\mathbf{r}, t) + \frac{1}{3} v \nabla U(\mathbf{r}, t) \\
&= \sqrt{\frac{4\pi}{3}} \left[ \sqrt{\frac{1}{2}} (q_{1,-1}(\mathbf{r}, t) - q_{1,1}(\mathbf{r}, t)) \hat{\mathbf{x}} \right. \\
&\quad \left. - i \sqrt{\frac{1}{2}} (q_{1,-1}(\mathbf{r}, t) + q_{1,1}(\mathbf{r}, t)) \hat{\mathbf{y}} + q_{1,0}(\mathbf{r}, t) \hat{\mathbf{z}} \right]. \quad (7.23)
\end{aligned}$$

The vectorial equation is obtained by combining Eqs. (7.17), (7.18), (7.19) according to the following formal relationship:

$$\sqrt{2\pi/3}[(7.17) - (7.19)]\hat{\mathbf{x}} - i\sqrt{2\pi/3}[(7.17) + (7.19)]\hat{\mathbf{y}} + \sqrt{4\pi/3}(7.18)\hat{\mathbf{z}}.$$

From the general definition of the coefficients  $f_l$ , we find that  $f_0$  and  $f_1$  are given by

$$f_0 = 2\pi \int_{-1}^1 f(\cos \gamma) P_0(\cos \gamma) d(\cos \gamma) = 2\pi \int_{-1}^1 f(\cos \gamma) d(\cos \gamma) = 1, \quad (7.24)$$

$$\begin{aligned}
f_1 &= 2\pi \int_{-1}^1 f(\cos \gamma) P_1(\cos \gamma) d(\cos \gamma) \\
&= 2\pi \int_{-1}^1 f(\cos \gamma) \cos \gamma d(\cos \gamma) = \langle \cos \gamma \rangle, \quad (7.25)
\end{aligned}$$

where in Eq. (7.24) we have used the fact that the scattering probability is normalized according to the condition  $\int_{4\pi} f(\hat{\Omega}' \cdot \hat{\Omega}) d\hat{\Omega}' = 1$ , which is equivalent to  $2\pi \int_{-1}^1 f(\cos \gamma) d(\cos \gamma) = 1$ . Therefore  $f_0$  is 1, whereas  $f_1$  is the average cosine of the scattering angle  $\gamma$  ( $\langle \cos \gamma \rangle$ ). The source terms in Eqs. (7.22) and (7.23) are formally a monopole term (spherically symmetric) and a dipole term, respectively.

The average values of the coordinates of  $P_3$  are<sup>32</sup>

$$\begin{aligned}\langle x_3 \rangle &= \langle y_3 \rangle = 0, \\ \langle z_3 \rangle &= \frac{1}{\mu_s} (1 + \langle \cos \theta \rangle + \langle \cos \theta \rangle^2).\end{aligned}\tag{7.31}$$

In general, at the  $n$ -th order of scattering, the average values of the coordinates of the scattering point  $P_n$  are<sup>32</sup>

$$\begin{aligned}\langle x_n \rangle &= \langle y_n \rangle = 0, \\ \langle z_n \rangle &= \frac{1}{\mu_s} \sum_{k=0}^{n-1} \langle \cos \gamma \rangle^k = \frac{1 - \langle \cos \gamma \rangle^n}{\mu_s (1 - \langle \cos \gamma \rangle)},\end{aligned}\tag{7.32}$$

where we have used the result for the geometric series  $\sum_{k=0}^{n-1} a^k = (1 - a^n)/(1 - a)$ , with  $a < 1$ . In the limit of a high number of scattering events ( $n \rightarrow \infty$ ),  $\langle x_\infty \rangle = \langle y_\infty \rangle = 0$  and  $\langle z_\infty \rangle = 1/[\mu_s(1 - \langle \cos \gamma \rangle)]$  give the coordinates of the center of symmetry of the statistical photon distribution. In particular, the coordinate  $\langle z_\infty \rangle$  can be interpreted as the average distance between consecutive, effectively isotropic scattering events, and its inverse is defined as the reduced scattering coefficient  $\mu'_s$ :

$$\mu'_s = \mu_s (1 - \langle \cos \gamma \rangle).\tag{7.33}$$

In the case of isotropic scattering,  $\langle \cos \gamma \rangle = 0$  and  $\mu'_s = \mu_s$ . In the case of forward scattering,  $\langle \cos \gamma \rangle = 1$  and  $\mu'_s = 0$ .

### 7.3.6 THE $P_1$ EQUATION AND THE STANDARD DIFFUSION EQUATION (SDE)

We now reduce the  $P_1$  approximation to a single equation for the photon density  $U(\mathbf{r}, t)$ . From Eq. (7.27) we obtain  $\mathbf{J}(\mathbf{r}, t)$ :

$$\begin{aligned}\mathbf{J}(\mathbf{r}, t) &= -\frac{1}{v(\mu'_s + \mu_a)} \frac{\partial}{\partial t} \mathbf{J}(\mathbf{r}, t) - \frac{v}{3(\mu'_s + \mu_a)} \nabla U(\mathbf{r}, t) + \frac{1}{(\mu'_s + \mu_a)} \mathbf{S}_1(\mathbf{r}, t) \\ &= -\frac{3D}{v^2} \frac{\partial}{\partial t} \mathbf{J}(\mathbf{r}, t) - D \nabla U(\mathbf{r}, t) + \frac{3D}{v} \mathbf{S}_1(\mathbf{r}, t),\end{aligned}\tag{7.34}$$

where we have defined the diffusion coefficient  $D = v/[3(\mu'_s + \mu_a)]$ . By substituting this expression for  $\mathbf{J}(\mathbf{r}, t)$  in Eq. (7.26), we get

$$\begin{aligned}\frac{\partial}{\partial t} U(\mathbf{r}, t) + v\mu_a U(\mathbf{r}, t) - \frac{3D}{v^2} \frac{\partial}{\partial t} \nabla \cdot \mathbf{J}(\mathbf{r}, t) - D \nabla^2 U(\mathbf{r}, t) \\ + \frac{3D}{v} \nabla \cdot \mathbf{S}_1(\mathbf{r}, t) = S_0(\mathbf{r}, t).\end{aligned}\tag{7.35}$$

and the photon flux  $\mathbf{J}(\mathbf{r}, t)$  is related to the photon density  $U(\mathbf{r}, t)$  by Fick's law:

$$\mathbf{J}(\mathbf{r}, t) = -D\nabla U(\mathbf{r}, t). \quad (7.40)$$

In the frequency domain,  $\partial/\partial t \rightarrow -i\omega$  and the diffusion equation takes the form of the Helmholtz equation:

$$(\nabla^2 + k^2)U(\mathbf{r}) = -\frac{S_0(\mathbf{r})}{D}, \quad (7.41)$$

where  $k^2 = (i\omega - v\mu_a)/D$ .

### 7.3.7 SOLUTION OF THE STANDARD DIFFUSION EQUATION IN THE FREQUENCY DOMAIN

The solution to the diffusion equation for a homogeneous, infinite medium containing a harmonically modulated point source of power  $P(\omega)$  at  $\mathbf{r} = 0$  is given by<sup>33</sup>

$$U(r, \omega) = \frac{P(\omega)}{4\pi D} \frac{e^{ikr}}{r}. \quad (7.42)$$

The explicit expressions for the average photon density ( $U_{DC}$ ), and for the amplitude ( $U_{AC}$ ) and phase ( $\Phi$ ) of the photon-density wave are<sup>25,34,35</sup>

$$U_{DC}(r) = \frac{P_{DC}}{4\pi D} \frac{e^{-r(v\mu_a/D)^{1/2}}}{r}, \quad (7.43)$$

$$U_{AC}(r, \omega) = \frac{P(\omega)}{4\pi D} \frac{e^{-r(v\mu_a/2D)^{1/2}[(1 + \frac{\omega^2}{v^2\mu_a^2})^{1/2} + 1]^{1/2}}}{r}, \quad (7.44)$$

$$\Phi(r, \omega) = r(v\mu_a/2D)^{1/2} \left[ \left( 1 + \frac{\omega^2}{v^2\mu_a^2} \right)^{1/2} - 1 \right]^{1/2} + \Phi_s, \quad (7.45)$$

where  $\Phi_s$  is the source phase in radians. Analytical solutions in the frequency domain have also been reported for a semi-infinite medium,<sup>25,35,36</sup> infinite slab,<sup>37</sup> cylindrical, and spherical geometries.<sup>37</sup> Equations (7.39) and (7.41) refer to homogeneous media. For quantitative tissue spectroscopy and oximetry (Section 7.4), one typically assumes that tissues are macroscopically homogeneous, so that Eqs. (7.39) and (7.41) are applicable. By contrast, optical imaging of tissues (Section 7.5) aims at measuring the spatial distribution of the tissue optical properties, and Eq. (7.39) must be generalized to account for the spatial dependence of  $\mu_a$  and  $D$ .



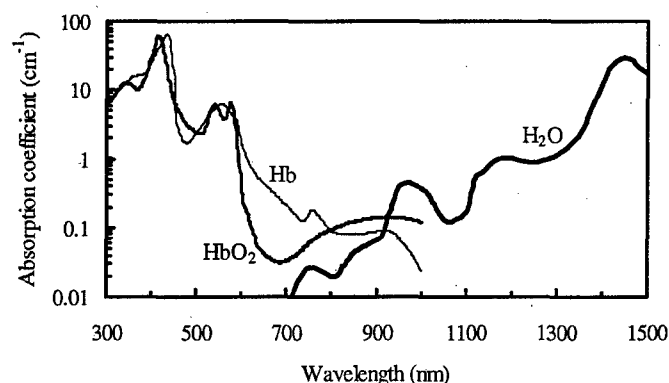


**Figure 7.4** Absorption spectra of the three dominant near-infrared chromophores in tissues, namely oxy-hemoglobin ( $\text{HbO}_2$ ), deoxy-hemoglobin ( $\text{Hb}$ ), and water ( $\text{H}_2\text{O}$ ). The absorption coefficient is defined to base  $e$ . The concentrations of  $\text{Hb}$  and  $\text{HbO}_2$  are both assumed to be  $50 \mu\text{M}$ , a typical value for blood-perfused tissues. These spectra are obtained from compiled absorption data for water<sup>42</sup> and hemoglobin.<sup>43</sup>

by a photon before being absorbed. In the NIR, typical values of  $\mu_a$  in tissues range from  $0.02$  to  $0.30 \text{ cm}^{-1}$ . The photon mean free path for absorption thus ranges between about  $3$  and  $50 \text{ cm}$ .

#### 7.4.1.2 Scattering

The scattering properties are determined mainly by the size of the scattering particles relative to the wavelength of light, and by the refractive index mismatch between the scattering particles and the surrounding medium. In biological tissues, the scattering centers are cells and cellular organelles. In the medical spectral window ( $700$ – $900 \text{ nm}$ ), cellular organelles have dimensions comparable to the wavelength, and their index of refraction is relatively close to that of the cytosol and extracellular fluid. As a result, light scattering in tissue is mainly forward directed (i.e., the scattering angle  $\gamma$  introduced in Section 7.3.2 is less than  $90^\circ$ ) and shows a weak wavelength dependence.

As discussed in Sections 7.3.1 and 7.3.5, the scattering properties of tissues are described by two parameters: (1) the scattering coefficient ( $\mu_s$ ), defined as the inverse of the average photon path length between successive scattering events; and (2) the average cosine of the scattering angle ( $f_1 = \langle \cos \gamma \rangle$ ). From the definition of  $\mu_s$ , it follows that  $1/\mu_s$  is the average distance traveled by a photon between successive scattering events, as shown by Eq. (7.28). Even though each scattering event is mainly forward directed, after a number of collisions a photon loses memory of its original direction of propagation. Under these conditions, we can say that the photon has experienced an effectively isotropic scattering event. As discussed in Section 7.3.5, the reduced scattering coefficient [ $\mu'_s = (1 - f_1)\mu_s$ ] represents

If the extinction spectra  $\epsilon_i(\lambda)$  of all  $N$  species are known, the concentrations  $C_i$  can be determined by measuring  $\mu_a$  at  $N$  or more wavelengths, so that the linear system of Eq. (7.46) is fully determined. This approach requires that  $\mu_a$  be measured independently of  $\mu'_s$ . In the frequency domain, Eqs. (7.43)–(7.45), or the corresponding equations for semi-infinite or other geometries, can be used to quantitatively measure  $\mu_a$  and  $\mu'_s$ .<sup>36</sup> The spatial<sup>10</sup> or the frequency<sup>17</sup> dependence of the DC intensity, AC amplitude, and phase can also be used effectively for *in-vivo* tissue spectroscopy. It is worth noting that this approach to tissue spectroscopy yields quantitative, absolute values of the concentration of chromophores in tissue.

### 7.4.3 NEAR-INFRARED TISSUE OXIMETRY

In many cases, the absorption spectra of tissues can be well described by considering only three chromophores; namely, oxy-hemoglobin, deoxy-hemoglobin, and water. For example, Figure 7.5 shows the absorption coefficients of human muscle (forearm) and brain (forehead) measured at eight NIR wavelengths (squares) under resting conditions. The lines in Figure 7.5 are the best fit absorption spectra corresponding to a linear combination of the water, oxy-hemoglobin, and deoxy-hemoglobin extinction spectra. In the fits, the water concentration (by volume) is assumed to be 75% for the muscle, and 80% for the brain,<sup>45</sup> while the concentrations of oxy-hemoglobin ( $[\text{HbO}_2]$ ) and deoxy-hemoglobin ( $[\text{Hb}]$ ) are the parameters for fit. The best fit spectra of Figure 7.5 yield values of  $[\text{HbO}_2]$  and  $[\text{Hb}]$  of

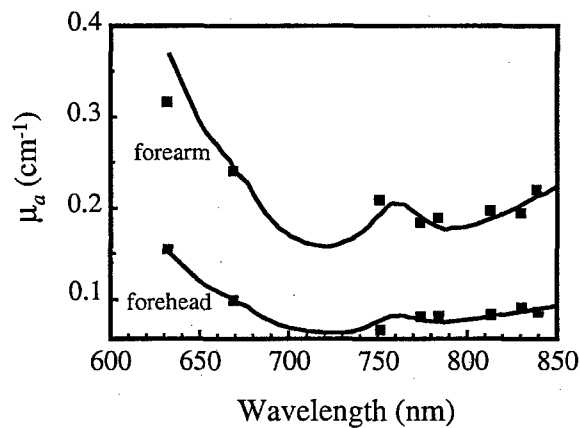


**Figure 7.5** Quantitative absorption spectroscopy of tissues *in vivo*.<sup>24,46</sup> The squares represent the eight-wavelength spectra measured with frequency-domain spectroscopy in the skeletal muscle and in the forehead (according to the label) of human subjects. The lines are best fits using a linear combination of the extinction spectra of oxy-hemoglobin, deoxy-hemoglobin, and water.

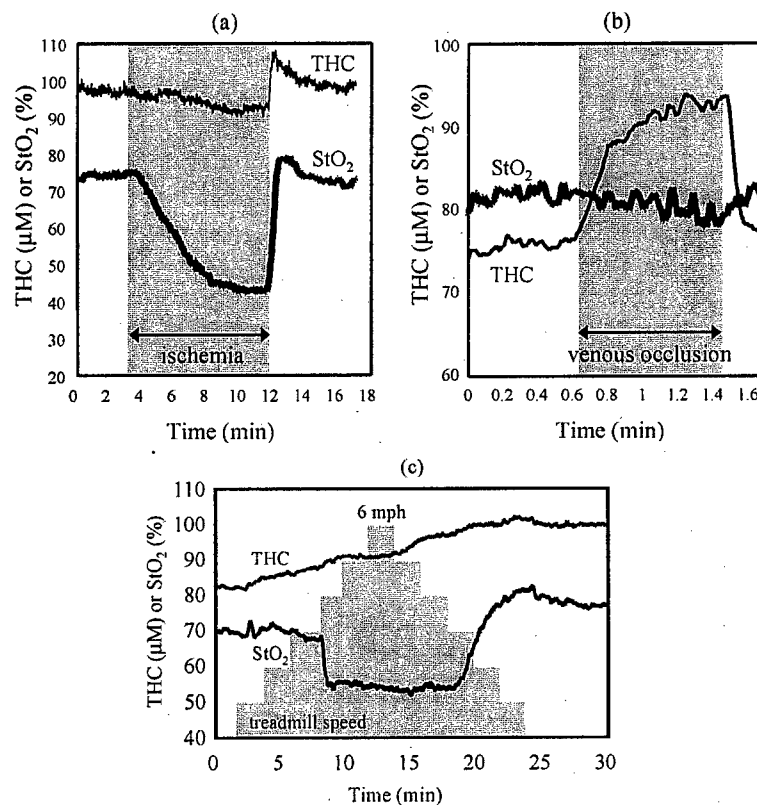


**Figure 7.6** Temporal traces of optically measured total hemoglobin concentration ( $\text{THC} = [\text{HbO}_2] + [\text{Hb}]$ ) and tissue saturation ( $\text{StO}_2$ ) in human subjects. The measurements were conducted on a forearm muscle during (a) arterial or (b) venous occlusion, and (c) on a calf muscle during treadmill exercise. In panel (c), the step function represent the treadmill speed, which was changed by steps of 1 mph every 2 minutes.<sup>50</sup> Running started at a speed of 4 mph. The frequency-domain measurements allow for absolute y-axis readings

Near-infrared oximetry lends itself to measurements on the human head as well. Figure 7.7a shows the arrangement of optical fibers on the forehead of a human subject. The cerebral oxygenation may be varied by changing the fraction of oxygen inspired by the subject. The resulting changes in the cerebral tissue oxygenation ( $\text{StO}_2$ ) are reported in Figure 7.7b. Figure 7.7b also shows a comparison between two traces of arterial saturation ( $\text{SaO}_2$ ); one is measured with a commercial pulse oximeter, while the other is measured with a frequency-domain tissue oximeter.<sup>46</sup> Both instruments use the oscillatory components of the optical signals at the frequency of the heartbeat (which are directly associated with the arterial pulsation, and therefore with arterial blood volume). The key differ-

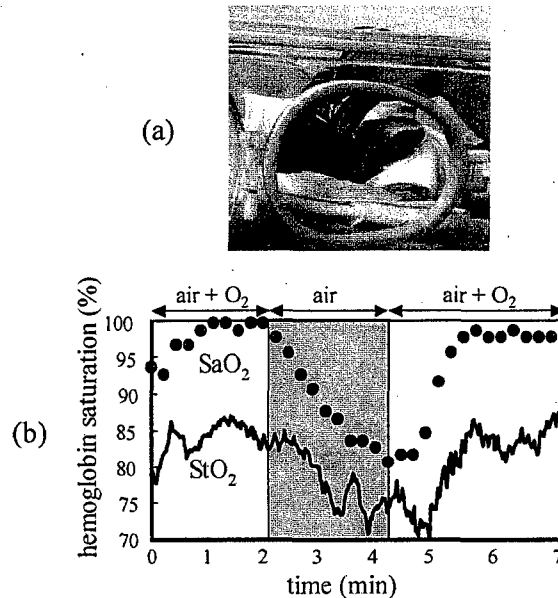


**Figure 7.8** Frequency-domain, near-infrared oximetry of the newborn infant brain. (a) Photograph showing the application of a flexible optical probe to the infant's head. (b) Temporal traces of cerebral tissue saturation ( $StO_2$ ) measured with frequency-domain optical oximetry, and systemic arterial saturation ( $SaO_2$ ) measured with a pulse oximeter at an infant's toe. Deoxygenation is achieved by a controlled reduction in the fraction of inspired oxygen (in collaboration with G. P. Donzelli and S. Pratesi, University of Florence, Italy).

duced by a controlled decrease in the fraction of inspired oxygen. The arterial saturation and the cerebral saturation show a qualitatively similar trend. However, a local cerebral deoxygenation would be detected only by the NIR cerebral measurement. The manual application of the optical probe shown in Figure 7.8a can be replaced by a flexible headband<sup>57,58</sup> or by an infant cap for continuous long-term monitoring.

#### 7.4.4 MEASUREMENTS OF OPTICAL SCATTERING IN TISSUES

Traditionally, optical studies have been targeted at measurements of the absorption properties of tissues. The strong scattering of light in tissue constitutes a complication in quantitative absorption spectroscopy. However, it has recently been suggested that the reduced scattering coefficient itself may provide information about physiologically relevant parameters. For instance, it has been shown that mitochondria are the main source of light scattering in the liver, and possibly in other tissues as well.<sup>59</sup> Since a number of metabolic processes related to cellular

effects. Theoretical and experimental studies of the optical properties of the human sclera (the white outer coat enclosing the eyeball) have also shown a significant scattering change induced by glucose and by other osmotically active species.<sup>63</sup> While the monitoring of glucose concentration by NIR spectroscopy is, at the present stage of development, far from being clinically applicable, it nevertheless points out the diversity of potential diagnostic applications of medical optics.

## 7.5 OPTICAL IMAGING OF TISSUES

### 7.5.1 GENERAL CONCEPTS

Optical imaging relies on its sensitivity to optical properties of tissues, namely absorption and scattering. Consequently, the contrast in NIR imaging originates from spatial variations in the optical absorption and scattering properties of the tissue. These spatial variations can be due to a local change in hemoglobin concentration or saturation (for instance, a hematoma or heterogeneous vascularization, blood flow, or oxygenation), a localized change in the tissue architecture (for example, a result of microcalcifications), or the concentration of cellular organelles. In any case, NIR imaging is sensitive to physical properties of tissues that are different than those probed by current diagnostic imaging modalities such as x-ray tomography (mass density, atomic number), ultrasound (acoustic impedance), magnetic resonance imaging (proton density, nuclear relaxation times), and positron emission tomography (accumulation of a radioactive tracer). In this sense, NIR imaging is not necessarily an alternative to these imaging modalities but could constitute an adjunct technique that complements existing methods. We point out here that the promise of optical tomography is not in achieving a high spatial resolution (which is intrinsically limited by the diffusive nature of light propagation in tissues), but rather in achieving high contrast and specificity.

NIR tissue imaging aims at generating spatial maps that display either structural or functional properties of tissues. Since optical imaging studies the spatial distribution of the optical properties, Eq. (7.39) must be replaced with the diffusion equation for inhomogeneous media:

$$\frac{\partial U(\mathbf{r}, t)}{\partial t} - \nabla \cdot D(\mathbf{r}) \nabla U(\mathbf{r}, t) + v\mu_a(\mathbf{r})U(\mathbf{r}, t) = q(\mathbf{r}, t). \quad (7.47)$$

Equation (7.47) can be used to solve the forward problem, which consists of finding the photon density  $U(\mathbf{r}, t)$  corresponding to a given spatial distribution of the optical properties and of the photon sources. Analytical solutions of Eq. (7.47) are available only for a few inhomogeneous cases such as those of spherical<sup>33</sup> and cylindrical<sup>64</sup> inclusions. For arbitrary inhomogeneous cases, Eq. (7.47) can be solved using numerical methods such as the finite-difference method (FDM)<sup>65</sup> or the finite-element method (FEM).<sup>66</sup> Alternatively, a perturbation expansion in  $\mu_a$  and  $D$  leads to a solution of Eq. (7.47) in terms of a volume integral involving

Another approach, using a hybrid of CW and frequency-domain techniques has been employed to perform real-time imaging (image acquisition rate: 5.2 Hz) of an experimental brain hemorrhage in a piglet model.<sup>85</sup> Figure 7.10 shows the optical image recorded noninvasively through the intact scalp and skull immediately following the subcortical injection (depth of injection: 1.2 cm) of 0.5 cc of autologous blood. In Figure 7.10, a photograph of a brain slice obtained after autopsy is superimposed to the near-infrared image to show the geometrical relationship between the optical image and the piglet brain. The optical image was obtained by linearly combining the readings from 10 source-detector pairs according to a linear back-projection scheme.<sup>85</sup> While this scheme is computationally fast, it does not lead to quantitative readings, so that the absorption scale in Figure 7.10 is qualitative (i.e., the image gives reliable spatially resolved information on whether the absorption increases or decreases, but the absorption changes are not accurately

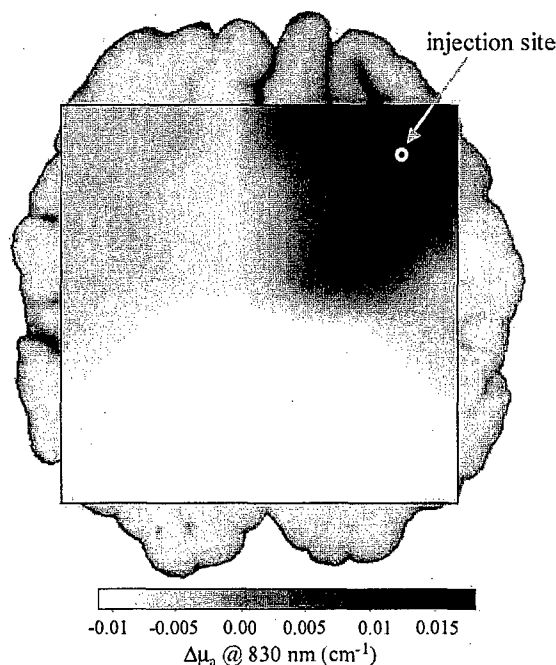


**Figure 7.10** Optical absorption image of a  $4 \times 4 \text{ cm}^2$  area of the piglet brain, measured non-invasively immediately after the subcortical injection of 0.5 cc of blood.<sup>85</sup> The injection site is indicated by the white circle. A picture of a brain slice taken after autopsy is superimposed to the optical image to show the geometrical relationship between the imaged area and the piglet brain. One can see the increased optical absorption over the area surrounding the injection site, which corresponds to the subcortical hemorrhage.

<30 s,<sup>98</sup> 2.5 min,<sup>99</sup> several hours,<sup>57,58</sup> and not-quantified "slow data acquisition rate"<sup>100</sup> and "long measurement times."<sup>94</sup> Faster optical imaging approaches, suitable for noninvasive functional brain imaging, have been reported recently with image acquisition times of 500 ms<sup>101</sup> and 160 ms.<sup>79</sup> Noninvasive optical studies of the brain are reviewed in Ref. [102].

Figure 7.11 shows the results of a functional brain imaging study that used a multichannel frequency-domain optical instrument (a modified version of Model No. 96208, ISS, Inc., Champaign, IL, shown in Figure 7.2).<sup>79</sup> The optically measured maps of cerebral deoxy-hemoglobin concentration show the activated cortical area during voluntary hand tapping. Image reconstruction was based on a linear superposition of the optical signals from 10 source-detector pairs. The fast image acquisition rate (6.25 Hz) leads to online, continuous optical mapping of the cerebral cortex during the examination. Figure 7.11 shows one optical image every 10 measurements (i.e., every 1.6 s) for space reasons. The real-time movie of the cerebral activation recorded with near-infrared imaging can be viewed in Ref. [79].

Currently, most optical functional studies of the brain have been based on continuous-wave (cw) spectroscopy. Even Figure 7.11 shows results based on the DC component of the measured amplitude-modulated signal. The reason for the more common use of cw data in optical brain imaging is twofold. (1) The study of cerebral activation requires the measurement of changes in the optical signals that correlate with brain activity. Therefore, even relative readings, i.e., changes from an arbitrary initial value, yield meaningful information. (2) The absolute measurement capability afforded by time-resolved methods requires the application of a physical model for light propagation inside tissues. An accurate model for the highly inhomogeneous and geometrically irregular case of the human head is yet to be achieved. However, there are a few exceptions to the use of cw spectroscopy for optical studies of the brain.<sup>98,99,103,104</sup> These studies show that even without absolute measurements, time-resolved data can be extremely valuable in optical studies of the human brain. In fact, the additional information content of time-resolved data (the phase in the frequency-domain, the time-of-flight distribution in the time-domain) may lead to more effective approaches to human brain studies, for instance by affording the optimization of the spatial region of sensitivity, and the maximization of the sensitivity to localized absorption and scattering changes.

### 7.5.3 OPTICAL MAMMOGRAPHY

From a practical point of view, the human breast lends itself to near-infrared tissue spectroscopy and imaging. In fact, it is easily accessible and its relatively low hemoglobin concentration (10–20  $\mu\text{M}$ )<sup>105,106</sup> determines near-infrared absorption coefficients ( $\sim 0.02\text{--}0.04\text{ cm}^{-1}$ ) that account for a deep optical penetration depth and the optical transmission through the whole breast. Furthermore, there is much appeal in the possibility of detecting breast cancer using a noninvasive method that

does not involve ionizing radiation. The optical detection of breast cancer may rely on the perturbations induced by cancer on the host tissue rather than on a direct detection of optical signatures associated with cancer cells.<sup>107</sup> These perturbations include angiogenesis,<sup>107,108</sup> alterations to the blood flow and oxygenation,<sup>108</sup> and fibroblast proliferation,<sup>107</sup> which may yield modifications to the optical scattering and absorption properties. However, it is not known whether these cancer-induced optical perturbations can lead to an effective optical approach to breast cancer detection over the wide range of cases observed in the clinical and screening practice (different types and stages of cancer, various benign tumors, different levels of tissue heterogeneity, etc.). *In vitro* optical studies of normal and diseased breast tissues have not found significant differences between their optical properties.<sup>109,110</sup> This result further suggests that the optical contrast induced by cancer may result only from modifications to the vascularization, oxygenation, or tissue architecture, which are significantly altered for the measurements *in vitro*. In fact, *in-vivo* measurements have indicated that cancerous breast tissue has a significantly larger absorption coefficient and a marginally larger reduced scattering coefficient with respect to normal breast tissue.<sup>111-113</sup> Since it is yet to be demonstrated that optical mammography can rely solely on the intrinsic optical contrast associated with cancer, it has recently been proposed to use dyes as optical contrast agents.<sup>73,114,115</sup>

The first clinical tests of breast transillumination for diagnostic purposes were performed by Cutler in 1929.<sup>116</sup> This approach was soon abandoned because of the poor sensitivity and specificity of the method. In the 1970s and 1980s, technical developments led to two new optical techniques called *diaphanography*<sup>117</sup> and *lightscanning*,<sup>118</sup> which induced a renewed enthusiasm for optical mammography. These approaches employed a broad beam of visible and NIR continuous-wave light that illuminated one side of the breast. On the opposite side of the breast, the examiner visually inspected the light transmission pattern and used a video camera for image recording. The examination had to be performed in a dark room, and the examiner's eyes needed to be dark-adapted. Despite some encouraging initial results,<sup>119</sup> several clinical studies conducted in the late 1980s have shown that diaphanography and lightscanning are inferior to x-ray mammography both as a screening and as a clinical tool.<sup>120,121</sup> As a result, medical acceptance of diaphanography and lightscanning has been subdued.

The introduction of time-resolved methods for tissue imaging has yielded new instrumental tools for optical mammography. Furthermore, the application of the diffusion equation [Eq. (7.47)] provides a mathematical model that allows for a more rigorous approach to optical mammography with respect to the mainly empirical studies of the past. As a result, new time-domain<sup>73,112,122-124</sup> and frequency-domain<sup>18,105,113,125-128</sup> approaches for optical mammography have recently been developed. Siemens AG, Medical Engineering (Erlangen, Germany) has recently designed and clinically tested a frequency-domain prototype for optical mammography.<sup>129</sup> Figure 7.12 shows a block diagram of this prototype and two representative optical mammograms obtained on a patient affected by breast cancer. The optical mammograms shown in Figure 7.12 are 2D projection images



by minimizing the effects of the breast geometry on the optical data.<sup>80</sup> As in x-ray mammography, the breast is imaged in two directions, leading to a craniocaudal (cc) and an oblique (ob) view. Figure 7.12 shows that breast cancer can be detected with excellent contrast using optical methods. However, optical mammography still needs to improve its performance in the detection of small tumors and in the discrimination between malignant tumors and benign breast lesions. A preliminary analysis based on the criterion that an optical mammogram is positive if it shows a region of abnormal absorbance in both the craniocaudal and oblique views, has led to a sensitivity (fraction of cancerous breasts successfully detected) of 72% and a specificity (fraction of noncancerous breasts correctly evaluated as negative) of 52% on a clinical population of 131 patients.<sup>130</sup> This result is consistent with the sensitivity of 73% obtained on 69 patients<sup>131</sup> with a similar frequency-domain prototype developed independently by the research laboratories of Carl Zeiss (Oberkochen, Germany).<sup>132</sup> It must be stressed that these results, which are based on optical mammograms like the ones shown in Figure 7.12b, rely on 2D projection data at a single wavelength. The potential of optical mammography goes beyond these capabilities, so that there are a number of possibilities for developing more effective approaches. For instance, testing nonplanar geometries without (or with minimal) breast compression, exploiting the spectral information, quantifying and discriminating the breast absorption and scattering coefficients, achieving a true 2D or 3D spatial reconstruction of the breast optical properties, performing oxygenation or blood flow imaging, and developing imaging approaches based on dynamic perturbations (such as periodic light compression and decompression of the breast), are some of the areas currently under investigation by research groups worldwide.

## 7.6 FUTURE DIRECTIONS

The key difference between continuous-wave and frequency-domain spectroscopy is the phase measurement capability afforded by the frequency-domain. For optical studies of tissues, the phase information can be exploited in at least two ways.

First, by combining the phase measurement with the DC intensity, AC amplitude, or modulation measurement, one can separately measure the absorption and the reduced scattering coefficients of tissues. This is of paramount importance for quantitative tissue spectroscopy, imaging, and oximetry. In this chapter, we have illustrated the capability of frequency-domain spectroscopy to quantify the absorption and the reduced scattering coefficients [Figures 7.3d, 7.5, and 7.9], and to perform absolute tissue oximetry (Figures 7.6–7.8).

The second relevant aspect of the phase measurement is that the phase is sensitive to a different tissue volume with respect to the DC intensity and AC amplitude. The region of sensitivity can be evaluated by the effect on the measured quantities of a small perfectly absorbing object located at  $\mathbf{r}$ . In particular, the DC, AC, and phase sensitivities can be expressed by the parameters  $e_{DC}(\mathbf{r}) = DC(\mathbf{r})/DC_0$ ,  $e_{AC}(\mathbf{r}) = AC(\mathbf{r})/AC_0$ , and  $e_{\Phi}(\mathbf{r}) = \Phi(\mathbf{r}) - \Phi_0$ , respectively, where  $DC_0$ ,  $AC_0$ ,  $\Phi_0$ ,

the figure caption).<sup>133</sup> Figure 7.13 shows that the DC and AC measurement are most sensitive to the region along the line joining the source and the detector, which, by contrast, is not the highest region of sensitivity for the phase. In a non-invasive tissue measurement, which is better modeled by a semi-infinite geometry, where the illuminating and collecting optical fibers are located on the tissue/air interface, the phase measurement is typically less sensitive to the superficial tissue layer with respect to the DC and AC measurements. As a result, the phase information may contribute to achieving depth discrimination in optical imaging of tissues.

Future applications of frequency-domain techniques to the optical study of biological tissues will exploit the two above-mentioned features, with the objective of developing innovative approaches for medical imaging and diagnosis.

#### ACKNOWLEDGMENTS

We thank E. Gratton, B. Barbieri, and D. Hueber for useful discussions, and E. Heffer for the critical reading of the manuscript. This research is supported by the U.S. National Institutes of Health (Grants No. CA57032 and MH62854) and by the U.S. Department of the Army (Award No. DAMD17-99-1-9218).

#### REFERENCES

1. D. T. Delpy, M. Cope, P. van der Zee, S. Arridge, S. Wray, and J. Wyatt, "Estimation of optical pathlength through tissue from direct time of flight measurement," *Phys. Med. Biol.* Vol. 33, pp. 1433-1442 (1988).
2. M. S. Patterson, B. Chance, and B. C. Wilson, "Time resolved reflectance and transmittance for the non-invasive measurement of optical properties," *Appl. Opt.* Vol. 28, pp. 2331-2336 (1989).
3. B. Chance, M. Cope, E. Gratton, N. Ramanujam, and B. Tromberg, "Phase measurement of light absorption and scatter in human tissue," *Rev. Sci. Instrum.* Vol. 69, pp. 3457-3481 (1998).
4. E. Gratton and M. Limkeman, "A continuously variable frequency-domain cross-correlation phase fluorometer with picosecond resolution," *Biophys. J.* Vol. 44, pp. 315-324 (1983).
5. R. D. Spencer and G. Weber, "Measurement of subnanosecond fluorescence lifetimes with a cross-correlation phase fluorometer," *Ann. NY Acad. Sci.* Vol. 158, pp. 361-376 (1969).
6. D. W. Piston, G. Marriott, T. Radivoyevich, R. Clegg, T. M. Jovin, and E. Gratton, "Wide-band acousto-optic light modulator for frequency-domain fluorometry and phosphorimetry," *Rev. Sci. Instrum.* Vol. 60, pp. 2596-2600 (1989).

21. B. A. Feddersen, D. W. Piston, and E. Gratton, "Digital parallel acquisition in frequency domain fluorometry," *Rev. Sci. Instrum.* Vol. 60, pp. 2929–2936 (1989).
22. R. N. Bracewell, *The Fourier Transform and Its Applications*, pp. 189–194, McGraw-Hill, Singapore (1986).
23. S. Fantini, M. A. Franceschini, J. S. Maier, S. A. Walker, B. Barbieri, and E. Gratton, "Frequency-domain multichannel optical detector for non-invasive tissue spectroscopy and oximetry," *Opt. Eng.* Vol. 34, pp. 32–42 (1995).
24. M. A. Franceschini, E. Gratton, D. Hueber, and S. Fantini, "Near-infrared absorption and scattering spectra of tissues *in vivo*," *Proc. SPIE* Vol. 3597, pp. 526–531 (1999).
25. S. Fantini, M. A. Franceschini, and E. Gratton, "Semi-infinite-geometry boundary problem for light migration in highly scattering media: a frequency-domain study in the diffusion approximation," *J. Opt. Soc. Am. B* Vol. 11, pp. 2128–2138 (1994).
26. J. J. Duderstadt and L. J. Hamilton, *Nuclear Reactor Analysis*, p. 113, Wiley, New York, NY (1976).
27. F. Hetzel, M. Patterson, L. Preuss, and B. Wilson, "Recommended nomenclature for physical quantities in medical applications of light," AAPM Report No. 57, American Institute of Physics, Woodbury, NY, pp. 1–6 (1996).
28. J.-M. Kaltenbach and M. Kaschke, "Frequency- and time-domain modelling of light transport in random media," in *Medical Optical Tomography: Functional Imaging and Monitoring*, G. J. Muller et al. (eds.), pp. 65–86, SPIE, Bellingham, Washington (1993).
29. D. A. Boas, "Diffuse Photon Probes of Structural and Dynamical Properties of Turbid Media: Theory and Biomedical Applications," Ph.D. Thesis, Dept. of Physics, University of Pennsylvania, (1996).
30. S. R. Arridge, "Optical tomography in medical imaging," *Inverse Problems* Vol. 15, pp. R41–R93 (1999).
31. H. W. Wyld, *Mathematical Methods for Physics*, Chapter 3, Addison-Wesley, Reading, MA (1994).
32. G. Zaccanti, E. Battistelli, P. Bruscaglioni, and Q. Wei, "Analytic relationships for the statistical moments of scattering point coordinates for photon migration in a scattering medium," *Pure Appl. Opt.* Vol. 3, pp. 897–905 (1994).
33. D. A. Boas, M. A. O'Leary, B. Chance, and A. G. Yodh, "Scattering of diffuse photon density waves by spherical inhomogeneities within turbid media: analytic solution and applications," *Proc. Natl. Acad. Sci. USA* Vol. 91, pp. 4887–4891 (1994).
34. J. B. Fishkin and E. Gratton, "Propagation of photon-density waves in strongly scattering media containing an absorbing semi-infinite plane bounded by a straight edge," *J. Opt. Soc. Am. A* Vol. 10, pp. 127–140 (1993).

50. V. Quaresima, M. A. Franceschini, S. Fantini, E. Gratton, and M. Ferrari, "Difference in leg muscles oxygenation during treadmill exercise by a new near infrared frequency-domain oximeter," in *Photon Propagation in Tissues III*, D. A. Benaron, B. Chance, M. Ferrari (eds.), *Proc. SPIE* Vol. 3194, pp. 116–120 (1998).
51. T. R. Cheatle, L. A. Potter, M. Cope, D. T. Delpy, P. D. Coleridge Smith, and J. H. Scurr, "Near-infrared spectroscopy in peripheral vascular disease," *Br. J. Surg.* Vol. 78, pp. 405–408 (1991).
52. R. A. de Blasi, M. Cope, and M. Ferrari, "Oxygen consumption of human skeletal muscle by near-infrared spectroscopy during tourniquet-induced ischemia in maximal voluntary contraction," *Adv. Exp. Med. Biol.* Vol. 317, pp. 771–777 (1992).
53. R. A. de Blasi, M. Ferrari, A. Natali, G. Conti, A. Mega, and A. Gasparetto, "Noninvasive measurement of forearm blood flow and oxygen consumption by near-infrared spectroscopy," *J. Appl. Physiol.* Vol. 76, pp. 1388–1393 (1994).
54. S. Homma, H. Eda, S. Ogasawara, and A. Kagaya, "Near-infrared estimation of  $O_2$  supply and consumption in forearm muscles working at varying intensity," *J. Appl. Physiol.* Vol. 80, pp. 1279–1284 (1996).
55. M. C. P. van Beekvelt, W. N. J. M. Colier, B. G. M. van Engelen, M. T. E. Hopman, R. A. Wevers, and B. Oeseburg, "Validation of measurement protocols to assess oxygen consumption and blood flow in the human forearm by near-infrared spectroscopy," *Proc. SPIE* Vol. 3194, pp. 133–144 (1998).
56. C. Casavola, L. A. Paunescu, S. Fantini, and E. Gratton, "Blood flow and oxygen consumption with near-infrared spectroscopy and venous occlusion: spatial maps and the effect of time and pressure of inflation," *J. Biomed. Opt.* Vol. 5, pp. 269–276 (2000).
57. S. R. Hintz, D. A. Benaron, J. P. van Houten, J. L. Duckworth, F. W. H. Liu, S. D. Spilman, D. K. Stevenson, and W.-F. Cheong, "Stationary headband for clinical time-of-flight optical imaging at the bedside," *Photochem. Photobiol.* Vol. 68, pp. 361–369 (1998).
58. S. R. Hintz, W.-F. Cheong, J. P. van Houten, D. K. Stevenson, and D. A. Benaron, "Bedside imaging of intracranial hemorrhage in the neonate using light: comparison with ultrasound, computed tomography, and magnetic resonance imaging," *Pediatr. Res.* Vol. 45, pp. 54–59 (1999).
59. B. Beauvoit, T. Kitai, and B. Chance, "Contribution of the mitochondrial compartment to the optical properties of the rat liver: a theoretical and practical approach," *Biophys. J.* Vol. 67, pp. 2501–2510 (1994).
60. M. Kohl, M. Cope, M. Essenpreis, and D. Böcker, "Influence of glucose concentration on light scattering in tissue-simulating phantoms," *Opt. Lett.* Vol. 19, pp. 2170–2172 (1994).
61. J. S. Maier, S. A. Walker, S. Fantini, M. A. Franceschini, and E. Gratton, "Possible correlation between blood glucose concentration and the re-

75. H. Jiang, K. D. Paulsen, U. L. Osterberg, B. W. Pogue, and M. S. Patterson, "Simultaneous reconstruction of optical absorption and scattering maps in turbid media from near-infrared frequency-domain data," *Opt. Lett.* Vol. 20, pp. 2128–2130 (1995).
76. B. W. Pogue, T. O. McBride, J. Prewitt, U. L. Österberg, and K. D. Paulsen, "Spatially variant regularization improves diffuse optical tomography," *Appl. Opt.* Vol. 38, pp. 2950–2961 (1999).
77. D. A. Benaron, D. C. Ho, S. Spilman, J. P. Van Houten, and K. D. Stevenson, "Non-recursive linear algorithms for optical imaging in diffusive media," *Adv. Exp. Med. Biol.* Vol. 361, pp. 215–222 (1994).
78. S. A. Walker, S. Fantini, and E. Gratton, "Image reconstruction using back-projection from frequency-domain optical measurements in highly scattering media," *Appl. Opt.* Vol. 36, pp. 170–179 (1997).
79. M. A. Franceschini, V. Toronov, M. E. Filiaci, E. Gratton, and S. Fantini, "On-line optical imaging of the human brain with 160-ms temporal resolution," *Opt. Express* Vol. 6, pp. 49–57 (2000).
80. S. Fantini, M. A. Franceschini, and E. Gratton, "Effective source term in the diffusion equation for photon transport in turbid media," *Appl. Opt.* Vol. 36, pp. 156–163 (1997).
81. F. F. Jöbsis "Noninvasive, infrared monitoring of cerebral and myocardial oxygen sufficiency and circulatory parameters," *Science* Vol. 198, pp. 1264–1267 (1977).
82. P. W. McCormick, M. Stewart, G. Lewis, M. Dujovny, and J. I. Ausman, "Intracerebral penetration of infrared light. technical note," *J. Neurosurg.* Vol. 76, pp. 315–318 (1992).
83. G. Gratton, J. S. Maier, M. Fabiani, W. W. Mantulin, and E. Gratton, "Feasibility of intracranial near-infrared optical scanning," *Psychophysiology* Vol. 31, pp. 211–215 (1994).
84. S. P. Gopinath, C. S. Robertson, R. G. Grossman, and B. Chance, "Near-infrared spectroscopic localization of intracranial hematomas," *J. Neurosurg.* Vol. 79, pp. 43–47 (1993).
85. S. Fantini, M. A. Franceschini, E. Gratton, D. Hueber, W. Rosenfeld, D. Maulik, P. G. Stubblefield, and M. R. Stankovic, "Non-invasive optical mapping of the piglet brain in real time," *Opt. Express* Vol. 4, pp. 308–314 (1999).
86. C. S. Roy and C. S. Sherrington, "On the regulation of the blood supply of the brain," *J. Physiol.* Vol. 11, pp. 85–108 (1890).
87. A. Villringer and U. Dirnagl, "Coupling of brain activity and cerebral blood flow: basis of functional neuroimaging," *Cerebrovasc. Brain Metab. Rev.* Vol. 7, pp. 240–276 (1995).
88. B. M. Salzberg and A. L. Obaid, "Optical studies of the secretory event at vertebrate nerve terminals," *Exp. Biol.* Vol. 139, pp. 195–231 (1988).
89. R. A. Stepanoski, A. LaPorta, F. Raccuia-Behling, G. E. Blonder, R. E. Slusher, and D. J. Kleinfeld, "Noninvasive detection of changes in membrane

102. A. Villringer and B. Chance, "Non-invasive optical spectroscopy and imaging of human brain function," *Trends Neurosci.* Vol. 20, pp. 435–442 (1997).
103. G. Gratton, M. Fabiani, D. Friedman, M. A. Franceschini, S. Fantini, P. M. Corballis, and E. Gratton, "Rapid changes of optical parameters in the human brain during a tapping task," *J. Cognitive Neuroscience* Vol. 7, pp. 446–456 (1995).
104. K. A. Kang, D. F. Bruley, and B. Chance, "Feasibility study of a single- and multiple-source near-infrared phase-modulation device for characterizing biological systems," *Biomed. Instrum. Technol.* Vol. 31, pp. 373–386 (1997).
105. B. J. Tromberg, O. Coquoz, J. B. Fishkin, T. Pham, E. R. Anderson, J. Butler, M. Cahn, J. D. Gross, V. Venugopalan, and D. Pham, "Non-invasive measurements of breast tissue optical properties using frequency-domain photon migration," *Phil. Trans. R. Soc. Lond. B* Vol. 352, pp. 661–668 (1997).
106. V. Quaresima, S. J. Matcher, and M. Ferrari, "Identification and quantification of intrinsic optical contrast for near-infrared mammography," *Photochem. Photobiol.* Vol. 67, pp. 4–14 (1998).
107. S. Thomsen and D. Tatman, "Physiological and pathological factors of human breast disease that can influence optical diagnosis," *Ann. NY Acad. Sci.* Vol. 838, pp. 171–193 (1998).
108. P. Vaupel, F. Kallinowski, and P. Okunieff, "Blood flow, oxygen and nutrient supply, and metabolic microenvironment of human tumors: a review," *Cancer Res.* Vol. 49, pp. 6449–6465 (1989).
109. V. G. Peters, D. R. Wyman, M. S. Patterson, and G. L. Frank, "Optical properties of normal and diseased human breast tissues in the visible and near-infrared," *Phys. Med. Biol.* Vol. 35, pp. 1317–1334 (1990).
110. T. L. Troy, D. L. Page, and E. Sevic-Muraca, "Optical properties of normal and diseased breast tissues: prognosis for optical mammography," *J. Biomed. Opt.* Vol. 1, pp. 342–355 (1996).
111. S. Fantini, S. A. Walker, M. A. Franceschini, M. Kaschke, P. M. Schlag, and K. T. Moesta, "Assessment of the size, position, and optical properties of breast tumors *in vivo* by non-invasive optical methods," *Appl. Opt.* Vol. 37, pp. 1982–1989 (1998).
112. D. Grosenick, H. Wabnitz, H. H. Rinneberg, K. T. Moesta, and P. M. Schlag, "Development of a time-domain optical mammograph and first *in vivo* applications," *Appl. Opt.* Vol. 38, pp. 2927–2943 (1999).
113. B. J. Tromberg, N. Shah, R. Lanning, A. Cerussi, J. Espinoza, T. Pham, L. Svaasand, and J. Butler, "Non-invasive *in vivo* characterization of breast tumors using photon migration spectroscopy," *Neoplasia* Vol. 2, pp. 26–40 (2000).
114. B. Riefke, K. Licha, and W. Semmler, "Contrast media for optical mammography," *Radiologe* Vol. 37, pp. 749–755 (1997).
115. S. Nioka, S. B. Colak, X. Li, Y. Yang, and B. Chance, "Breast tumor images of hemodynamic information using a contrast agent with back projection and FFT enhancement," *OSA Trends in Optics and Photonics* Vol. 21, *Advances*

130. S. Fantini, E. L. Heffer, M. A. Franceschini, L. Götz, A. Heinig, S. Heywang-Köbrunner, Oliver Schütz, and Horst Siebold, "Optical mammography with intensity-modulated light," Proceedings Volume from In Vivo Optical Imaging Workshop (September 16-17, 1999, National Institutes of Health, Bethesda, MD), A. Gandjbakhche, Ed. (Optical Society of America 2000), *in press*.
131. H. Jess, H. Erdl, K. T. Moesta, S. Fantini, M. A. Franceschini, E. Gratton, and M. Kaschke, "Intensity-modulated breast imaging: technology and clinical pilot study results," *OSA Trends in Optics and Photonics on Advances in Optical Imaging and Photon Migration*, R. R. Alfano and J. G. Fujimoto, Eds., Vol. 2, pp. 126-129, Optical Society of America, Washington, DC (1996).
132. M. Kaschke, H. Jess, G. Gaida, J. M. Kaltenbach, and W. Wrobel, "Transillumination imaging of tissue by phase modulation techniques," in *Advances in Optical Imaging and Photon Migration*, R. R. Alfano (ed.), *Proc. OSA* Vol. 21, pp. 88-92 (1994).
133. S. Fantini, M. A. Franceschini, S. A. Walker, J. S. Maier, and E. Gratton, "Photon path distributions in turbid media: applications for imaging," *Proc. SPIE* Vol. 2389, pp. 340-349 (1995).



DEPARTMENT OF THE ARMY  
US ARMY MEDICAL RESEARCH AND MATERIEL COMMAND  
504 SCOTT STREET  
FORT DETRICK, MD 21702-5012

REPLY TO  
ATTENTION OF

MCMR-RMI-S (70-1y)

1 July 03

MEMORANDUM FOR Administrator, Defense Technical Information  
Center (DTIC-OCA), 8725 John J. Kingman Road, Fort Belvoir,  
VA 22060-6218

SUBJECT: Request Change in Distribution Statement

1. The U.S. Army Medical Research and Materiel Command has reexamined the need for the limitation assigned to technical reports written for this Command. Request the limited distribution statement for the enclosed accession numbers be changed to "Approved for public release; distribution unlimited." These reports should be released to the National Technical Information Service.

2. Point of contact for this request is Ms. Kristin Morrow at DSN 343-7327 or by e-mail at Kristin.Morrow@det.amedd.army.mil.

FOR THE COMMANDER:

Encl

PHYLLIS M. RINEHART  
Deputy Chief of Staff for  
Information Management



ADB274518  
ADB287328  
ADB277943  
ADB288221  
ADB248332  
ADB265760  
ADB287619  
ADB281577  
ADB287600  
ADB288422  
ADB288375  
ADB268297